Fall 1-31-2003

Numerical and experimental investigation of dry particle coating

Ajit Mujumdar
New Jersey Institute of Technology

ABSTRACT

NUMERICAL AND EXPERIMENTAL INVESTIGATION OF DRY PARTICLE COATING

by

Ajit Laxmikant Mujumdar

Dry particle coating is an emerging field in the industries that deal with particulate products and powder processing. Compared to the widely reported experimental studies of the dry particle coating, the theoretical modeling of such processes is found to be less comprehensive. The work presented in this thesis is an attempt to fill this gap.

The first part of the dissertation aims at the numerical investigation of the hybridization system (Nara Machinery, Tokyo, Japan). The flow behavior of different materials processed in this device is analyzed using three-dimensional Discrete Element Method (DEM) as well as the computational fluid dynamics (CFD) models. The particulate motion is directly simulated using the DEM code, which incorporates the effect of the fluid drag force, computed through the CFD models. The diagnostic investigation includes various aspects pertinent to the effectiveness of the hybridizer system in the coating process. Inter-particle collisions and particle-wall collisions as well as the normal and tangential forces between the particles are estimated which play an important role in the surface modification process of a powder. Experimentally measured velocities in the mixing chamber are in good agreement with the computed velocities. CFD results show that the flow field is not significantly affected as the volume fraction of particles is varied from 3 to 10 percent. Overall, it is found that the combined DEM-CFD model appears to be an adequate approximation of the behavior of the fluid-particle system in the hybridizer.

The experimental part of this dissertation presents an investigation of different powder processing devices such as the Hybridizer, Mechanofusion and Magnetically Assisted Impaction Coating (MAIC) devices for a specific application of improving the humidity resistance of the ground magnesium powder through the dry particle coating technique. It is shown that coating by wax (1 percent by weight) is sufficient to increase the humidity resistance of ground magnesium to a level almost as good as the atomized magnesium powder.

The last part of the dissertation deals with a related, yet different type of numerical study, carried out using the DEM approach, of the granular flows and mixing behavior in the oscillating sectorial containers. Mixing patterns are observed for a wide range of frequencies of oscillation as well as different operating conditions such as the powder loading, the coefficient of friction, and the coefficient of restitution. It is observed that the flow patterns follow a particular trend and there exists a critical frequency at which the mixing rate is very small.

NUMERICAL AND EXPERIMENTAL INVESTIGATION OF DRY PARTICLE COATING

by
Ajit Mujumdar

A Dissertation
Submitted to the Faculty of
New Jersey Institute of Technology
In Partial Fulfillment of the Requirements for the Degree of
Doctor of Philosophy in Mechanical Engineering

Department of Mechanical Engineering

January 2003

APPROVAL PAGE

NUMERICAL AND EXPERIMENTAL INVESTIGATION OF DRY PARTICLE COATING

Ajit Laxmikant Mujumdar

Dr. Rajesh N. Dave, Dissertation Advisor — Date
Professor of Mechanical Engineering, NJIT

Dr. Ian S. Fischer, Committee Member — Date
Professor of Mechanical Engineering, NJIT

Dr. I. Jŏga Rao, Committee Member — Date
Assistant Professor of Mechanical Engineering, NJIT

Dr. Chao Zhu, Committee Member — Date
Assistant Professor of Mechanical Engineering, NJIT

Dr. Robert Pfeffer, Committee Member — Date
Distinguished Professor of Chemical Engineering, NJIT

BIOGRAPHICAL SKETCH

Author: Ajit Laxmikant Mujumdar

Degree: Doctor of Philosophy

Date: January 2003

Undergraduate and Graduate Education:

- Doctor of Philosophy in Mechanical Engineering,
  New Jersey Institute of Technology, Newark, NJ, 2003
- Master of Technology in Instrument Technology,
  Indian Institute of Technology, New Delhi, India, 1997
- Bachelors of Science in Mechanical Engineering
  Nagpur University, Nagpur, India, 1994

Major: Mechanical Engineering

Presentations and Publications:

Ajit Mujumdar, Dongguang Wei, Rajesh Davé, Robert Pfeffer
"Improvement of Humidity Resistance of Magnesium powder by Dry Particle Coating" Submitted Powder Technology, August 2002.

Moinuddin Malik, Ajit Mujumdar, Rajesh Davé,
"Numerically-simulated Characteristics of Oscillating Sectorial Containers" Submitted Powder Technology, November 2002.

Rajesh Davé, Wenliang Chen, Ajit Mujumdar, Wenqiang Wang, Robert Pfeffer
"DEM for Dry Particle Coating", World Congress on Particle Technology, Sydney, Australia, July 2002.

Ajit Mujumdar, Moinuddin Malik, Robert Pfeffer, Rajesh Davé,
"Numerically-simulated Characteristics of Oscillating and Rotating, Sectorial and Cylindrical Containers" Proceedings at Annual meeting AIChE conference, Los Angeles, CA Nov-12-Nov17, 2000.

Ajit Mujumdar, Wenliang Chen, Moinuddin Malik, Robert Pfeffer, Rajesh Davé, "Diagnostic Analysis of Hybridization system by Numerical Simulation" Proceedings at Annual meeting AIChE conference, Los Angeles, CA Nov- 12-Nov17, 2000.

T. P. Ravchandran, A. Mujumdar, Gregory James, R. N. Davé, C. Y. Wu, S. Wantano, "Study of Powder Discharge from a Vibrated Hopper", Mini-symposium on Particle Technology, Particle Processing Research Center, New Jersey Institute of Technology, March 25-26, 1999.

Ravichandran, T. P., A. Mujumdar, C-Y. Wu, S. Watano and R. N. Davé, "Study of Powder Segregation During Discharge from a Vibrated Hopper," Advanced Technologies for Particle Processing: 1998 AIChE Conference, Vol. I, pp. 519-525, November 1998.

To my father (baba), mother (aai), brothers Amol and Amit
for their love, support and encouragement

ACKNOWLEDGMENT

I wish to express my sincere appreciation to my advisor Dr. Rajesh Dave for his guidance, supervision and support throughout this research. Without his innovative ideas and constant encouragement, it would have been impossible to finish this dissertation. Special thanks are due to Dr. Robert Pfeffer, Dr. I. Joga Rao, and Dr. Ian Fischer, Dr. Chao Zhu for their active participation in my dissertation committee. I am also thankful to Dr. Moinuddin Malik for his valuable suggestions in this study.

I am grateful to the supports from Graduate Office, National Science Foundation, New Jersey Commission on Science and Technology, and US Army (Picatinny Arsenal) for the funding of this research work. Technical assistance from Tsingua University, Nara machineries and Dr. Otis Walton for providing the numerical code is also greatly acknowledged.

I would like to thank Dr. Bodhisattwa Chaudhuri, Dr. Wenliang Chen, Dr. Dongguang Wei, Mr. Amit Banerjee, and Mr. Yueyang Shen for their valuable help during research.

In the end, I would like to express my endless gratitude to my parents, Mr. Laxmikant Mujumdar and Dr. Shyamala Mujumdar, who have always supported my academic pursuit and encouraged me in every possible ways. Also, I want to thank my wife, Renuka and son, Ameya for their love and support throughout these years.

TABLE OF CONTENTS

TABLE OF CONTENTS
(Continued)

Chapter **Page**

TABLE OF CONTENTS
(Continued)

TABLE OF CONTENTS
(Continued)

Chapter **Page**

LIST OF TABLES

LIST OF FIGURES

LIST OF FIGURES
(Continued)

LIST OF FIGURES
(Continued)

Figure **Page**

LIST OF FIGURES
(Continued)

Figure **Page**

LIST OF FIGURES
(Continued)

Figure **Page**

LIST OF FIGURES
(Continued)

CHAPTER 1

INTRODUCTION

1.1 Dry Particle Coating

Dry particle coating is an emerging technology in the field of chemical and powder processing industries. Traditionally, powder processing and coating is done by wet coating methods such as fluidized beds, pan coaters etc, or by wet chemistry based techniques such as coacervation, interfacial polymerization etc. These techniques have certain drawbacks, in particular from the environmental point of view, as these methods tend to produce waste products, which may be hazardous. Hence, over the last decade, researchers in the field of powder technology (Yokoyama *et al.*, 1987; Tanno 1990; Naito *et al.*, 1993) have diverted their attention to find an alternative or other suitable means of coating of powders. Dry particle coating technique has drawn tremendous attention of many researchers as these methods do not produce any hazardous waste products and do not require any binder or solvent for coating.

Dry particle coating processes were developed in Japan about fifteen years ago, and are still in the stages of optimization. Typically, in dry particle coating, smaller particles (guests) are mixed with the bigger particles (host), and by means of mechanical processes such as high shear, high impaction etc, the particles are forced to collide with each other as well as with the boundaries of the system. This results in the mechanical fixing of smaller particles onto the surface of the host particles. The strength of this force by which the guest particles are attached onto the surface of the host particles depends upon number of factors, such as size and density of particles, the type of processing

device, the operating conditions of the processing device etc. Depending upon all these factors, the coating may be categorized into partial coating, continuous coating, film coating, deep embedding, encapsulation etc. Due to the lack of a general rule governing the coating process, the studies have to be carried out mostly by trial and error method. As the characterization of these powders often takes a long time, trial and error is not an ideal way to decide the parameters for coating, which necessitates the development of some kind of a guideline, which would help determining the type of dry particle coating device and also the close prediction of the operating conditions.

Much emphasis has been given to the experimental studies in the recent years. Compared to the widely reported experimental studies, less attention has been paid to theoretical modeling of the dry particle coating devices. Since the different coating devices use different mechanisms of coating, the modeling of these processes is not straightforward. The performance of the commercially available devices used for dry particle coating is under investigation by researchers in this field and this lack of information makes the study of these dry coating devices from numerical modeling point of view extremely important, and that is the major focus of this dissertation.

1.2 Objectives

This research is dedicated to several aspects of dry particle coating. The study is divided into two broad areas. The first area is the numerical investigation of one of the dry particle coating devices, called as Hybridization system, which is a commercial coating device developed by Nara Machinery, Japan. The numerical investigation also includes a preliminary study of granular flows in oscillating containers. The second area of research

is the experimental study of an application of dry particle coating process to improve the humidity resistance of ground magnesium powder.

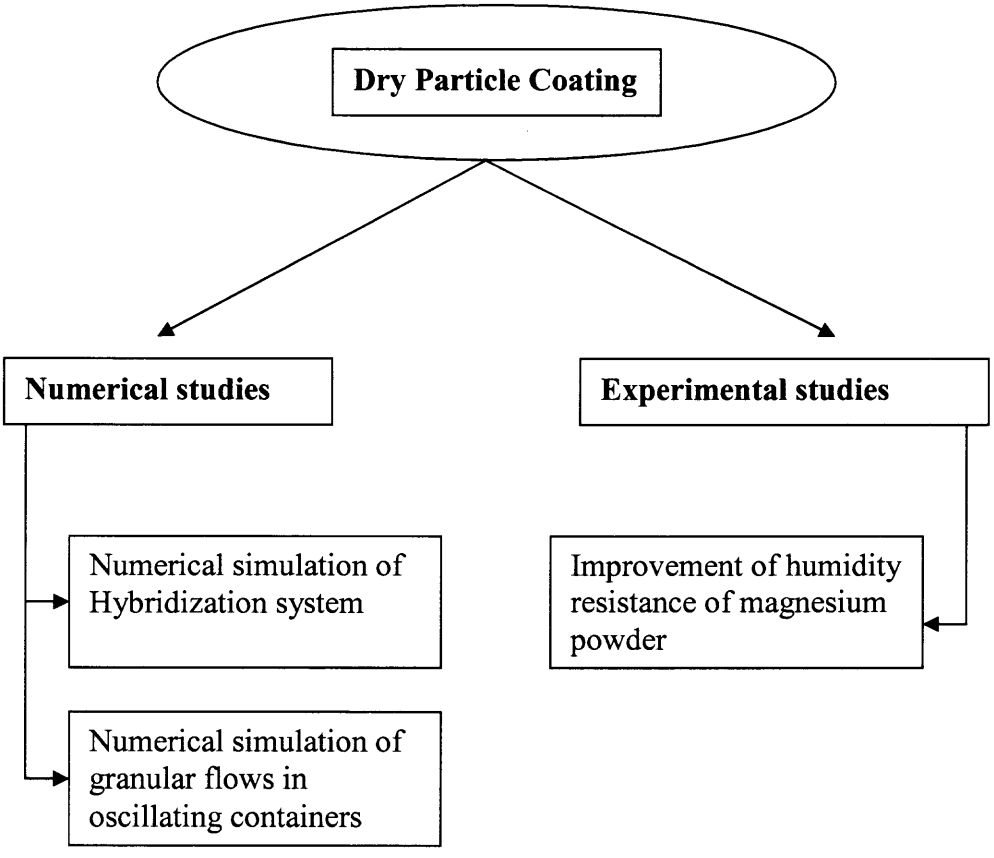

Figure 1.1 Objectives of the dry particle coating studies.

The general outline of the research work carried out and presented in this dissertation is shown in Figure 1.1.

For the numerical simulation of hybridization system, a numerical model is developed based on the Discrete Element Method (DEM) to analyze the diagnostic properties of the mixing chamber of the hybridization system. The diagnostic properties such as the rotational kinetic energy, pressure distribution inside the system are

evaluated. The inter-particle collisions as well as the collisions of the particles with the walls of the container are calculated. The effect of different operating conditions on the performance of the hybridization system is computed. The inter-particle forces are also calculated which show the possible impaction strength of the particles.

Induced airflow due to the high-speed rotation of the blades inside the mixing chamber of the hybridization system is also analyzed using computational flow dynamics techniques. Velocity and pressure contours for different rotational speeds of the hybridization system are studied and their importance from the simulation point of view is outlined. Numerically simulated and experimentally measured values of the velocities in the system are compared. Coupling of particles and fluid velocities is done in the DEM studies. The effect of the airflow field on the particles is studied. A multi-phase model is also developed to compute the velocity contours. Different operating parameters such as rotational speeds, and volume fraction are studied through this multi-phase model.

The second part of the numerical studies is devoted to the investigation of the flow characteristics of the granular flows in an oscillating sectorial container. The numerical simulation of the particles behavior inside the sectorial container is carried out for the set of unary and binary system of particles. The idea is emerged from the fact that the hybridization system, which typically has six blades rotating inside a circular chamber, forms a sectorial portion between the regions formed by two blades. Hence, in order to study the DEM modeling from the mixing and segregation point of view, these simulations are performed. Degree of mixing of the binary system of particles is studied and the mixing rate constants are calculated. The effect of different range of frequencies

on the performance of oscillating sector is outlined. Critical frequency when the particulate bed becomes stationary is computed for the unary and binary system of particles, for different loading conditions.

The last part of the dissertation deals with the experimental investigation of an application of dry particle coating technique to improve the humidity resistance of ground magnesium powder. Dry particle coating devices such as Magnetically Assisted Impaction Coating (MAIC), Hybridization system, and Mechanofusion are used to coat ground magnesium particles using carnuba wax, which is hydrophobic in nature. The coated products are treated and characterized in the humidity chamber, XRD, SEM etc. The performance of the coated product is compared with atomized magnesium particles, which absorb a little amount of water. A potentially cost-effective method for the improvement of humidity resistance of the ground magnesium powder using dry particle coating is suggested.

The above outlined studies are presented in subsequent chapters with an idea that not only will they provide valuable information and understanding of the dry particle coating process/devices, but will also lead to other extensive and exciting applications of dry particle coating. In general, the numerical and experimental studies carried out in this dissertation are aimed to have a better understanding of the operation of these dry particle-coating devices.

CHAPTER 2

BACKGROUND

2.1 Introduction

As outlined in the previous chapter, dry particle coating is a process where guest particles are embedded onto the surface of host particles by means of mechanical forces. These new coated products have value-addition. Due to the small size of guest particles, the van der Waal's forces are sufficient to hold the guest particles onto the surface of the host particles. The simple schematic illustrating the process of dry particle coating is shown in Figure 2.1 below.

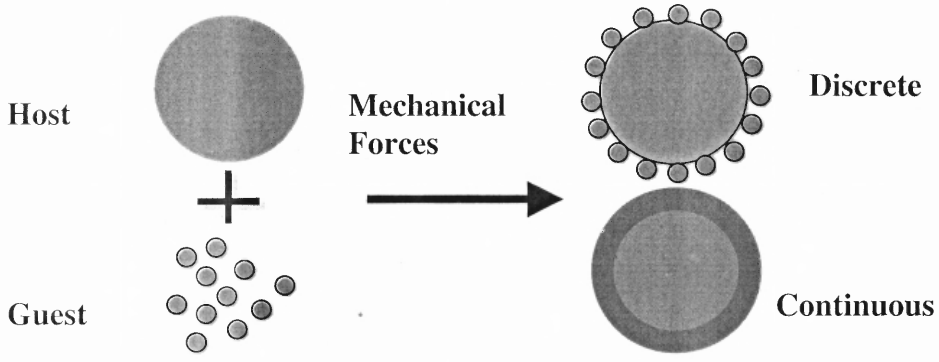

Figure 2.1 Dry particle coating.

Dry particle coating can be used for altering the properties of the materials, which are also called as 'engineered materials'. Typical applications include but are not limited to flowability, solubility, dispersibility, wettability (hydrophobic/hydrophilic properties), electric, electrostatic, magnetic, optical, color, flavor, taste, shape, sphericity, solid phase

reactivity. These are whole new areas of research where dry particle coating finds its applications.

Another advantage of dry particle coating is that these processes are environmentally benign. As the catalyst or binder/solvent is not required, the processes are environmentally safe. Moreover, the use of dry particle coating can be used as a cost saving approach, as the cheaper material, produced by altering the properties to the desired level, can replace highly expensive material.

Dry particle coating methods find applications in various industries such as food, pharmaceutical, herbal/cosmetic, agricultural, chemical, powder processing industries etc. There are many interesting applications of dry particle coating (Alonso et al., 1989a and 1989b; Chaudhuri et al.., 1998; Watano et al.., 1998; Ramlkhan et al.., 2000).

2.2 Origins of Dry Particle Coating

The subject of dry particle coating is very closely related to the subject of dry mixing of powders. Ideally, a binary mixing process should intimately mix the two species so that any small sample taken from the mixture would contain the same proportion of the two constituents. This is hard to achieve, particularly when the powders are either cohesive, or the two species to be mixed are quite different in size. When the powders are cohesive, they naturally form agglomerates and mixing two constituents requires breaking up the agglomerates. When the constituents differ in size, there is an increased tendency for segregation, as the size difference becomes larger. However, when the two components to be mixed are very different in size (one or two orders of magnitude), then segregation may no longer be a problem. In such cases, the smaller particles tend to

adhere onto the larger particles. The adhesion force between the smaller particle and the larger particle is greater than the weight of the smaller particle, and hence it is not easily removed from the host. This phenomenon is usually referred to as "ordered mixing" or "structured mixing".

The advantage of ordered mixing is that it provides a much better degree of homogeneity as long as the particle size distribution of the larger size species is not too wide (Hersey, 1975; Bannister *et al..,* 1983; Enstad, 1981). Hence in terms of subsequent segregation, ordered mixtures are more stable than ordinary mixtures (Hersey, 1975; Yip and Hersey, 1977; Staniforth, 1985; Bannister *et al..,* 1983; Bryan *et al..,* 1979; Lai and Hersey, 1981; Thiel *et al..,* 1982). It was also discussed in this literature that having a very wide size distribution of the large size species may lead to "ordered unit segregation" (Hersey and Thiel, 1979; Lai and Staniforth, 1981; Thiel *et al..,* 1982; Yip and Hersey, 1977), which should be avoided.

While there is little available in terms of quantitative modeling of the ordered mixing process (except work by Alonso *et al..,* 1989a, 1989b, 1990, and 1991), a qualitative explanation is given in Bannister and Harnby, (1983). Three stages are identified: (1) separation of the agglomerates of the fine constituent into their primary particles, (2) bonding of these fines to the carrier particles, and (3) redistribution and exchange of fines among the carrier particles until a random distribution is achieved. While the real process may not take place exactly in that order, it is clear that the de-agglomeration of fines must occur in order to create such a mixture. Therefore, any mixing device, in order to achieve ordered mixing, must provide sufficient mechanical or other means of agitation to promote de-agglomeration of fines, i.e., provide a large

number of particle collisions involving high normal and shear impact forces. Machines that can be used for this purpose are high intensity mixers and grinding machines such as ball and media mills.

There is another reason why ordered mixing and/or dry coating work well when using grinding type machines. It is easier to break up agglomerates into primary size particles in the presence of coarser particles in the mix when processed in a milling machine, than having fine particle agglomerates alone. While this behavior was only speculated by Yeung and Hersey, in 1977, later in 1991, Alonso showed this through statistical computer simulations. This phenomenon works to the advantage of dry particle coating when performed in a milling type machine because the host particles act as the media and help in de-agglomerating the fines.

The concept of ordered mixing was also taken one step further (to dry coating) by using dry impact blending, as described in a series of papers by another Japanese group (Honda *et al..,* 1987, 1988, 1989, and 1991). They argued that an ordinary dry blending process would result in an ordered mixture, as the fine particles attach to the larger host particles through electrostatic forces (Honda *et al..,* 1991). However upon processing in an impact-blending device, the large impulsive forces cause the fine particles to become firmly attached to the core particle and a coated composite particle is obtained. This device, called the Hybridizer, is manufactured by Nara Machinery of Japan. The hybridizer has proven very useful for pharmaceutical applications; for example, it accelerated aspirin dissolution when coated onto an excipient such as potato starch (Iskizata *et al..,* 1988).

The mechanofusion and hybridizer machines referred to above can produce chemical as well as physical surface interactions between the host and guest particles.

While most of the literature in dry coating comes from Japan, during the last few years, several concentrated activities in this area (some proprietary, and not yet described in the literature) have been initiated in the US. At the New Jersey Institute of Technology (NJIT), a new device was invented based on the principle of centrifugal fluidization. This device called the Rotating Fluidized Bed Coater (RFBC) (Watano *et al..,* 1998) can also produce soft coatings. Most recently, a novel class of coating technique has been proposed based on the concept of direct fine particle generation and subsequent coating onto host particles. In one such process, nano-sized guest particles are generated by laser ablation of a target (e.g., Ag, Y_2O_3:Eu^{+3}, and $TaSi_2$), and the particle flux in a plasma is directed towards a small fluidized (caused by vibration) bed of micron sized host particles (Fitz-Gerald *et al..*, 1998, 1999a and 1999b). While difficult to scale-up, this laser ablation technique can coat very fine (less than 5 μm) host particles by ultrafine guest particles, an important consideration for the pharmaceutical industry. Similar processes based on sputtering and other techniques that allow for producing a flux of nano-particles, have also been proposed.

2.3 Dry Particle Coating Devices

As already discussed in the previous section, there are numerous devices available for dry particle coating. These devices, although different in their manner of supplying the necessary mechanical forces, all strive to efficiently promote the de-agglomeration of the guest particles and their adhesion onto the surface of the host particles. In the hybridizer,

the ultra high rotational speed of the blades and recirculation of the powder allows the host and guest particles to violently collide with each other. In mechanofusion, the particles are also subjected to severe shear and compressive stresses as they travel between the clearance of a rotating drum and inner piece. In MAIC, the magnetic particles spin furiously due to an oscillating electromagnetic field causing collisions between the host and guest particles, and the walls of the device. In the theta composer, the guest particles are impacted onto the host particles by the high-speed motion of an elliptical rotor in an elliptical mixer. In RFBC, de-agglomeration and impaction of the guest particles onto the hosts occur because the bed is fluidized at very high gas velocities resulting in very good mixing and high shearing stresses. All of these devices have been used successfully by many investigators to produce composite particles with unique and improved functionality. With the exception of the theta composer, all the other devices are available at NJIT. In the next section, these dry coating devices will be described in more detail.

2.3.1 Mechanofusion

A schematic of the mechanofusion machine is shown in Figure 2.2. The device consists mainly of a rotating outer vessel, a stationary inner piece and a stationary scraper (the scraper and inner piece can be either ceramic or stainless steel). A measured amount of host and guest particles is placed into the rotating vessel. As the vessel rotates at speeds between 200 to 1600 rpm, the powder is forced outward towards the walls of the vessel. The gap between the inner piece and the rotating drum is controlled, and as a result, the particles passing through the gap are subjected to intense shearing and compressive forces. These forces generate sufficient heat energy to "fuse" the guest particles onto the

surface of the host particles. The gap size between the inner piece and the walls of the vessel is very important in controlling the thickness of the desired coating. The gap between the scraper and the wall of the vessel is also controlled. The scraper breaks-up and disrupts any build-up or caking of the particles on the walls of the vessel. This is a batch-operated device.

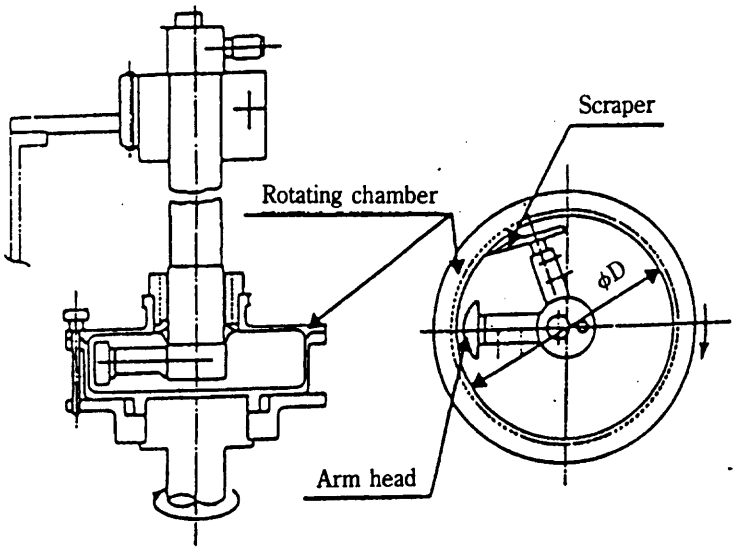

Figure 2.2 Schematic of Mechanofusion system.

There are several advantages in using the mechanofusion system. First, the shape of the inner piece, the small gap, and the high rotation speed of the drum allow the particles to be subjected to very high shear and compressive forces. Second, there is a local temperature build-up due to these strong forces acting on the particles, which can result in the fusion of the surface of the host and guest particles. This produces very strong physical and/or chemical bonds, which enhance the coating process.

2.3.2 Hybridizer

The hybridizer, shown schematically in Figure 2.3, consists of a high-speed rotor with six blades, a stator and a powder re-circulation circuit. Similar to the mechanofusion system,

the rotor with six blades and the powder re-circulation circuit (the inner lining) can be made with ceramic or stainless steel.

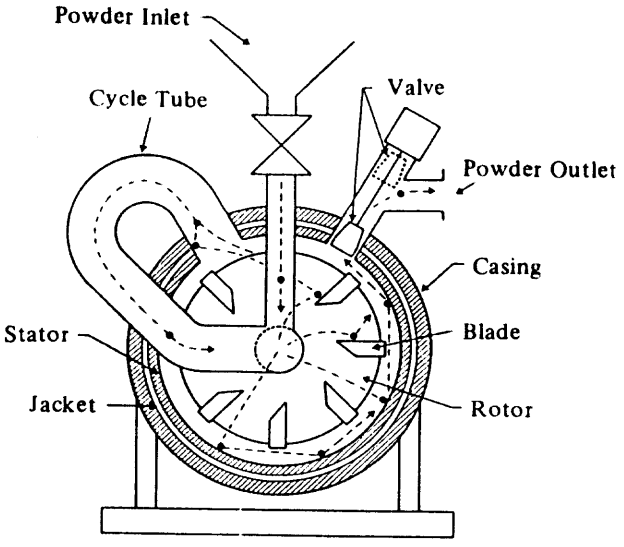

Figure 2.3 Schematic of Hybridizer.

The powder (host and guest particles) placed in the processing part of the vessel is subjected to high impaction and dispersion due to the high rotating speed of the rotor. The particles undergo many collisions, and this allows for break-up of fine agglomerates and powder coating due to the embedding or filming of the guest particles onto the surface of the host particles. Currently, this is a batch-operated device.

The hybridizer has several advantages that make it a powerful dry coating device. First, the rotor of the hybridizer can rotate anywhere from 5000 rpm to 16000 rpm. Due to the strong forces applied to the materials at these high rpm, very short processing times are required to achieve coating. Second, the device consists of a re-circulating unit that continuously moves the particles in and out of the processing vessel and against the blades of the rotor. Lastly, similar to mechanofusion, there is a temperature build-up due

to the high impaction forces caused by the high rotation speeds, which aids in coating the guest particles onto the surface of the host particles.

2.3.3 Magnetically Assisted Impaction Coater (MAIC)

A schematic of the magnetically assisted impaction coating device is shown in Figure 2.4. Although MAIC can be used in a continuous mode (Hendrickson and Abbott, 1997), the small bench-scale device used at NJIT operates in a batch mode. A measured mass of both host and guest particles is placed into a processing vessel (125 ml glass bottle). A measured amount of magnetic particles is also placed in the processing vessel. The magnetic particles are made of barium ferrite and coated with polyurethane to help

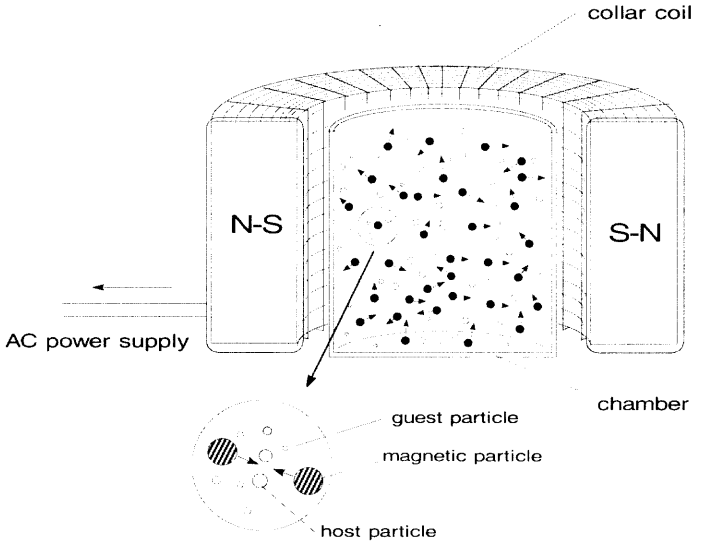

Figure 2.4 Schematic of MAIC.

prevent contamination of the coated particles. An external oscillating magnetic field is created using a series of electromagnets surrounding the processing vessel. When a magnetic field is created, the magnetic particles are excited and move furiously inside the vessel resembling a gas-fluidized bed system, but without the flowing gas. These agitated magnetic particles then impart energy to the host and guest particles, causing collisions

and allowing coating to be achieved by means of impaction or peening of the guest particles onto the host particles.

There are several unique features of MAIC that make it advantageous as a dry particle coating device. Firstly, the MAIC can coat soft organic host and guest particles without causing major changes in the material shape and size. Secondly, although there is some heat generated on a microscopic level due to the collisions of particles, there is negligible heat generation on a macroscopic level and hence no increase in temperature of the material during processing by MAIC. This is desirable when processing temperature sensitive powders such as pharmaceuticals. Lastly, the device can be operated both as a batch and continuous system making it versatile in the amount of material it can process.

2.4 Magnesium Powder Coating

As an application of dry particle coating technique, magnesium powder in the ground and atomized form was studied. As will be explained later in detail about this coating in chapter 7, coating carnuba wax on the surface of the magnesium powder increased the humidity resistance of ground magnesium powder.

Magnesium is the eighth most abundant element in the earth's crust although not found in it is elemental form. It is a Group II element called alkaline earth metals. Magnesium is a light, silvery-white, and fairly tough metal. It tarnishes slightly in air, and finely divided Mg readily ignites upon heating in air and burns with a dazzling white flame. Normally Mg is coated with a layer of Mg oxide - MgO, which protects Mg from air and water.

The uses of Mg largely center on 3 properties of the metal:

- ❖ Its ability to form intermetallic compounds with other metals
- ❖ Its high chemical reactivity
- ❖ Its low density

Uses of Magnesium

- It is one third lighter than aluminum, and in alloys is essential for airplane and missile construction, racing bikes and other things that need light metals.
- The metal improves the mechanical, fabrication, and welding characteristics of aluminum when used as an alloying agent. Also used in fireplace bricks, flashbulbs, pigments and filters
- Magnesium is used in producing nodular graphite in cast iron, and is used as an additive to conventional propellants.
- For cast metal components from either sand or die-casting. This is the area of strongest demand growth for Mg; particularly in the US automotive market as US car producers attempt to meet current and future fuel economy standards.
- It is also used as a reducing agent in the production of pure uranium and other metals from their salts.
- The hydroxide (milk of magnesia), chloride, sulfate (Epsom salts), and citrate are used in medicine: Chemical reagents.
- Dead-burned magnesite is employed for refractory purposes such as brick and liners in furnaces and converters.
- Flashlight photography, flares, and pyrotechnics, including incendiary bombs.

There are 2 detrimental mechanisms that undermine the ground Mg powder, these are:

1. Presence of a larger surface area to the volume ratio, due to fragmentation during grinding in the ground Mg powder, which provides more surface for Mg $(OH)_2$ formation than the atomized Mg powder.

2. Non-coherent nature of the Mg $(OH)_2$ layers that form on the ground Mg powder particles with no limitation due to lack of protective layer formation.

The result of powder coating suggest that ordered mixing proceeds essentially as a chemical reaction, i.e. through collisions between the "reacting" components. As a result of collisions, the exchange of fine particles between large particles (carriers) occurs simultaneously with the gradual de-agglomeration (homogeneity) of the fine component over the surface of carriers. Three different types of devices are used to coat Mg powder with carnauba wax. All these devices are based on the principle of high shear stress and impaction force causing the guest particles to get embedded onto the surface of the host particles. These devices were:

- Mechanofusion (a high shear mill)
- Hybridizer
- Magnetically Assisted Impaction Coating (MAIC)

The Hybridizer and Mechanofusion systems generate high temperatures as compared to other methods, due to high speed rotating blades.

2.5 Numerical Simulations

2.5.1 Dynamic Simulation Method Review

Particle simulation provides a direct route from the microscopic details of a system (molecular geometry, the interactions between them, etc.) to macroscopic properties of

experimental interests (the equation of state, transport coefficients, structural order parameters, and so on). As well as being of academic interest, this type of information is technologically useful. It may be difficult or impossible to carry out experiment under extreme condition or special requirement, but can be conducted easily from computer simulation. Particle simulation technology started in the early 1970s'. Basically, there are two mechanisms dealing with particle simulation: kinematics method and dynamic method. The theory of kinematics method is based on the fluid dynamics. It is mostly used to simulate the dynamics system including particle flow. Here the constitutive equations are analyzed for the particle assembly. This type of continuum approach is capable of providing some useful information on macroscopic behaviors of powder assembly during process. However, it is impossible to elucidate the effects of particle geometrical factor like size and distribution, surface factors like friction and cohesion as well as physical factor like interaction forces between particles to the system, because the developed constitutive equations are not related to them. Particle dynamic simulation investigates the behavior of particles in this respect. It treats the particle as an assembly of particles instead of a continuum. The behavior of each particle is described to relate to the macroscopic behavior of the assembly.

Most particle dynamic simulations use the discrete element (DE) method. The term "discrete element" refers to the fact that the simulation models the particles as a system of individual particles. Examples of DE model include Molecular Dynamics (MD) method, Monte Carlo (MC) techniques, etc. Molecular dynamics is the term used to describe the solution of the classical equations of motion (Newton's equations) for a set of molecules. Monte Carlo simulation is so called because of the rule that random

numbers play in the method. By MD simulation, it is possible to solve the dynamic problem without making any approximations within the limits imposed by machine accuracy. MD simulation has been applied widely to the study of the structure and dynamics of molecular liquids and solids. It is well used in the granular flow simulation including studies of size segregation due to shaking.

Computer simulation of dense-phase discrete particle systems was first reported by Cundall and Strack (1979). The scheme developed was termed the "distinct element method (DEM)". The method is analogous to molecular dynamics simulation. However, the discrete element simulation of particles is more complicated because of the non-linear and non-central inter-particle interactions arising from auto adhesion, friction and presence of a viscous fluid. Because of the different treatment of particle interaction in DEM simulation, soft spheres and hard spheres models are available. The hard spheres approach assumes that the particles interact by instantaneous collisions such that linear and angular momentum is balanced using collision operators to dissipate energy. Such a simulation uses a kinematics approach that describes the individual particles by their instantaneous positions and velocities. Hard spheres simulations are mainly concerned with rapid granular flows (Campbell and Brennen, 1985). In contrast to hard spheres where the collisions are instantaneous, the soft spheres go through certain deformations during collisions and have a finite contact time. This is a generally a better representation of what actually happens during impact. So the soft spheres method is one of the more common discrete element simulation techniques since it can handle a variety of inter-particle forces. In soft spheres simulation, the interactive forces exerted on each particle are computed as continuous functions of the distance between contiguous particles and

are based on physically realistic interaction laws. This approach is more computationally intensive, but provides information on the structure and dynamics of system including details of position, velocities, forces and energy partitions. During the simulation, the forces (body and surface forces) acting on each particle in the system are calculated. Newton's second law is then used to determine the resulting accelerations for each particle, which are then integrated in time to find the particle's new state. This process is repeated until the simulation ends.

2.5.2 Recent Work on DEM Model

- Walton et al. (1988), Walton (1993) used three-dimensional discrete particle models to calculate inelastic, frictional granular flows. Good quantitative agreements have been achieved with experiment measurements and with theories when the same assumptions are made in the models and the theories.
- Walton (1992) reviewed numerical simulation of inelastic, frictional particle-particle interaction by discrete particle simulations.
- Kafui and Thornton (1993), Thornton (1996) and Ning et al. (1997) used DEM to simulate agglomerates impacting a wall.
- Muguruma et al. at (1997) applied DEM to simulate the three-dimensional motion of all individual particles in a rotating mixer with two baffles. The effect of the baffles on the particle mixing and on the motion of particles is studied.
- Lian et al. (1997, 1998) described computer simulation of pendular state wet agglomerates undergoing pair-wise collisions based upon soft spheres formulation.
- McCarthy (1998) proposed a hybrid technique based on soft spheres model for granular mixing. By focusing the particle dynamics simulation only where it is

needed, the new technique can yield more than an order of magnitude increase in computational speed and number of particles system can deal with.

- Matchett, et al. (2000) compared the experimental data from a vibrating bed of particles with that from 2D DEM simulation on the basis of energy dissipation. It shows that DEM simulation is able to qualitatively reproduce features found in the experimental data. However, the DEM simulation did not perform well at low accelerations and the calculation of applied force based on work done was not successful.

As will be explained later, the importance of air draft through the re-circulation tube, essential for the coating and effective use of hybridization system, it becomes important to investigate the literature available in this area where the researchers in the past have employed DEM technique together with the effect of fluid in the system.

As seen from the literature, many research scientists from Japan have been actively working in this field. Pioneers in the multi-phase flow analysis are Anderson and Jackson (1961) who developed the "Two-fluid models". Discrete element models and two-fluid models have been the major two approaches in the direct numerical simulation of powders applied to the fluidized beds, where the particle phase is treated like a continuum. It was first solved numerically by Pritchett (1978). For the constitutive equation, i.e. the stress term of the dispersed solid phase, Pritchett (1978) used the elastic modulus of emulsion phase determined experimentally by Rietema (1973). To treat the constitutive equation more rigorously, the kinetic theory was extended to the fluidized solids, e.g. Ding and Gidaspow (1990), Blazer and Sinomin (1996) and Syamlal (1993). However, the constitutive equations for the solid phase, which the two fluid models have

adopted, seem still not sufficiently validated as indicated by Boemer et al. (1995). Furthermore, the particle pressure predicted by the kinetic theory faces a problem when the particles are not completely fluidized.

2.6 Summary

By taking a look at the literature, it is quite clear that many efforts have been made in the development of dry particle coating technique to enhance the surface modification of powders. Much emphasis has been given to the experimental side of this research field but strong numerical work, which links these two, is somewhat missing. Experimental validation of the numerical results is not much, which becomes the motivation and the objective of the research work proposed.

CHAPTER 3

NUMERICAL SIMULATION OF HYBRIDIZATION SYSTEM

3.1 Introduction

The first part of this dissertation deals with the numerical studies of dry particle coating process focusing the hybridization system. This work presents the investigation of numerical modeling of a commercial powder surface modification system, called as hybridizer (Nara Machinery Co. Ltd., Tokyo, Japan). The work presented in this chapter is the first attempt on numerical simulation of the hybridization system based on the DEM technique. The numerical study performed is on the mono-dispersed system based on a three-dimensional simulation. The results of the diagnostic analysis of the hybridizer system, based on numerical simulation, are presented. The diagnostic studies include various aspects pertinent to the effectiveness of the hybridizer system in coating process. The effect of various parameters on the flow characteristics of particles is analyzed. Inter-particle collisions and particle-wall collisions as well as the normal and tangential forces between the particles are estimated which play an important role in the surface modification process of a powder. Also, the pressure distribution across the different zones inside the chamber is calculated. The pressure imposed on powders by hybridization is greatly affected by the geometry of the device, rotational speed of the blades and the material properties. In addition, some basic kinematic variables are estimated to give the overall picture of the flow distribution inside the chamber.

The numerical study is done on the system scale. Due to the large difference between the radii of host and guest particles in the system scale simulation, only the host

particles are taken into the consideration. Behavior of two different types of particles in the system is studied by performing the diagnostic analysis. The purpose of this system scale simulation is to understand the effects of different functional parameters vital for the effective operation of the hybridization system from the coating point of view.

3.2 Background

Discrete element method has been employed widely in the past to analyze flows involving particle motion inside a system subjected to high shear forces. Various industrial processes such as mixing, coating make use of many commercial devices such as Mechanofusion (Hosokawa), Hybridizer (Nara Machinery), where particles are rotated in a processing device running at very high speeds. For instance, the Mechanofusion and the Hybridizer are operated at the speeds as high as 3000 rpm and 15000 rpm respectively. The diagnostic analyses of the flow behavior inside the operating chambers hence become necessary to understand the effects of other parameters that affect the performance of these devices.

Many researchers have studied the experimental aspects of a machine operating on the similar principle as above. For instance, Yokoyama et al. (1987) has studied the dry coating method using a high shear mill commercially known as Mechanofusion. Honda et al. (1987) Masaru et al. (1996) have analyzed dry particle coating method using Hybridizer. Singh et al. (1997), Ramlakhan et al. (1998) investigated the magnetically assisted impaction-coating system. All these devices are based on the principle of high shear stress and impaction force, forcing the guest particles to get embedded onto the surface of host particles.

Though much attention has been given to the experimental studies of Hybridization system, very little literature is available for the numerical analyses of this system. Most particle dynamics simulations use the discrete element method. Discrete element method approach considers the particles as distinct and hence particles can be treated individually. Cundall and Strack (1979) developed a model based on this approach. The method is analogous to molecular dynamics simulation. The discrete element simulation of particles is more complicated because of the nonlinear and non-central inter-particle interactions arising from auto-adhesion, friction and presence of viscous fluid. The soft sphere approach is used to model this system.

Walton et al. (1986) used a three-dimensional discrete particle model to calculate inelastic, frictional granular flows. Good qualitative agreement has been achieved with experimental measurements and with theories when similar assumptions are made in the model. The same model has been used to simulate Hybridization system. Other recent work on DEM done by Kafui et al. (1993) includes the simulation of agglomerates impacting a wall. Lian et al. (1997) studied the pendular state wet agglomerates undergoing pair-wise collisions based upon soft sphere approach. By focusing the particle dynamics simulation only where it is used, this new technique can yield more than an order of magnitude increase in computational speed and number of particles, a system can deal with. It showed that DEM simulation is able to qualitatively reproduce features found in experimental data. However, DEM simulation did not perform well at low accelerations and the calculation of applied force based upon the work done was not entirely successful.

In the present study, the DEM model developed by Walton et al. (1986) is used and further modified to analyze the Hybridization system. Other relevant details of the DEM technique are already explained in the previous chapter.

3.3 Description of the Hybridization System

The hybridization system as shown in Figure 3.1 is primarily used for coating purposes, considers the host particles, which are bigger in size as compared to the guest particles, are mixed together and rotated in a high-speed rotation chamber. The guest particles are embedded onto the surface of host particles resulting in a dry particle coating. These guest and host particles are mixed simultaneously from the top of a circulating pipe as shown in Figure 3.2. The mixing chamber has six rotating blades, which typically rotate in the range of 5000 ~ 15000 rpm. As the rotor is switched on, host and guest particles mix and collide with each other as well as with the walls of the chamber. Due to high centrifugal forces, particles move to the upper part of the rotating chamber and recycle continuously till the end of the process.

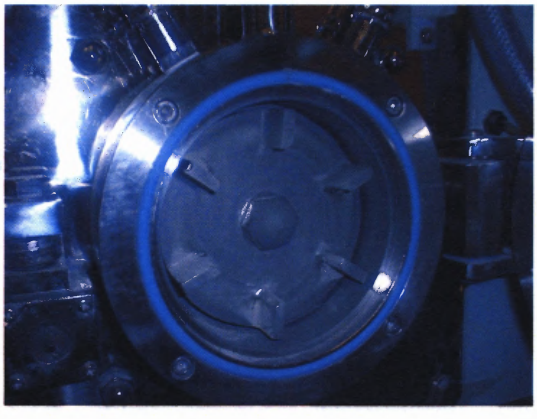

Figure 3.1 Mixing Chamber of Hybridization system.

Figure3.2 Recycling pipes and rotor with blades.

The hybridization system also has a temperature sensor, which monitors the temperature developed inside the mixing chamber during the operation. Typically, the batch size of a run during experimental studies varies from 15 to 30 gm depending upon the size and the density of particles. The unique feature of this system is the two-way motion of the particles during the operation, one in the mixing chamber and the other through the re-circulating pipe which provides a distinct advantage over the other dry coating machines from the coating point of view as one would expect more collisions between the particles to take place. The numerical model developed in this study is explained in the following section.

3.4 Numerical Model

A numerical model developed for the mixing chamber of hybridization system is shown in Figure 3.3. The exact modeling of the whole hybridization system including the re-circulating pipe is extremely complicated; hence in this study only the mixing chamber is modeled. As shown, the outer circle represents the outer wall of the mixing chamber. The blade mounted on the rotor is approximated as three overlapping cylinders. Particle is forced to leave the outer cylinder from the exit zone when it touches the predefined outer boundary and every particle going out is replaced with another particle generated at the outer boundary of the inner cylinder using a random number generator. While the simulation in 3-D, the front and back walls have periodic boundaries. Particles are mono-disperse, hence the guest particles are not considered explicitly. Also, dimension of the unit is smaller than the actual system to have the same volume fraction of particles used in the experiments.

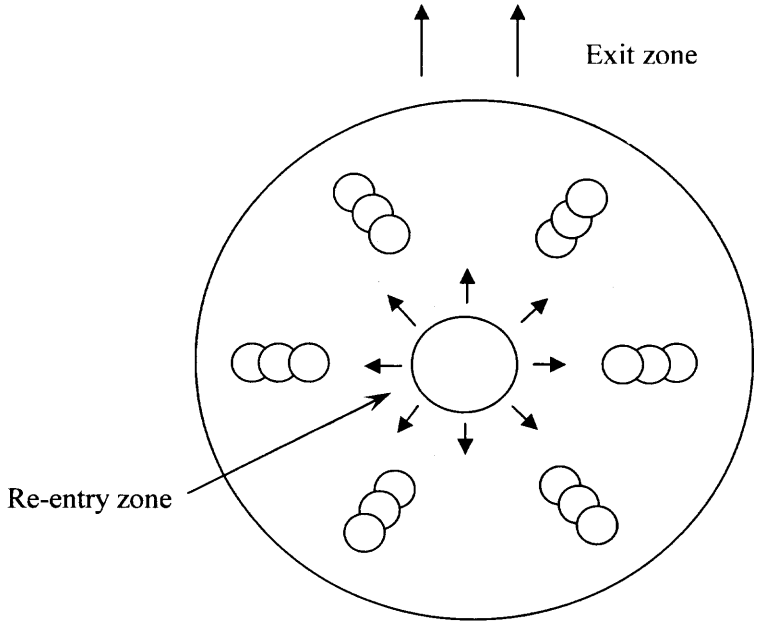

Figure 3.3 Simplified sketch of a numerical model of the system.

3.4.1 Force Model and Time Step

The accuracy of the any simulation depends upon the type of force model used in the numerical model as it determines the new positions and velocities of the particles after each time step. The detailed description of the force model used is already explained in chapter 2. The force model used here uses the Walton Braun approach. The particles are treated as frictional elastic-plastic. Normal force is computed using a partially latching spring model. The loading resistance force is calculated by linear spring with stiffness k_1. A stiffer spring resistance, k_2 is provided during the unloading (restoration) of particles during a collision, allowing a finite plastic deformation. The tangential force uses an incrementally slipping friction model. The new tangential force computed takes the loading history and direction into consideration.

The time step during the simulation is calculated by the following equation,

$$\Delta t = \pi e \frac{\sqrt{\frac{m}{2k_n}}}{n} \tag{3.1}$$

where e is the coefficient of restitution; m is the mass of particle; k_n is the spring stiffness during loading and n is the number of time steps desired during one collision. (For the simulations presented here, n = 40)

Equation 3.1 shows that the time step is proportional to the mass of particles as well as the coefficient of restitution and inversely proportional to the spring stiffness. Thus, if k is higher, the simulations require a long computational time. On the contrary, k_n cannot be too small which will make the particles too soft, resulting in the deformation of the particle during the simulation and thus exceeding the model limitations. Hence, the maximum deformation of the particle is taken to be less than 1% of the particle diameter. Therefore, based on the impact mechanics and the condition that maximum deformation is less than 1% of particle diameter, the normal stiffness is calculated by the following equation.

$$k_n = 0.01 \pi E r_i \tag{3.2}$$

where E is the Young's Modulus and r_i is the particle radius.

3.4.2 Zone Mapping

For diagnostic analyses, the mixing chamber of the hybridization system is divided into seven different zones as marked by concentric circles shown below in Figure 3.4. The

"averaged" zone is the radius of outer cylinder. Each zone has the same volume as calculated by $V_i = V/ N$, where V is the total volume of the system and N is the total number of zones. Number of zones is selected in such a way that the width of each zone is equal or greater than the maximum diameter of particles. This way it is ensured that at any given instant a particle cannot occupy more than two zones.

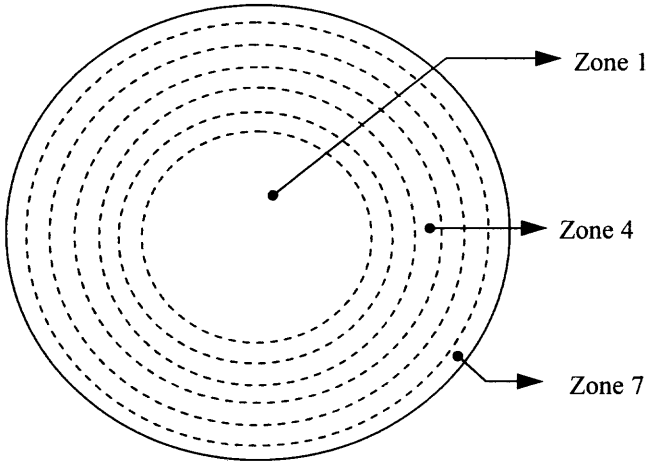

Figure 3.4 Zone mapping of the simulation system.

During the numerical simulation, the particles are considered to be frozen in each time step in order to compute the kinematic variables such as kinetic energy and pressure. If the particle i occupies two zones in a time instant, then the upper fraction belongs to zone k and the lower fraction belongs to zone k+1 as shown in Figure 3.5.

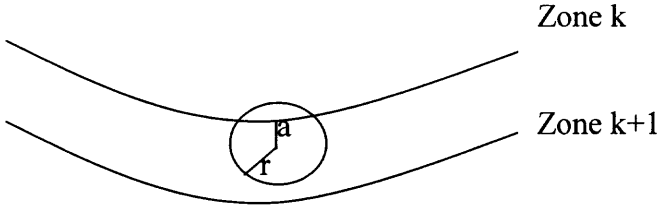

Figure 3.5 Volume fraction when two zones are occupied by the same particle i.

The distance of particle center to the zone k is represented as "a" and it is calculated by

$$a = l_{oi} - r_k \tag{3.3}$$

where l_{oi} is the distance of particle i's center to the chamber and r_k is the radius of zone k.

The volume of particle i in zone k is given as

$$V_k = \int_a^r \pi x^2 dy = \frac{2\pi}{3} r^3 - \pi a \left(r^2 - \frac{1}{3} a^2 \right) \tag{3.4}$$

where, r is the radius of particle and $x = \sqrt{(r^2 - y^2)}$

Therefore the volume fraction of particle i in zone k is given by

$$rpos\ (i) = \frac{V_k}{V_t} = \frac{\frac{1}{2} V_t - \pi a \left(r^2 - \frac{1}{3} a^2 \right)}{V_t} \tag{3.5}$$

where V_t is the volume of particle i.

Volume fraction of particle I in the zone k+1 is equal to

$$rneg\ (i) = 1 - rpos\ (i) \tag{3.6}$$

3.4.3 Simulation Method

During the simulation, the blades are considered as boundary particles and these boundary particles interact with the system particles. Initially, particles are randomly placed inside the system domain with some initial overlap allowed. However, the overlap between the system particles and boundary particles is not allowed. The initial velocities are assigned to the particles by keeping the net momentum of the system equal to zero. Inter-particle forces are computed for all the particles using a force model, during each

time step. The gravity is applied in y-direction. The new translational as well as the rotational acceleration is computed using Newton's law of motion.

$$\dot{v}_x^n = \frac{F_{ix}^n}{m}$$
$$\dot{\omega}_x^n = \frac{M_{ix}^n}{I} \tag{3.7}$$

where the superscript n refers to the current time step; $m = \frac{1}{6}\pi d^3 \rho$; $I = \frac{1}{10} m d^2$

m is the particle mass, d is the particle diameter and I is the particle moment of Inertia. F_{ix} and M_{ix} are the inter-particle force and the moment acting on the particle due to the interaction with other particle.

Similar equations can be written for other directions as well. The new velocities and positions of the particles can be calculated by explicit integration of the equation 3.7 via time-centered, finite difference "leap-frog" method. The finite difference equations for the particle are given as follows.

$$v_x^{n+1/2} = v_x^{n-1/2} + \dot{v}_x^n \Delta t$$
$$\omega_x^{n+1/2} = \omega_x^{n-1/2} + \dot{\omega}_x^n \Delta t \tag{3.8}$$

The equation 3.8 gives the translational and rotational velocities and the new positions are updated by

$$x^{n+1} = x^n + v_x^{n+1/2} \Delta t \tag{3.9}$$

Equations 3.8 and 3.9 are for the x-directions. Again, similar equations can be written for other directions. After computing new positions and velocities, the contact forces and the new positions of particles are updated, and the new contacts as well as the broken

contacts are also updated. This cycle is repeated until the end of simulation. Meanwhile, diagnostic quantities are computed.

3.5 Diagnostic Analyses

3.5.1 Parameters for the Numerical Study

In the numerical studies, first, the simulation of the hybridization system was done for two different sets of particles. The parameters for this study are given in the Table 3.1. Simulations were carried out for different system parameters such as density of particles, particle diameters etc. Results are presented below. The first set of simulation was carried out for 75 microns diameter magnesium particles (density 2500 kg/m$^{3)}$ rotated at 5000 rpm. The second set of simulation was run for dense titanium particles with density 5000 kg/m^3. Particle diameter was taken as 400 microns. The numbers of particles used were 1500, simulation run time being 1~2-sec. Different kinematic variables for pressure distribution inside the mixing chamber, rotational kinetic energy, and total energy are computed and presented in the next section. Also, the inter-particle forces and the collisions are computed for the first set of particles.

The quantities of interest for the diagnostic analysis of the system are the time-averaged values. The time over which average is taken must be long enough compared to the typical time taken by any particle interaction, for example particle-particle or particle-wall interaction. But, at the same time it should be short compared to the time scale of changes of the major properties of the particles of interest.

Table 3.1 Parameters for the Simulation

Radius of particles	75, 400 microns
Number of particles	1000-1500
Density of particles	3.5 g/cc
Outer cylinder radius	0.075m
Inner cylinder radius	0.015m
Rotational speed	5000, 6000, 8000, 10000 rpm
Normal stiffness	2000 kg/s^2
Coefficient of friction	Particles: 0.4 wall: 0.8
Coefficient of restitution	0.85

3.5.2 Snapshots

The snapshots of the simulated system of magnesium (lighter) particles and the titanium (heavier) particles are shown in Figures 3.6 and 3.7, respectively. The differences in the positions of particles for these two different types of simulated systems are evident. As clear from Figure 3.6, as the simulation starts, initial drag is observed due to the sudden motion of blades. The particles tend to follow the motion of the blades and the system becomes stabilized after a short time. The overall position of the particles is random and there is no typical trend observed. On the contrary, for the system of heavier particles, as shown in Figure 3.7, after initial motion of particles, the system tends to settle down

under the force of gravity and due to the inertia of particles. After about 0.2 seconds of simulation, particles seem to be settling down in the gap of blades and outer chamber. The same trend was also observed during the experiments, when the heavy particles were used to carry out coating. After the experiment, very few of particles were seen to be coming out of the product pipe and majority of the particles were seen to be settled down in the gap of the blade and the mixing chamber as well as in the re-circulation tube.

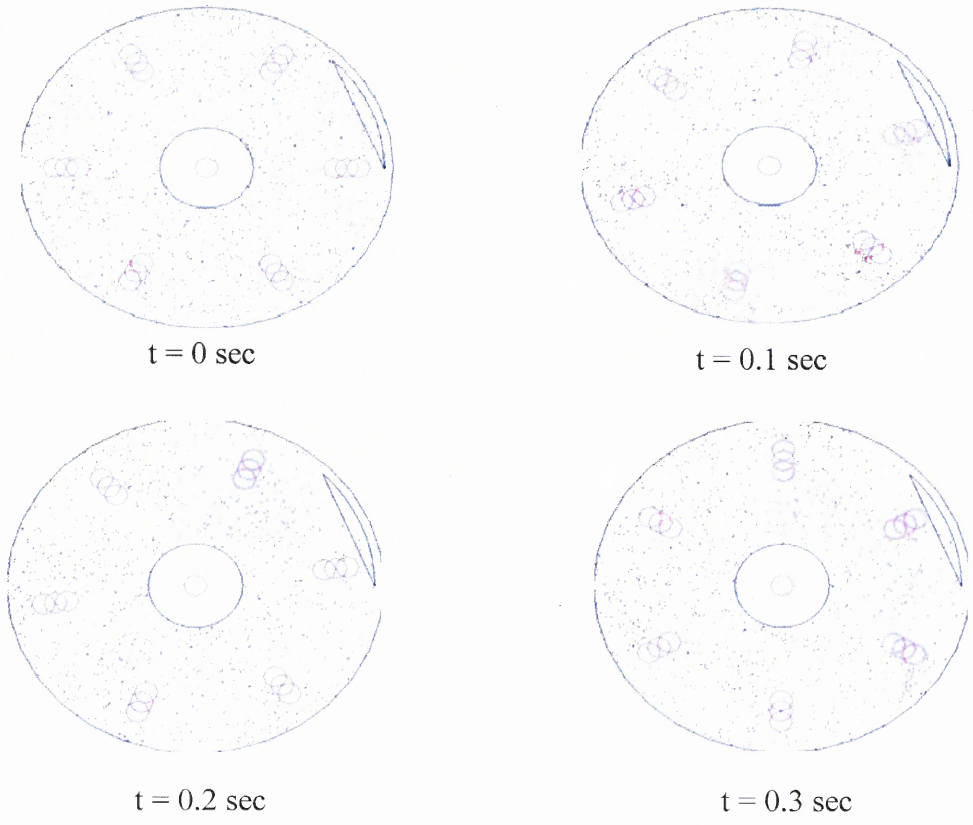

Figure 3.6 Snapshots of the system of lighter particles.

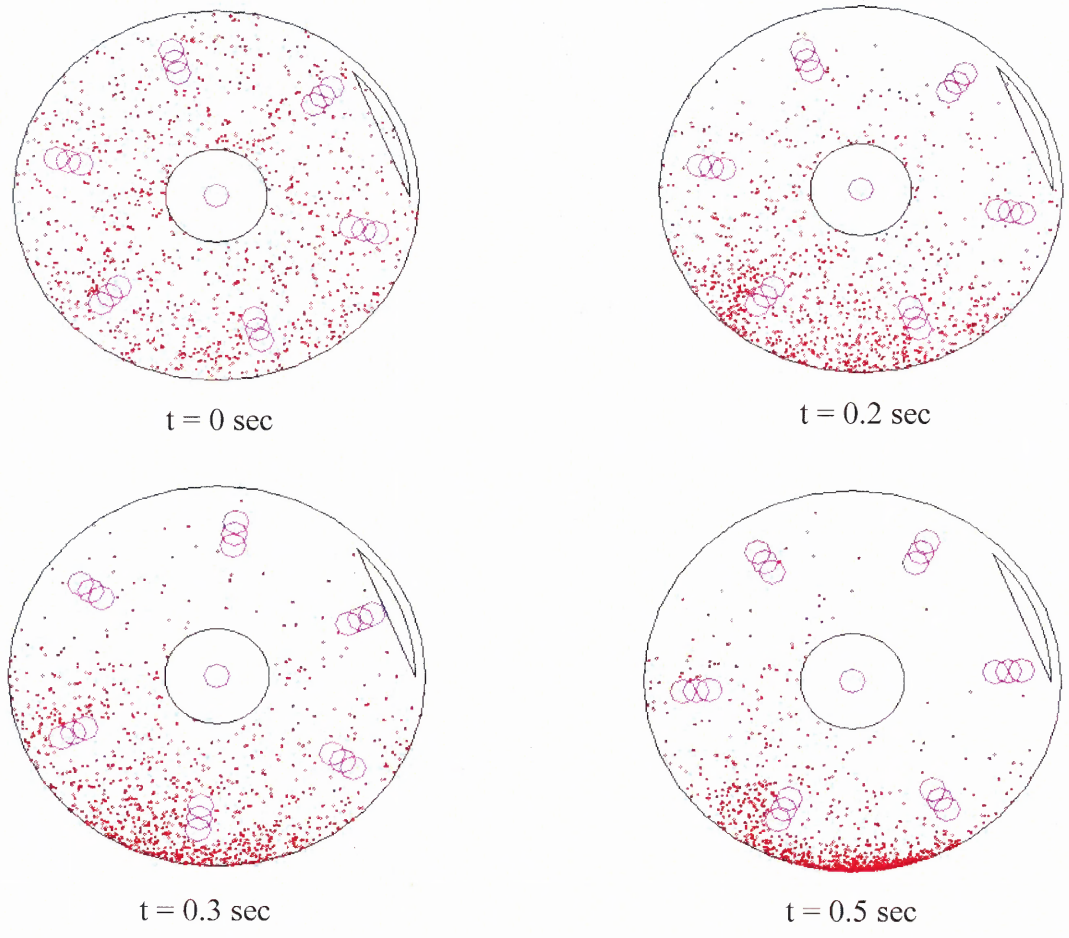

Figure 3.7 Snapshots for the system of heavier particles.

The snapshots of particles inside the system show qualitatively the difference between the system of lighter and heavier particles affecting the performance of the hybridization system. In order to get quantitative understanding, the kinetic energy, pressure etc. are computed and presented in the following sections. For these two systems, diagnostic analysis is carried out to understand the dynamic condition inside the system. Each diagnostic quantity is a volume average inside each zone during a time period.

3.5.3 Rotational Kinetic Energy, Total Energy and Pressure Distribution

Rotational kinetic energy of particles inside zone k is given by

$$E_r^{(k)} = \frac{1}{2V_k} \sum_{i \in k} I_i \left(\omega_{ix}^2 + \omega_{iy}^2 + (\omega_{iz}^2 - \omega^2) \right) \tag{3.10}$$

where V_k is the volume of zone k, ω is the rotational speed of the system, ω_{ix}, ω_{iy}, ω_{iz} are the components of angular velocity of particle i, which falls in zone k during that time instant. $I_i = \frac{2}{5} m_i r_i^2$ is the moment of inertia and m_i and r_i are the mass and radii of particle i.

Total energy inside the system is calculated using following relation

$$E_p = \frac{1}{V} \sum_i \sum_j \left(F_{ij} (\alpha_{ij} - \alpha_{ij_0}) \right) \tag{3.11}$$

Where, V is the volume of cell, α_{ij} is the relative displacement of particles i, j during time instant, and α_{ij0} is the deformation after unloading. Similarly pressure distribution inside the chamber in each zone with respect to time is calculated using an empirical relation deduced by Ladd P (1998) given in equation (3.12) as below,

$$P = \frac{1}{3V_i} \left[\sum_{i \in k} m_i v_i^2 + \sum_{i \in k, i > j} F_{ij} R_{ij} \right] \tag{3.12}$$

where, V_i is the volume of that zone, F_{ij} is the repulsive force between particles i and j and R_{ij} is the distance between two particles i and j. The first term in above equation

represents the kinetic contribution to the granular pressure due to the motion of particles corresponding to the average velocity field of particle i, and the second term is the potential or collisional contribution to the pressure due to the forces of interaction between particles.

Plots for pressure distribution, rotational kinetic energy and total energy are shown from Figures 3.8-3.10 for the system of lighter particles.

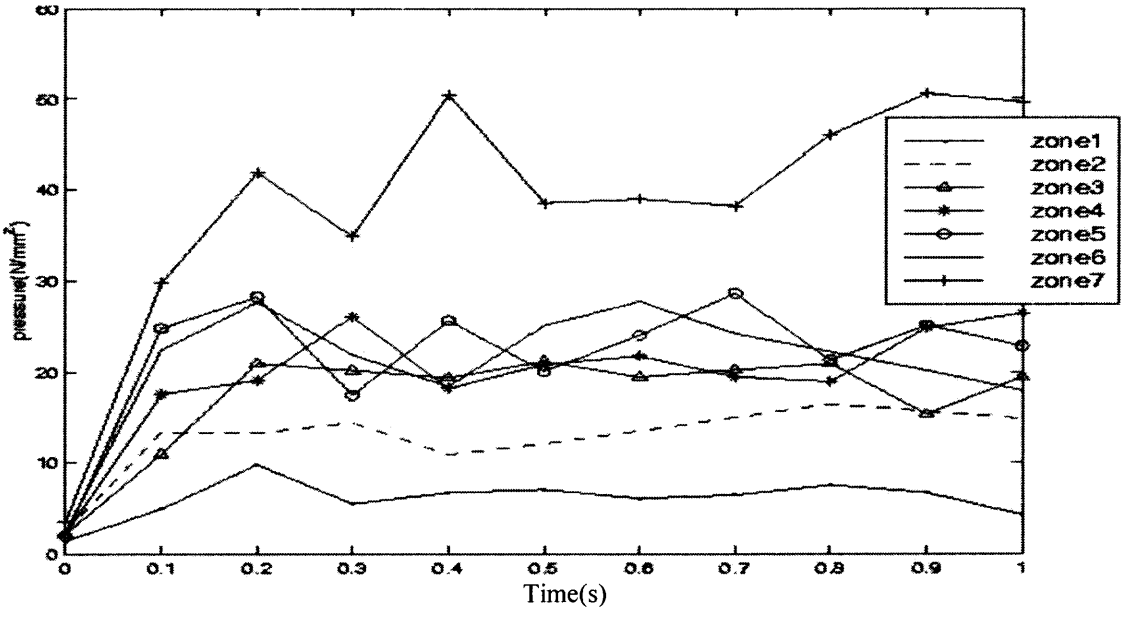

Figure 3.8 Pressure distributions across the chamber for the system of lighter particles.

From the estimation of these kinematics variables, it is seen that initially in the transit zone till about 0.2 seconds, particles reach the maximum velocities, pressure and energy and then the system is stabilized. A steady state condition is reached, which may be due to the particles following the motion of the rotating blades inside the chamber.

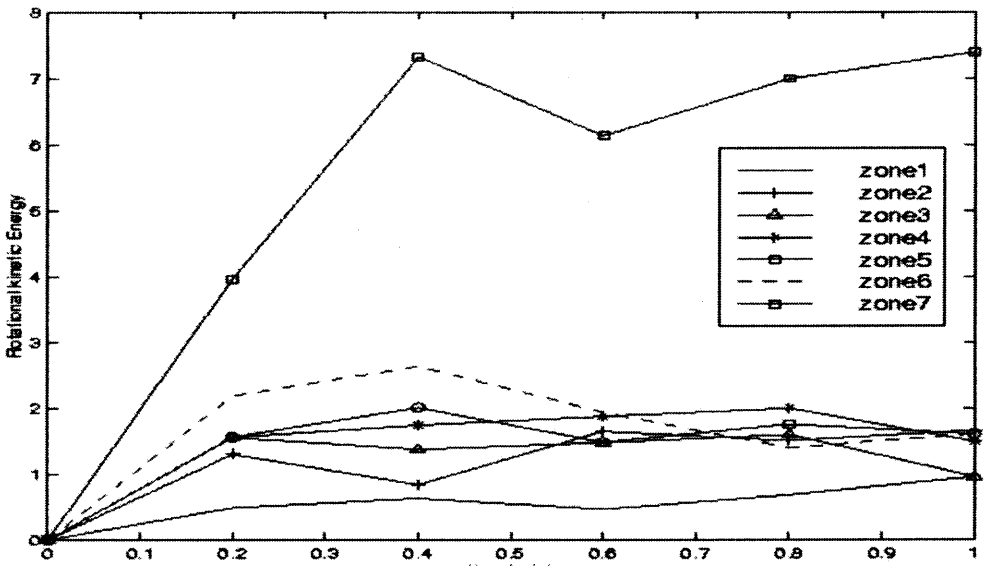

Figure 3.9 Rotational Kinetic Energy across different chamber for heavier particles.

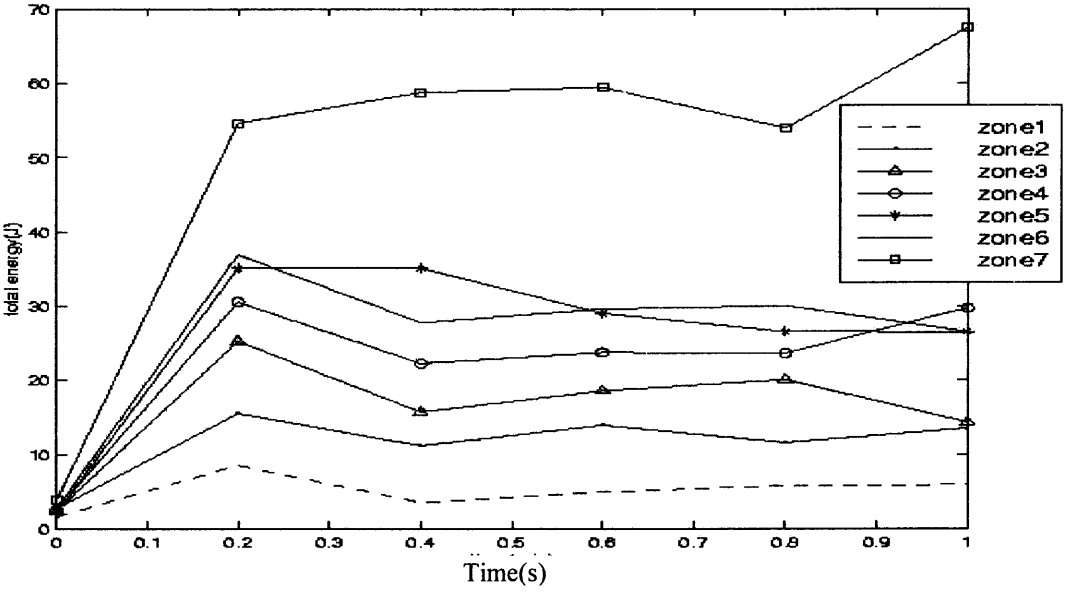

Figure 3.10 Total Energy across different chamber for lighter particles.

Pressure distribution and energies are higher in the outermost zone due to the centrifugal action as well as the higher number of collisions taking place with the outer wall of the rotating chamber.

In case of heavier particles, the particles picked up high velocities, and energies at the start of the run due to the inter-particle collisions but as the time increased, settled down in the clearance between the rotating blades and the outer chamber resulting into nearly zero values. Results are shown from Figures 3.11-3.13.

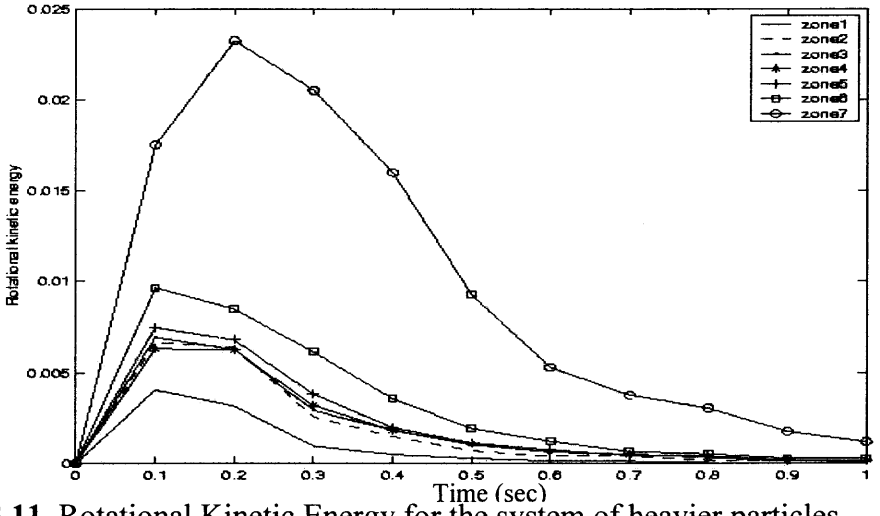

Figure 3.11 Rotational Kinetic Energy for the system of heavier particles.

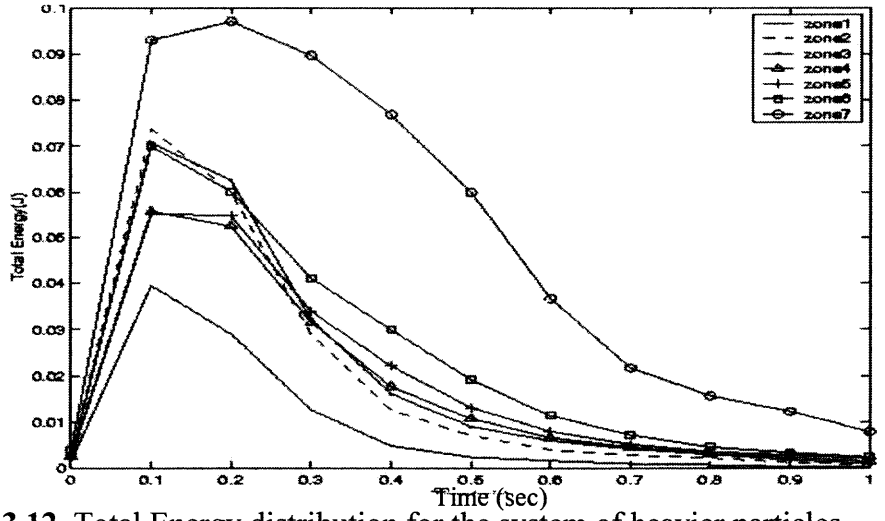

Figure 3.12 Total Energy distribution for the system of heavier particles.

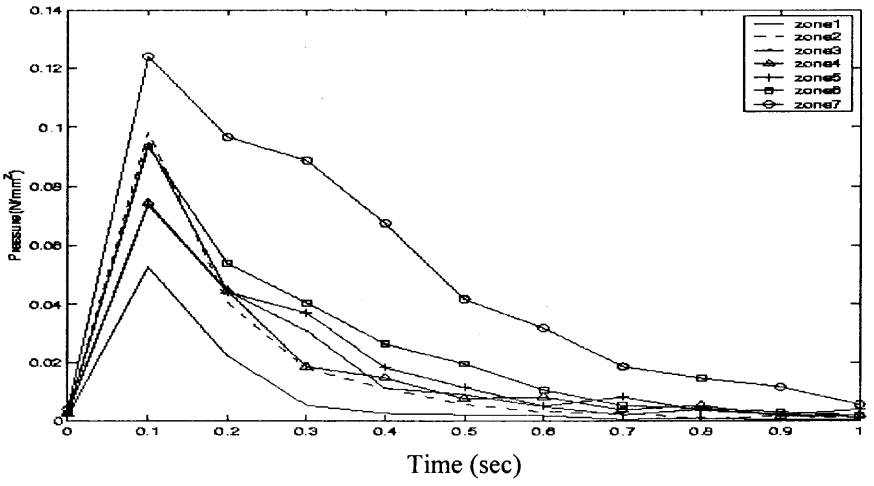

Figure 3.13 Pressure distribution for the system of heavier particles.

When these two sets of conditions were simulated as explained above, it was observed that particles fall down in the chamber due to gravity. It may be noted that these simulations were carried out assuming vacuum inside the chamber. Hence, as the density of particles is increased, particles seem to be settling down in to the narrow gap between the outer cylinder and the blades mounted on the rotating disc.

3.5.4 Collisions Analyses

In order to understand the behavior of Hybridization system under different operating conditions such as loading and rotational speeds, number of collisions as well as the forces inside the particulate system were analyzed. It is obvious that the inter-particle interactions as well as the magnitude of the impact of particles inside the system are the key parameters to the coating process occurring in the hybridization system. Therefore, estimation of these quantities provides vital information from the coating point of view. As shown in Figure 3.14, cumulative number of particle-particle collisions is computed for different loading conditions for 500, 600, 800 and 1000 particles. The rotational speed for this run was 10000 rpm. As seen the number of collisions showed a gradual and

uniform increasing trend as the simulation time increased. As the simulation was started, the increase in the number of collisions was seen to be in the similar range for the case of 500, 600 and 800 particle loading. As the run time progressed, the number of collisions was observed to be increasing at the higher rate for higher loading of particles. At the end of 0.5 seconds, the total number of cumulative collisions was seen to be increasing exponentially as the loading was increased from 500 to 1000 particles. Collisions were computed in the range of 10^{10}.

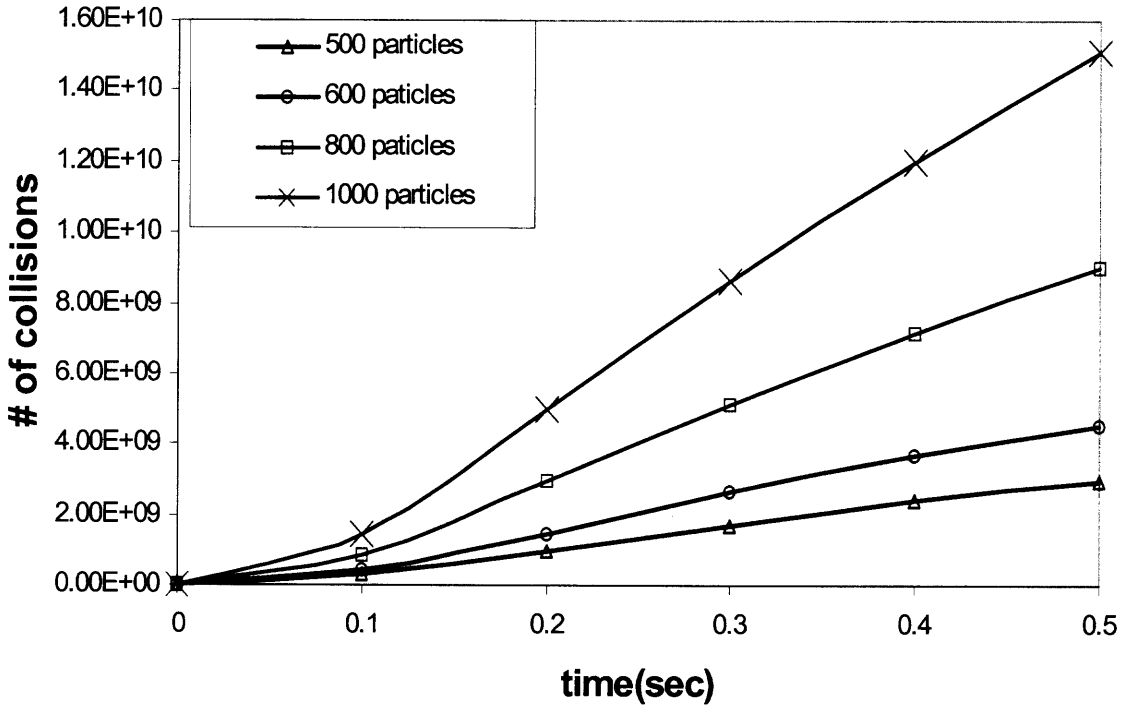

Figure 3.14 Particle-Particle collisions at 10000 rpm.

The number of collisions was seen to be increasing with the increase in the rotational speed. (Figure 3.15) For each case of loading of particles, the total number of collisions was increased by 19% at the end of simulation time going from 5000 to 10000 rpm.

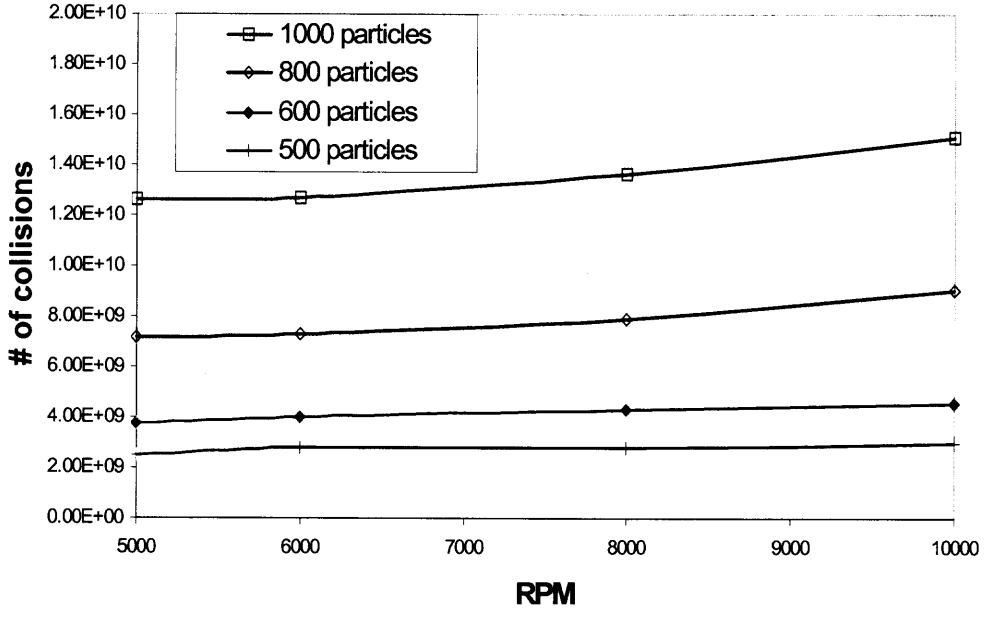

Figure 3.15 Number of particle-particle collisions for different rotational speeds.

In order to see the behavior of particles colliding with the boundaries of the system as well as with the blades of the wall, simulations were carried out for the different loadings and rotational speeds as above. The results in Figure 3.16 and 3.17 show that the total number of particles- boundary cumulative collisions was more than that of the particle-particle collisions by the order of 10^4.

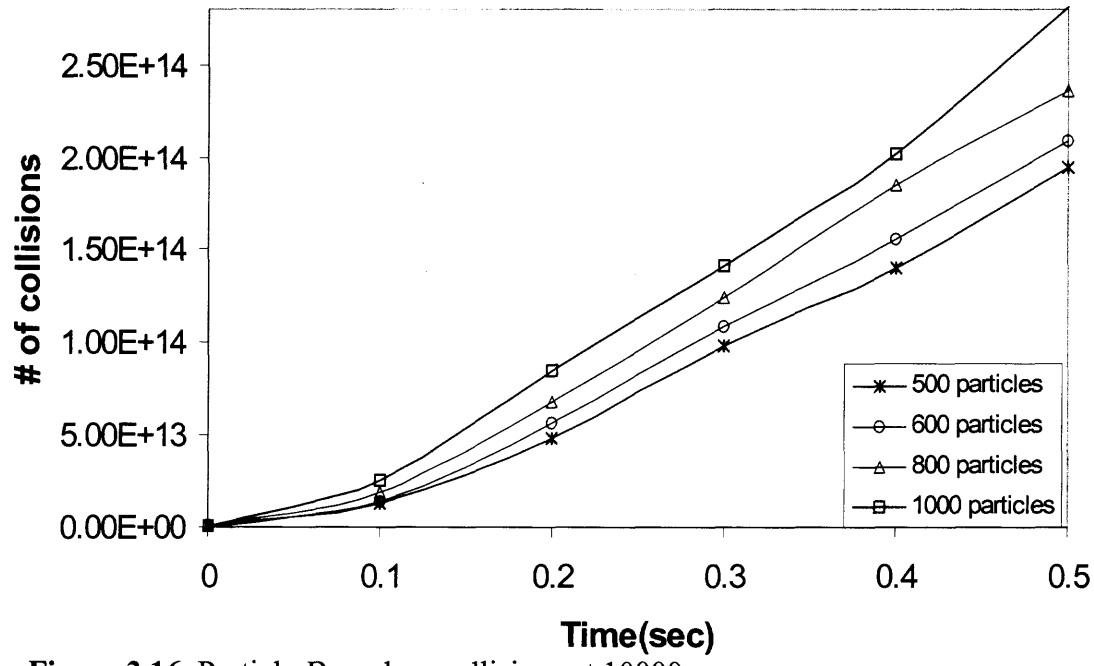

Figure 3.16 Particle-Boundary collisions at 10000 rpm.

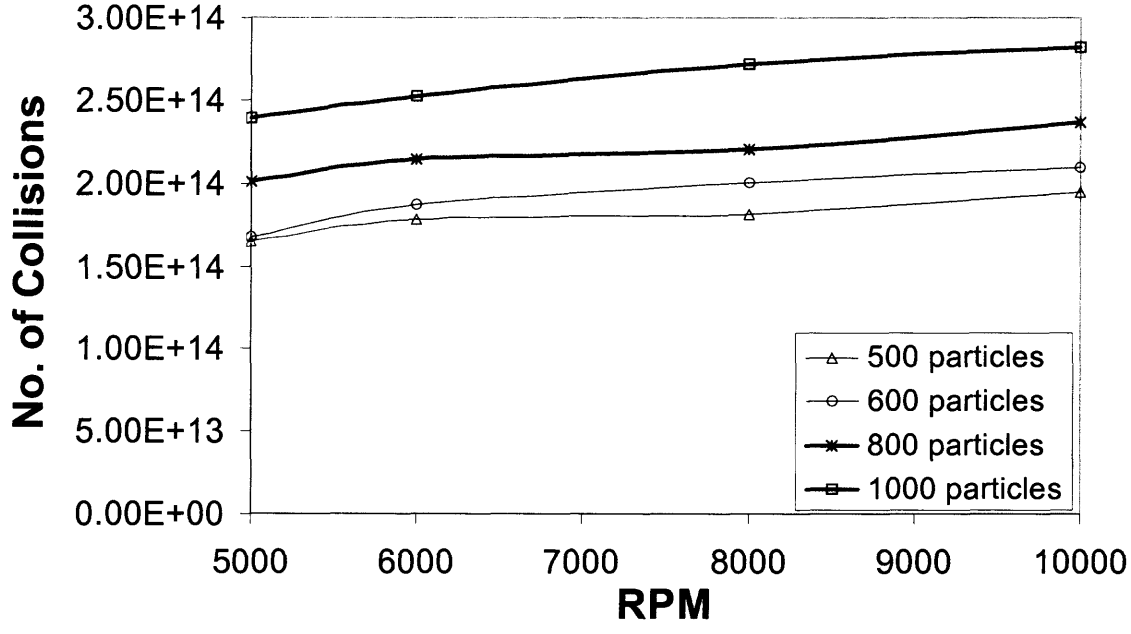

Figure 3.17 Particle-Boundary collisions for different rotational speeds.

The gradual increasing trend in the number of collisions was not as uniform as seen in the case of particle-particle collisions, though the total number of collisions was more. Similarly, an increase of 16%-18% in the number of collisions was recorded with the increase in the rotational speed, as seen in the case of particle-particle collisions.

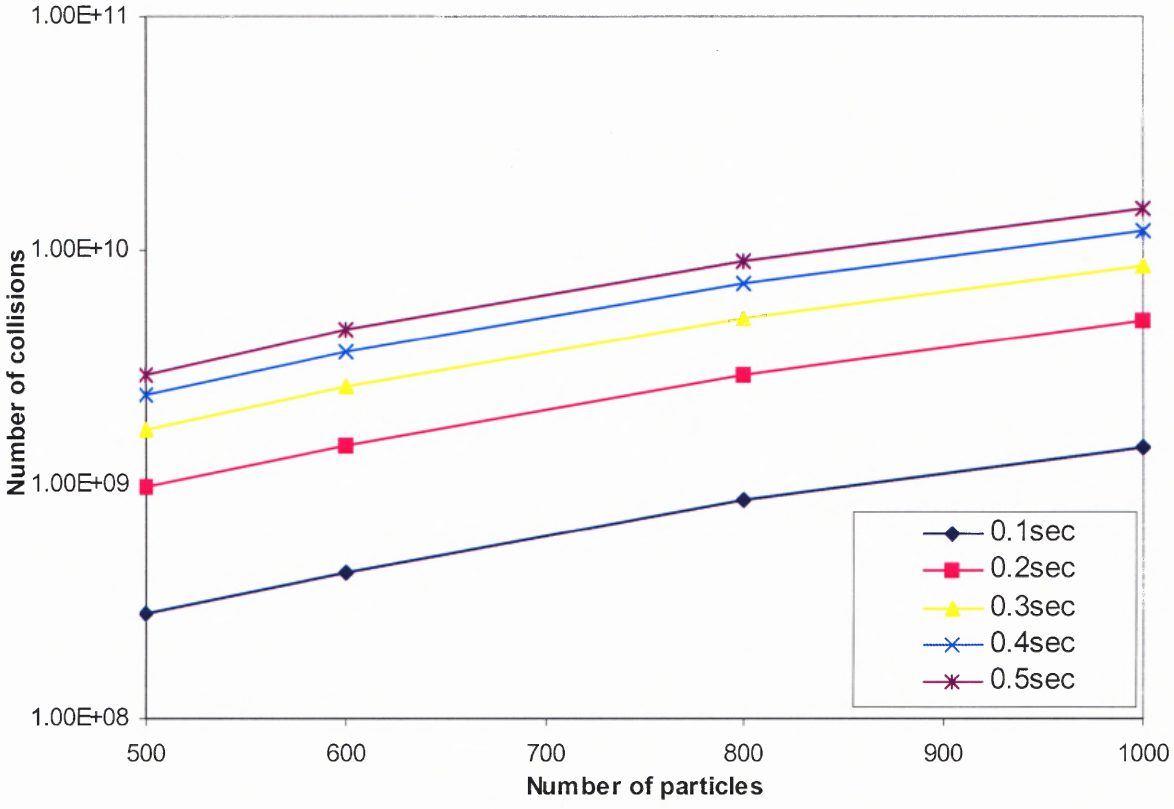

Figure 3.18 Particle-Particle interactions at 10000rpm for different loading of particles.

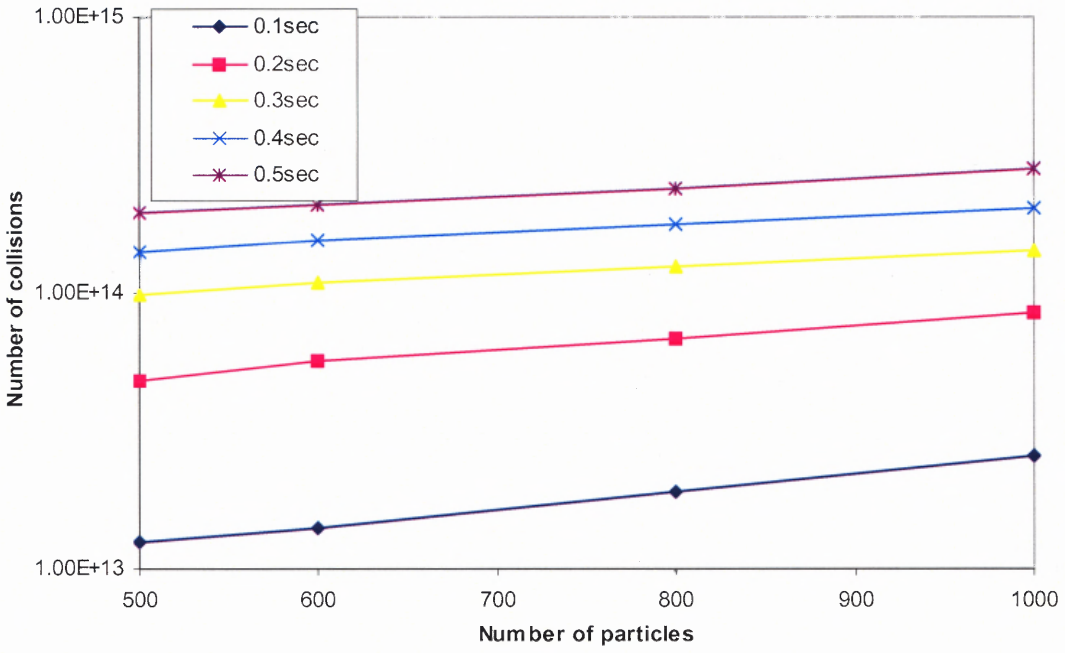

Figure 3.19 Particle-Boundary interactions at 10000rpm for different loading of particles.

Particle-particle and Particle-boundary interactions with respect to different loading of particles for the rotational speed of 10000 rpm are also computed and shown in Figure 3.18 and 3.19, respectively. The difference in the trend of curves is evident. Particle-particle collisions increases at lower rate as compared to particle-boundary interactions. Also, as the simulation time is increased, the rate of increase of interactions in both the cases seems to gradually decreasing.

Thus, overall the interactions of particles with the boundary and with the particles are computed, which explains some basic phenomenon happening inside the system.

3.5.5 Forces

Computations of forces inside the mixing chamber of the Hybridization system were carried out in order to understand the impact of particles on one another. Tangential forces and normal forces were computed for different loadings and rotational speeds. These forces are the long-term average values and are obtained by all the instant values during the simulation. As seen (Figure 3.20) in case of tangential forces, the forces were seen to be in the range of 10^{-3} N. Forces were higher for the higher loading cases.

Up to 8000 rpm, the forces for the loading cases of 500, 600 and 800 particles were seen to be in the similar range. At 10000 rpm and 1000 particles loading case, the tangential forces were particularly seen to be very high as compared to other loading cases. On the other hand, in the case of normal forces (Figure 3.21), there was not much significant change observed as the loadings and rotational speeds changed, which means the tangential forces had an important role in the operation of the system. However, the normal force was seen to be much higher than the tangential forces, which was in the range of 10^{-2}.

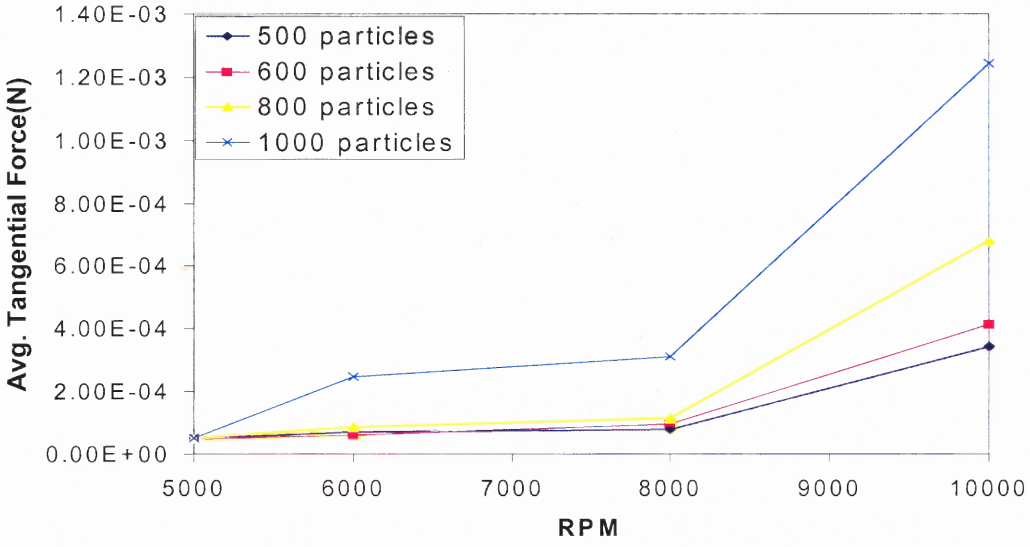

Figure 3.20 Average Tangential Force Analysis.

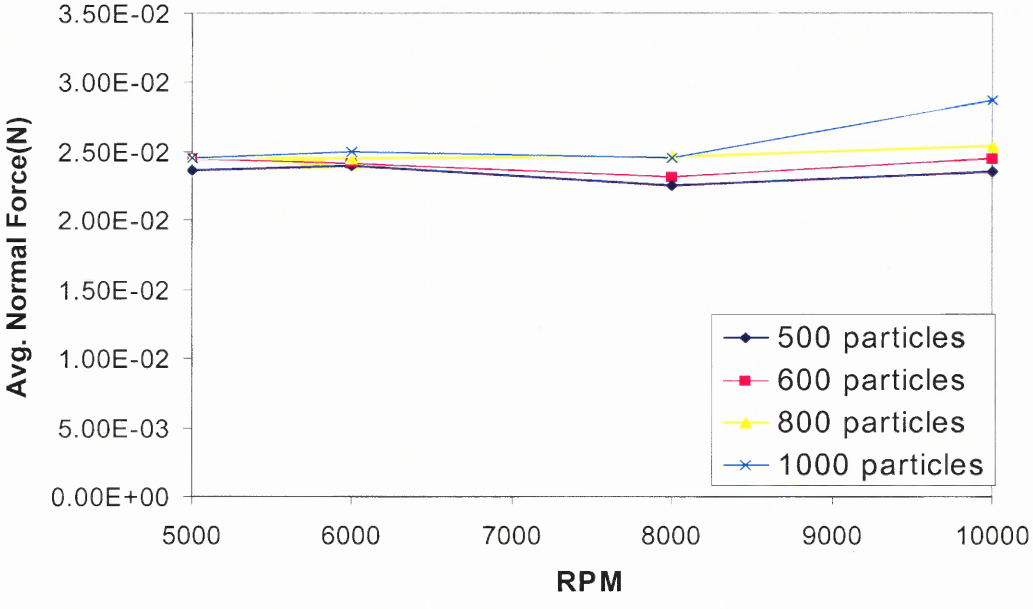

Figure 3.21 Average Normal Force Analysis.

The results of DEM shown in the sections above are computed from the smaller size of the hybridizer system where the rotational speed is varied from 5000 to 10000 rpm. However, in the reality, the scale up/down of any hybridization system is based on the idea of keeping the tip velocity of the blade constant. Further detailed analysis of this smaller system is shown in Chapter 5, in order to understand the change in the behavior of the system under the effect of air-drag. Also the original size system is also studied for the rotational speeds of 5000 and 10000 rpm. Velocities of particles obtained from this original size system are then compared to the velocities obtained from the fluid code, which is also explained in details.

3.6 Conclusions

Numerical simulation of hybridization system based upon Discrete Element Method is presented in this chapter. The numerical modeling is carried out based on the approach by Walton-Braun's partially latching spring model. The simulation clearly provides valuable information about the different operating parameters affecting the performance of the system. Two different sets of particles are studied and a diagnostic analysis is carried out. Heavier particles settle down in the system without going through the re-circulation tube. The lighter particles are randomly positioned at the end of simulation inside the system, which also tend to settle down in the system as seen by the reduction in the rate of number of collisions with the time. Computations of forces for different rotational speeds are shown. The normal forces seem to be dominant than the tangential forces. Normal forces do not have much effect on either the loading or rotational speeds. Tangential forces seem to be increasing with the rotational speeds as well as the loading of particles.

Particle-particle interactions as well as the particle-boundary interactions are also computed which demonstrates the frequency of collisions happening inside the system for different operating parameters. Particle-boundary interactions are more than particle-particle interactions. Rate of increase of particle-particle interactions is less than that of particle-boundary interactions. The increase in the number of collisions for both particle-particle as well as particle-boundary interactions is equal to nearly 18%, when the rotational speed of the hybridization system is doubled.

Since the blades of the hybridizer are rotating at high speeds, there is a formation of air-draft, which assists the particles to force their way to the re-circulation tube. In order to avoid the hybridization system from settling down, this induced air-draft due to the blades needs to be analyzed, which plays a very important role in the re-circulation of the particles through the re-circulation tube. Analysis of airflow using different CFD techniques inside the mixing chamber is therefore carried out in the next chapter.

CHAPTER 4

FLUID ANALYSIS OF HYBRIDIZATION SYSTEM

Numerical simulation of airflow field induced due to the high-speed rotating blades inside the mixing chamber of hybridization system is carried out and the results of single-phase flow are presented in this chapter. Importance of airflow field inside the hybridization system and its effect on the pattern of particles necessitates the calculations of quantities such as velocity flow fields/contours, pressure distribution, temperature, and forces due to the airflow on blades. Computational fluid dynamics techniques are used to compute the airflow field inside the mixing chamber of the hybridization system. The flow field using a three dimensional fluid code developed by Tsingua University as well as the commercial fluid analysis software, Fluent is computed. Numerically computed air velocities are then compared with the experimental data. The effect of different rotational speeds of the blades on the airflow field is also analyzed.

4.1 Introduction

Numerical simulation of three-dimensional incompressible flow problems using Reynolds-averaged Navier-Stokes equations are now becoming more feasible in many theoretical analyses and engineering applications. In many real flow problems, such as the flows in the impeller passage of turbo-machinery, and the flows in hybridization systems with rotating blades, the boundary geometries are so complex that it is much more accurate to describe the problems using body-fitted coordinate systems, which is also convenient from the computer programming point of view.

The main difficulty and feature of solving incompressible flow problems is to find a way to obtain a pressure field such that the flow field can be close to divergence-free as much as possible. In another words, the mass conservation law should be satisfied. Generally, there are two kinds of approaches, first is to employ the pseudo-compressibility approach and time-iterative scheme to generate the pressure field so that the continuity equation is satisfied when a steady state is reached. Second way is to apply a pressure-velocity correction scheme by using a Poisson's equation for pressure correction derived from the continuity and momentum equations for which grid staggering between velocity vectors and the pressure nodes must be used to ensure numerical stability.

There are several possible grid staggering methods that are discussed by Maliska and Raithby (1984). In the present work, the method of grid staggering developed by Vanka (1980) and Maliska (1984) is employed in which the same control volume is used for velocity components and scalar quantities. Thus, the problem of solving the velocity components and scalar quantities using different control volumes is avoided. In addition, for turbulent flow computations, the numerical code uses the standard k-ε turbulence model (1972) to provide the turbulent eddy viscosity.

4.2 Numerical Method

4.2.1 Governing Equations

For incompressible Newtonian fluid, the continuity, momentum and energy equations with standard k-ε turbulence model in Cartesian coordinate system rotating around z axis with rotating speed ω can be written as:

$$U_t + E_x + F_y + H_z = S \tag{4.1}$$

where $$U = \begin{bmatrix} \rho & \rho u & \rho v & \rho w & \rho k & \rho \varepsilon \end{bmatrix}^T \tag{4.2}$$

$$E = \begin{bmatrix} \rho u \\ \rho uu - \mu_{eff} u_x \\ \rho uv - \mu_{eff} v_x \\ \rho uw - \mu_{eff} w_x \\ \rho uk - \mu_{eff} k_x / \sigma_k \\ \rho u\varepsilon - \mu_{eff} \varepsilon_x / \sigma_\varepsilon \end{bmatrix} \quad F = \begin{bmatrix} \rho v \\ \rho vu - \mu_{eff} u_y \\ \rho vv - \mu_{eff} v_y \\ \rho vw - \mu_{eff} w_y \\ \rho vk - \mu_{eff} k_y / \sigma_k \\ \rho v\varepsilon - \mu_{eff} \varepsilon_y / \sigma_\varepsilon \end{bmatrix} \quad H = \begin{bmatrix} \rho w \\ \rho wu - \mu_{eff} u_z \\ \rho wv - \mu_{eff} v_z \\ \rho ww - \mu_{eff} w_z \\ \rho wk - \mu_{eff} k_z / \sigma_k \\ \rho w\varepsilon - \mu_{eff} \varepsilon_z / \sigma_\varepsilon \end{bmatrix}$$

$$S = \begin{bmatrix} 0 \\ (\mu_{eff} u_x)_x + (\mu_{eff} v_x)_y + (\mu_{eff} w_x)_z - p_x + 2\omega v + \omega^2 x \\ (\mu_{eff} u_y)_x + (\mu_{eff} v_y)_y + (\mu_{eff} w_y)_z - p_y - 2\omega u + \omega^2 y \\ (\mu_{eff} u_z)_x + (\mu_{eff} v_z)_y + (\mu_{eff} w_z)_z - p_z \\ \rho(P_r - \varepsilon) \\ \rho\varepsilon(C_1 P_r - C_2 \varepsilon)/k \end{bmatrix} \tag{4.3}$$

The effective viscosity can be calculated from

$$\mu_{eff} = \mu + \mu_t = \mu + \rho C_\mu k^2 / \varepsilon \tag{4.4}$$

The turbulent kinetic energy production term is defined as

$$\Pr = C_\mu[(u_y + v_x)^2 + (v_z + w_y)^2 + (w_x + u_z)^2 + 2(u_x^2 + v_y^2 + w_z^2)]k^2 / \varepsilon \tag{4.5}$$

The constants of the turbulence model are

C_μ=0.09, σ_k=1.0, σ_ε=1.3, C_1=1.44, C_2=1.92

where $\rho, p, k, \varepsilon, \mu, \mu_t$ are the density, pressure, turbulent kinetic energy, turbulent kinetic energy dissipation rate, molecular viscosity and turbulent eddy viscosity of the fluid respectively. Also, u, v, w are the components of velocity in *x, y,* and *z* directions respectively.

Transforming equation (4.1) to a general curvilinear coordinate system (ξ, η, ζ) results in the following equation:

$$U_t + E_\xi \xi_x + E_\eta \eta_x + E_\zeta \zeta_x + F_\xi \xi_y + F_\eta \eta_y + F_\zeta \zeta_y + G_\xi \xi_z + G_\eta \eta_z + G_\zeta \zeta_z = S \quad (4.6)$$

where,

$\xi_x = J(y_\eta z_\zeta - y_\zeta z_\eta)$, $\xi_y = -J(x_\eta z_\zeta - x_\zeta z_\eta)$, $\xi_z = J(x_\eta y_\zeta - x_\zeta y_\eta)$,

$\eta_x = -J(y_\xi z_\zeta - y_\zeta z_\xi)$, $\eta_y = J(x_\xi z_\zeta - x_\zeta z_\xi)$, $\eta_z = -J(x_\xi y_\zeta - x_\zeta y_\xi)$,

$\zeta_x = J(y_\xi z_\eta - y_\eta z_\xi)$, $\zeta_y = -J(x_\xi z_\eta - x_\eta z_\xi)$, $\zeta_z = J(x_\xi y_\eta - x_\eta y_\xi)$,

$J = [x_\xi (y_\eta z_\zeta - y_\zeta z_\eta) - x_\eta (y_\xi z_\zeta - y_\zeta z_\xi) + x_\zeta (y_\xi z_\eta - y_\eta z_\xi)]^{-1}$.

The transformation coefficients $\xi_x, \xi_y, \xi_z, \eta_x, \eta_y, \eta_z, \zeta_x, \zeta_y$ and ζ_z are computed using second-order central difference setting the grid sizes $\Delta\xi$, $\Delta\eta$ and $\Delta\zeta$ to be unity which can simplify the computation of the transformation coefficients.

4.2.2 Discretization of the Basic Equations

The governing equation (4.6) can be represented by the following model transport equation in which φ denotes all the dependent variables, and Γ the diffusion coefficient

$$(\rho\phi)_t + [\rho u\phi - \Gamma(\phi_\xi\xi_x + \phi_\eta\eta_x + \phi_\zeta\zeta_x)]_\xi\xi_x + [\rho u\phi - \Gamma(\phi_\xi\xi_x + \phi_\eta\eta_x + \phi_\zeta\zeta_x)]_\eta\eta_x$$
$$+ [\rho u\phi - \Gamma(\phi_\xi\xi_x + \phi_\eta\eta_x + \phi_\zeta\zeta_x)]_\zeta\zeta_x + [\rho v\phi - \Gamma(\phi_\xi\xi_y + \phi_\eta\eta_y + \phi_\zeta\zeta_y)]_\xi\xi_y$$
$$+ [\rho v\phi - \Gamma(\phi_\xi\xi_y + \phi_\eta\eta_y + \phi_\zeta\zeta_y)]_\eta\eta_y + [\rho v\phi - \Gamma(\phi_\xi\xi_y + \phi_\eta\eta_y + \phi_\zeta\zeta_y)]_\zeta\zeta_y$$
$$+ [\rho w\phi - \Gamma(\phi_\xi\xi_z + \phi_\eta\eta_z + \phi_\zeta\zeta_z)]_\xi\xi_z + [\rho w\phi - \Gamma(\phi_\xi\xi_z + \phi_\eta\eta_z + \phi_\zeta\zeta_z)]_\eta\eta_z$$
$$+ [\rho w\phi - \Gamma(\phi_\xi\xi_z + \phi_\eta\eta_z + \phi_\zeta\zeta_z)]_\zeta\zeta_z = S \qquad (4.7)$$

Discretization of equation (4.7) is performed using finite difference method in the transformed domain by the method of SIMPLEC. For the diffusion terms the second-order central difference is used. For the convection terms, the hybrid difference scheme by Patankar (1980) is employed. In the hybrid scheme, central difference is used for cell Peclet number less than or equal to 2 and upwind difference is used when the cell Peclect number is larger than 2. The difference equation can be arranged to the following form by collecting terms according to the grid points around a control volume:

$$A_P\phi_P = A_E\phi_E + A_W\phi_W + A_N\phi_N + A_S\phi_S + A_T\phi_T + A_B\phi_B + S_1 \qquad (4.8)$$

where, $A_P = A_E + A_W + A_N + A_S + A_T + A_B + A_P^0 - S_P$, $A_P^0 = \rho_P^0 / \Delta t$

$$S_1 = S - S_P\phi_P + A_P^0\phi_P^0 + A_{NE}\phi_{NE} + A_{NW}\phi_{NW} + A_{NT}\phi_{NT} + A_{NB}\phi_{NB}$$
$$+ A_{SE}\phi_{SE} + A_{SW}\phi_{SW} + A_{ST}\phi_{ST} + A_{SB}\phi_{SB}$$
$$+ A_{ET}\phi_{ET} + A_{EB}\phi_{EB} + A_{WT}\phi_{WT} + A_{WB}\phi_{WB}$$

The superscript ^{0} denotes the solution at the previous time step. A fully implicit formulation is employed for solving the problems. The nonlinear equations of motion are

approximated by a system of linear algebraic equations of the form of equation (4.8). Detailed information about the grid staggering and solution procedures is given in Chen (1980).

4.2.3 Method of Three-Dimensional Grid Generation

The computational domain of the hybridization system with rotating blades is shown in Figure 4.1. The inlet and outlet pipes are simplified as straight pipes. To avoid the singularity at the axis where $r = 0$, the start position is set to $r = \delta$ and $\delta = 0.1mm$, which is termed as R_DLT(Figure 4.2) in the grid generation code. In addition, to avoid the complexity of the grid generation, the geometry of the cross-section of the outlet pipe is changed to rectangular with same area of cross-section.

The grid generation of the hybridization system is divided into two steps. First step is to generate the two-dimensional grid of the meridian section; second step is to generate the three-dimensional grid based on the meridian grid.

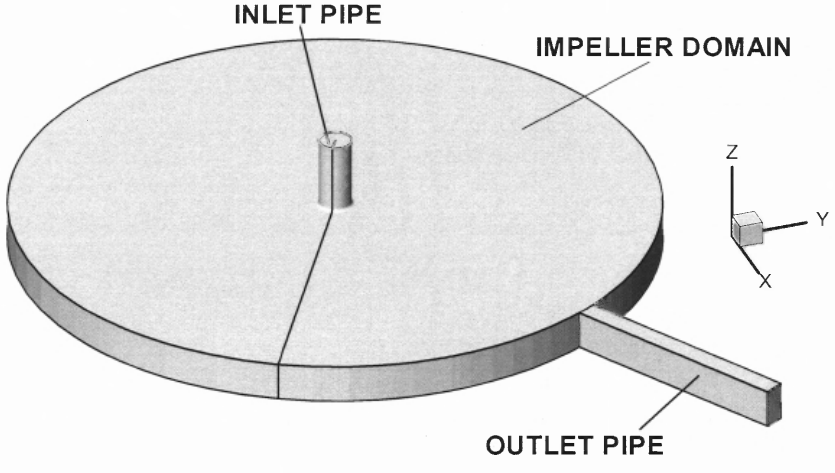

Figure 4.1 Three-dimensional Computation domain of the hybridization system.

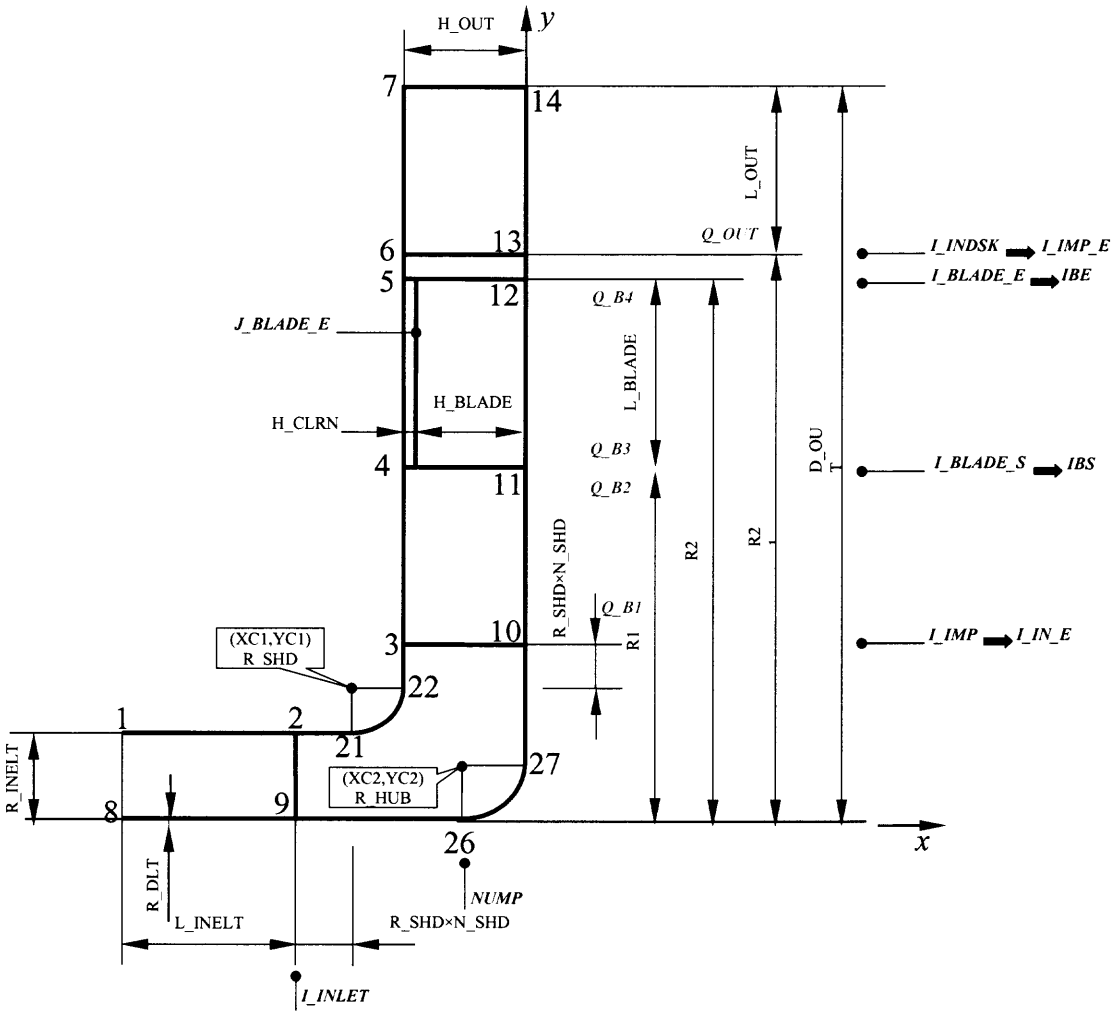

Figure 4.2 Schematic of the meridian domain of the hybridization system.

4.2.4 Flow Field Analysis

The numerical code is run for different rotational speeds ranging from 5000 to 15000 rpm. The results of airflow field are presented in Figures 4.3-4.6 for the rotational speeds of 5000, 8000, 10000 and 15000 rpm, respectively. As seen from these velocity contours, there are certain regions where the velocity field of air is very high as compared to other areas. Near the outer wall and between the blades, the velocity is maximum in all the

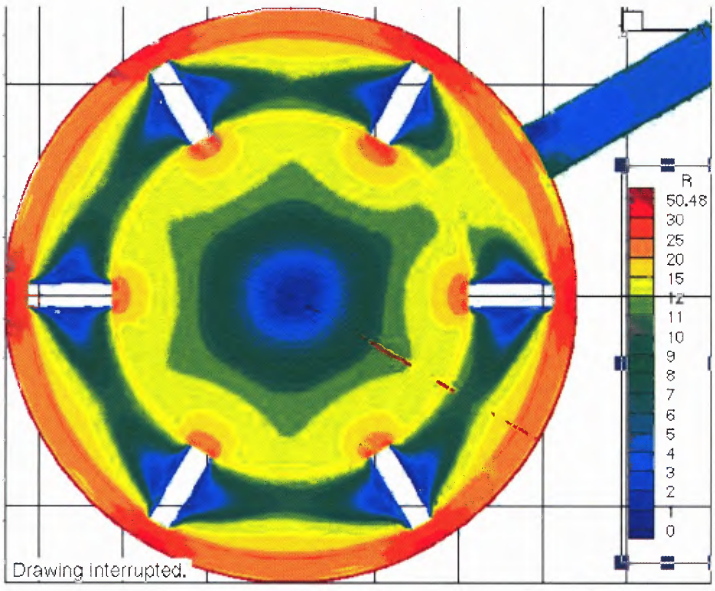

Figure 4.3 Airflow field inside the mixing chamber of the hybridization system at 5000 rpm.

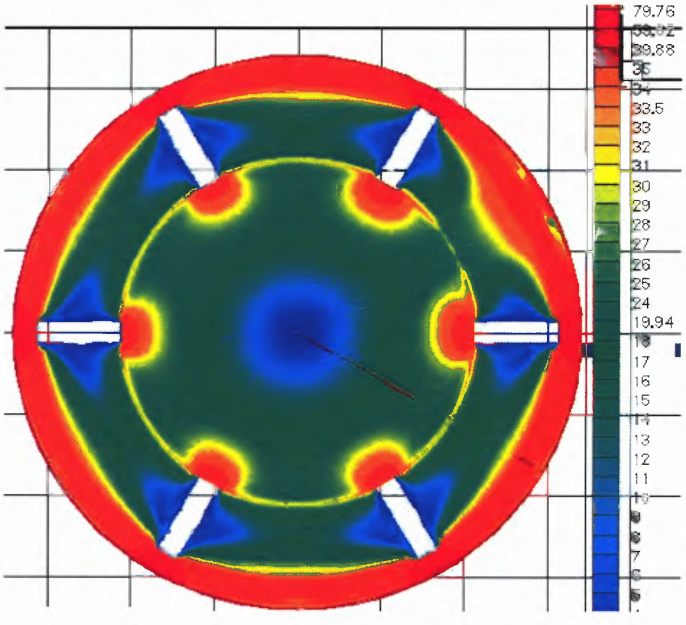

Figure 4.4 Airflow field inside the mixing chamber of the hybridization system at 8000 rpm.

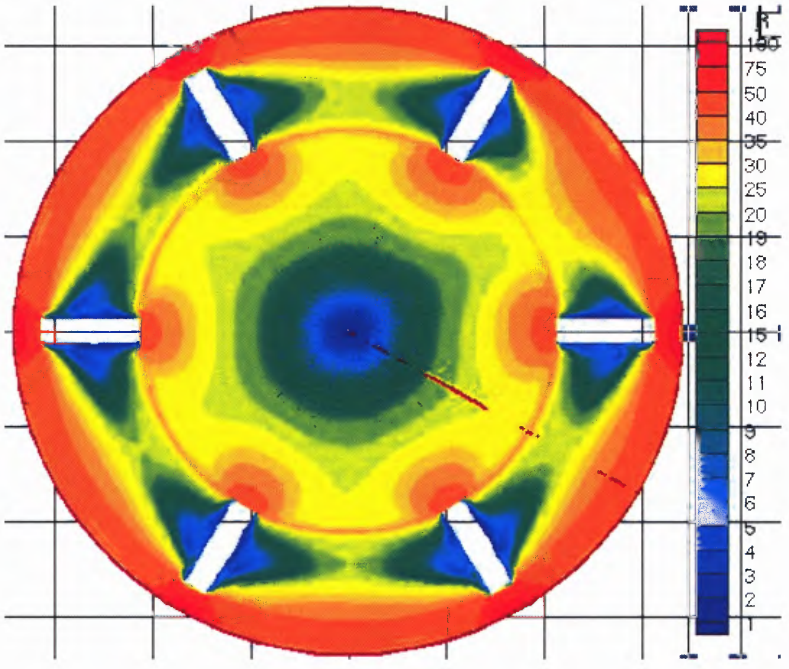

Figure 4.5 Airflow field inside the mixing chamber of the hybridization system at 10000 rpm.

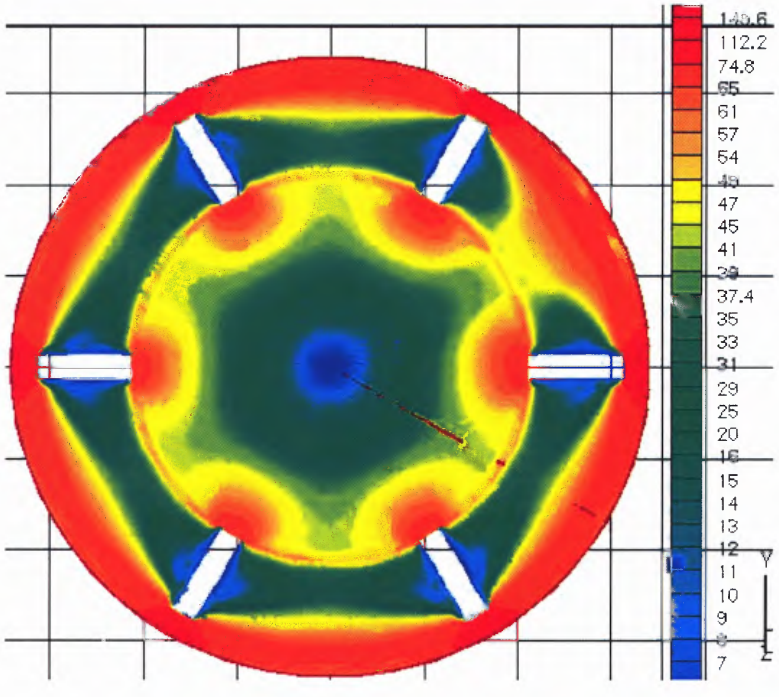

Figure 4.6 Airflow field inside the mixing chamber of the hybridization system at 15000 rpm.

cases and increases linearly with the rotational speed. Maximum velocities attained by the airflow are approximately equal to 50, 75, 100 and 150 m/s, respectively. Velocity of air is minimum at the center of the mixing chamber and increases towards the outer wall. Thus, it can be concluded that the general pattern of air flow remains the same for all the rotational speeds, however, the magnitude of velocities goes on increasing linearly. Also, as shown in Figure 4.3, the airflow field near the re-circulation pipe is in the range of about 10 m/s. Due to the sudden expansion/opening, there is a drop in the velocity of the flow field and formation of vortices takes place. Due to high velocities and the air drag near the outer wall, it can be estimated that the particles settled down between the gap of blade and the mixing chamber can be lifted and revolved in the mixing chamber as well as re-circulated in the re-circulation pipe increasing the efficiency of the coating process.

4.3 Flow Field Analysis Using Fluent

Commercial software FLUENT 5.5 is used for the gas/particle flow system to predict particle and gas flow patterns in the Hybridization system. The $\kappa - \varepsilon$ turbulence model is used to understand the turbulence behavior of the gas phase. The algebraic slip mixture (ASM) model was employed as the multiphase model in the computation. (This will be discussed in chapter 5). The velocity and pressure profiles for the gas phase are analyzed. The result from Fluent is then compared to the results obtained using a numerical code discussed in the earlier section.

4.3.1 Simulation Parameters

Simulations were carried out for different rotational speeds as done in the earlier section of this chapter. Gas properties were set to equal those of air. The system geometry is shown in Figures 4.7 and 4.8. The mixing chamber geometry is shown in Figure 4.7 and the re-circulation tube is shown in Figure 4.8. Approximately 278,000 tetrahedral meshes are used in the simulation.

4.3.2 Velocity and Pressure Contours (Fluent)

Numerical simulations were performed for the different rotational speeds as done in the earlier section. The results are shown in Appendix A.

Figure 4.7 System Geometry.

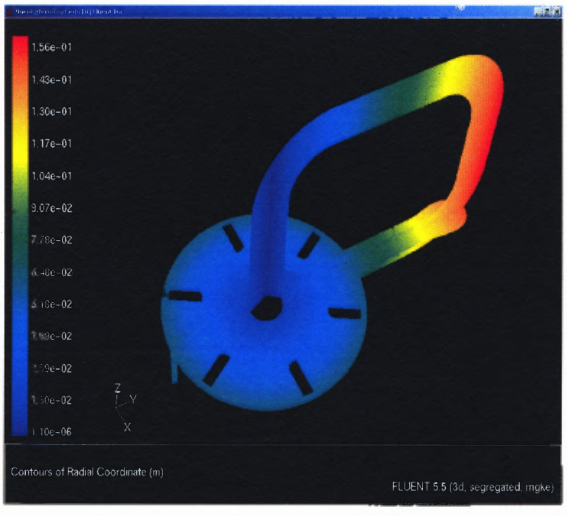

Figure 4.8 System Scale and Two Cross Sections.

In the mixing chamber of the hybridization system, when the blades are rotating, high pressure begins to build up near the cylindrical chamber side wall, and then drives the air flow out through the outlet on the chamber side wall and re-circulates back to the upper center part of chamber via the re-circulation pipe. From Figures shown in Appendix A, it can be seen that higher velocity region is located near the sidewall of the chamber and the maximum value appears around the outlet from the chamber to the re-circulation pipe.

The flow field in the re-circulation pipe at 5000 rpm is fairly uniform throughout the pipe except at the exit point, where high velocities are observed. Velocity of the flow field is in the range of 5 to 15 m/s. The flow field computed by Fluent can be broadly classified into three regions inside the mixing chamber. One near the inner cylinder (point of entry), second between the blades and the central part of the mixing chamber and third around the blades. The velocity of the flow field is higher in the third region, and gradually decreases as we move towards the center of the mixing chamber.

The pressure distribution contours inside the mixing chamber of the hybridization system is shown in Figure 4.9.

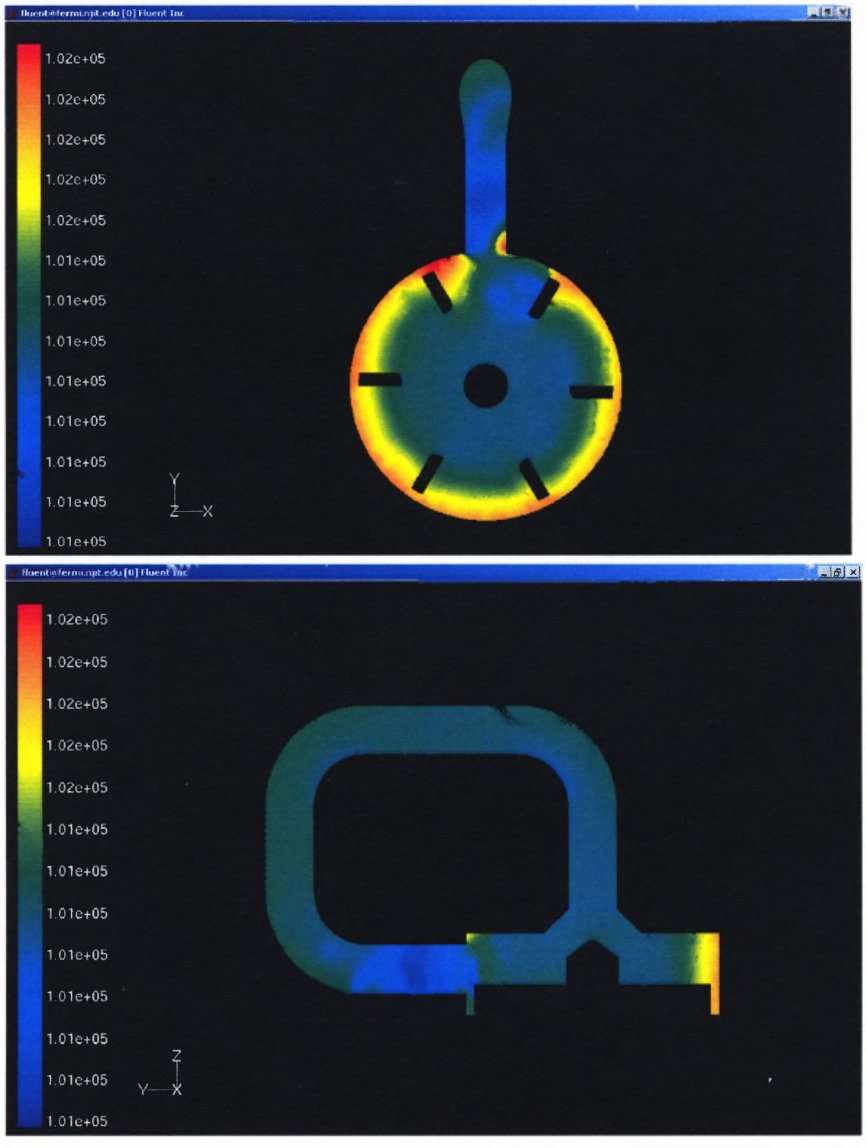

Figure 4.9 Pressure distribution inside the mixing chamber and the re-circulation tube at 5000 rpm.

It is clear from Figure 4.14 that pressure is built up on the outer wall. Pressure drop is observed at the exit of the re-circulation tube. Again, the pressure distribution inside the re-circulation tube remains fairly uniform.

The differences between these two computational codes are seen from the contours of the flow field; however, the magnitude of the velocities remains almost

identical. Figure 4.10 illustrates the comparison of velocity vectors at the exit of the re-circulating pipe. The direction of velocity vectors is identical in both cases. There is a formation of vortices and a back flow is seen in that region.

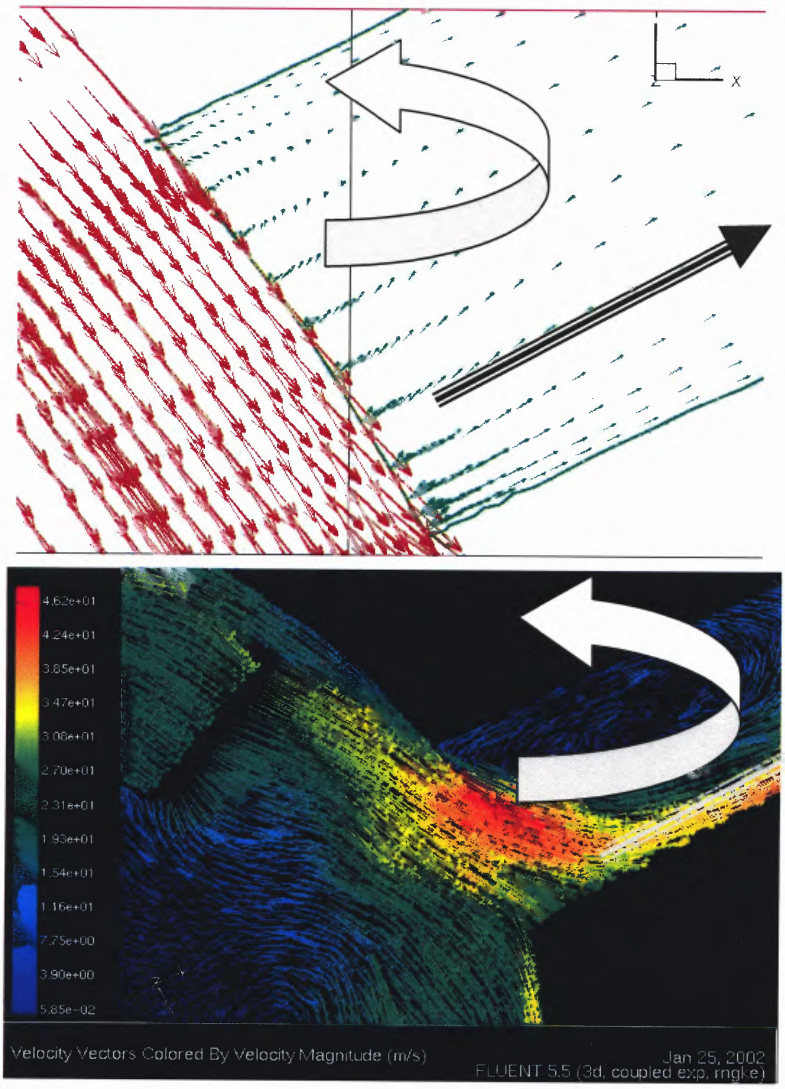

Figure 4.10 Comparison of velocity vectors near the exit of re-circulating tube using computational fluid code and Fluent.

4.4 Experimental comparison

In order to validate the simulation results computed by two aforementioned numerical codes, air velocities inside the mixing chamber and the re-circulating pipe were measured and compared with the simulation values. The experimental values were measured using a pitort tube. The results are shown in Figures 4.11 and 4.12.

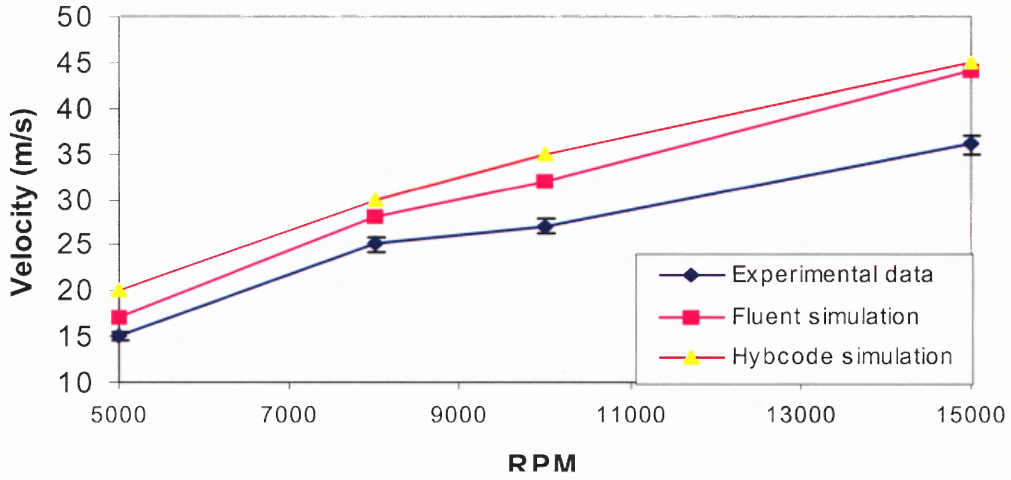

Figure 4.11 Comparison of velocities in the re-circulating pipe.

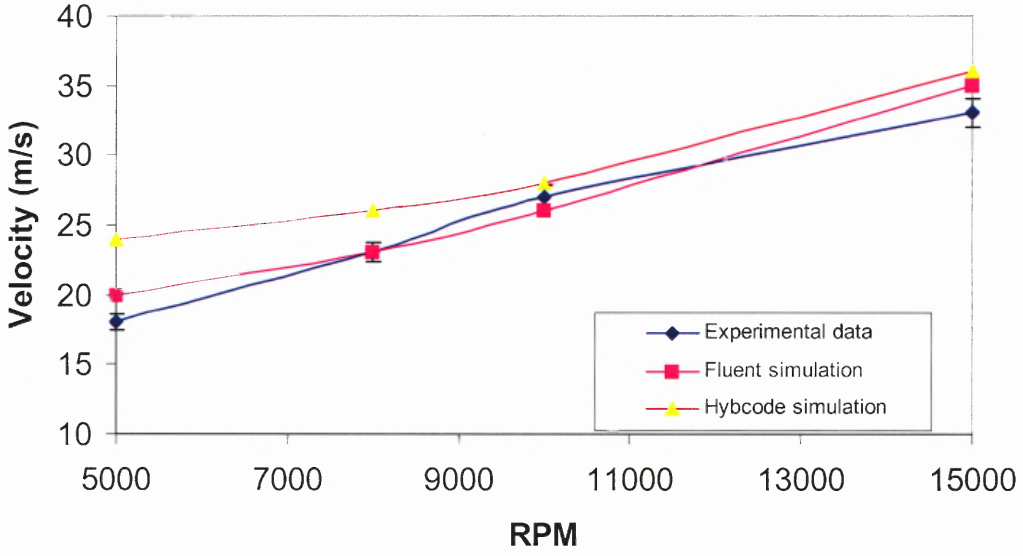

Figure 4.12 Comparison of velocities near the center of the mixing chamber.

As seen, the velocities measured experimentally closely resembles to the numerically simulated values. The velocities were measured for different rotational speeds and in each case, the computed as well as experimentally measured velocities were found to be very close and comparable.

4.5 Conclusions

Numerical simulation of hybridization system from CFD point of view is carried out and the results are presented in this chapter. The induced air draft due to the high-speed rotation of the blades, which, is very crucial in the effective and efficient operation of the hybridization system, is analyzed using two different numerical codes and their results are compared. These numerical codes employs k-ε model. Velocity contours demonstrate the effect of the airflow field inside the mixing chamber as well as the re-circulating pipe of the hybridization system. Higher velocities are seen near the outer wall and along the blades. Velocities are low near the entry of the re-circulating pipe. Due to the sudden expansion at the exit of the re-circulating pipe, the pressure drop is observed and the vortices are formed. The air velocity is very high near that region. Also, the air velocities increase linearly with the increase in the rotational speed of the mixing chamber. The flow pattern is not nearly identical in these two computational codes; however, the magnitude of the quantities computed is identical. Overall flow inside the system seems to be symmetrical about the axis of revolution except in the region near the exit of the re-circulating pipe. Pressure distribution is also computed and found to be higher near the outer wall of the mixing chamber. The quantities such as velocity, and pressure are uniform throughout the re-circulating pipe. Simulated values of the air velocities are

compared with the experimentally measured values and a good agreement between the values is seen.

After studying these two different methods of numerical simulations, DEM in Chapter 3 and CFD in Chapter 4, the task remains to study both these effects combined. Next chapter therefore is focused on the studies of DEM and CFD combined, as well as using a multi-phase model in Fluent to study both gas and particle phases together.

CHAPTER 5

COUPLING OF PARTICLES-AIR FLOW USING NUMERICAL TECHNIQUES

The importance of airflow field on the performance of the hybridization system is vital. Numerical simulation of the hybridization system using Discrete Element Method (DEM) is carried out in Chapter 3, where the particles are simulated and treated as discrete elements. Effect of air drag on the particles was not considered. Also, with the aid of computational fluid dynamics techniques (CFD), the airflow inside the mixing chamber as well as within the re-circulating pipe is computed in Chapter 4, where the effect of particles was not taken into account. Hence, the inclusion of air drag effect on the particles is dealt in this chapter with the coupling of DEM and CFD to further evaluate the performance of the hybridization system. In addition, the modeling is carried out using a multi-phase model (CFD). In DEM and CFD coupling, various quantities such as, number of collisions, work done due to collision, the type and magnitude of forces are calculated. The distribution of particles inside the system is also evaluated. Effects of different operating parameters such as loading of particles, rotational speeds are studied. In the first part of this chapter, DEM results of the smaller size of the hybridization system are presented to understand the effect of air drag on the particles and are compared with the quantities diagnosed in chapter 3. Remaining part of this chapter is devoted to the preliminary DEM simulation of the particles in the re-circulating tube as well as the DEM simulation of the full size hybridization system. The scaling problem of the hybridization system is also investigated and various quantities such as velocity, pressure, and turbulent intensity of the scaled sizes are compared with the original size.

5.1 Introduction

Coupling of gaseous phase with the solid phase has been studied by number of researchers in the past. Different techniques and the complexity of the problem under investigation determine the approach of performing the coupling studies. Coupling studies have been concentrated in the area of fluidized beds. Y. Tsuji et al. (1998) performed the numerical studies of two-dimensional fluidized beds using discrete element method to calculate the motion of particles by solving Newton's laws of motion. Locally averaged equations derived by Anderson and Jackson (1956) were solved to calculate the fluid motion taking into account the interaction of fluid and particles. Effect of drag force on the particles and the particle-fluid interaction force was used to modify the equation of motion in both the-fluid model as well as the DEM model to solve these equations simultaneously. Similar approach is used by Horio et al. (1998) to simulate the behavior of cohesive powder in the fluidized bed. Yue et al. (2000) recently performed the numerical studies of air-particle motions in bubbling fluidized bed of smaller particles. Particle-particle interactions were solved using Discrete Element Method. The Navier-Stokes equations and the Lagrangian type particle equations were simultaneously solved where the drag and lift forces on the particles, multi-body collisions among particles and mutual interaction between particles and air were taken into account.

All these coupling studies were done using a strong two-way coupling approach, which solves the DEM code as well as the fluid code simultaneously. However, due to the computational limitations and the complexity of the problem in the present study for the coupling of DEM with the fluid model, a two-way weak coupling is employed, which is discussed in the following section.

5.2 Coupling Using DEM

5.2.1 Simulation Scheme

Behavior of airflow field inside the mixing chamber of the hybridization system has already been explained in details in chapter 4. The airflow field has a symmetrical pattern. A sector as shown in Figure 5.1 between the two blades is considered. The time dependant air velocity at every node between this region is computed using Fluent.

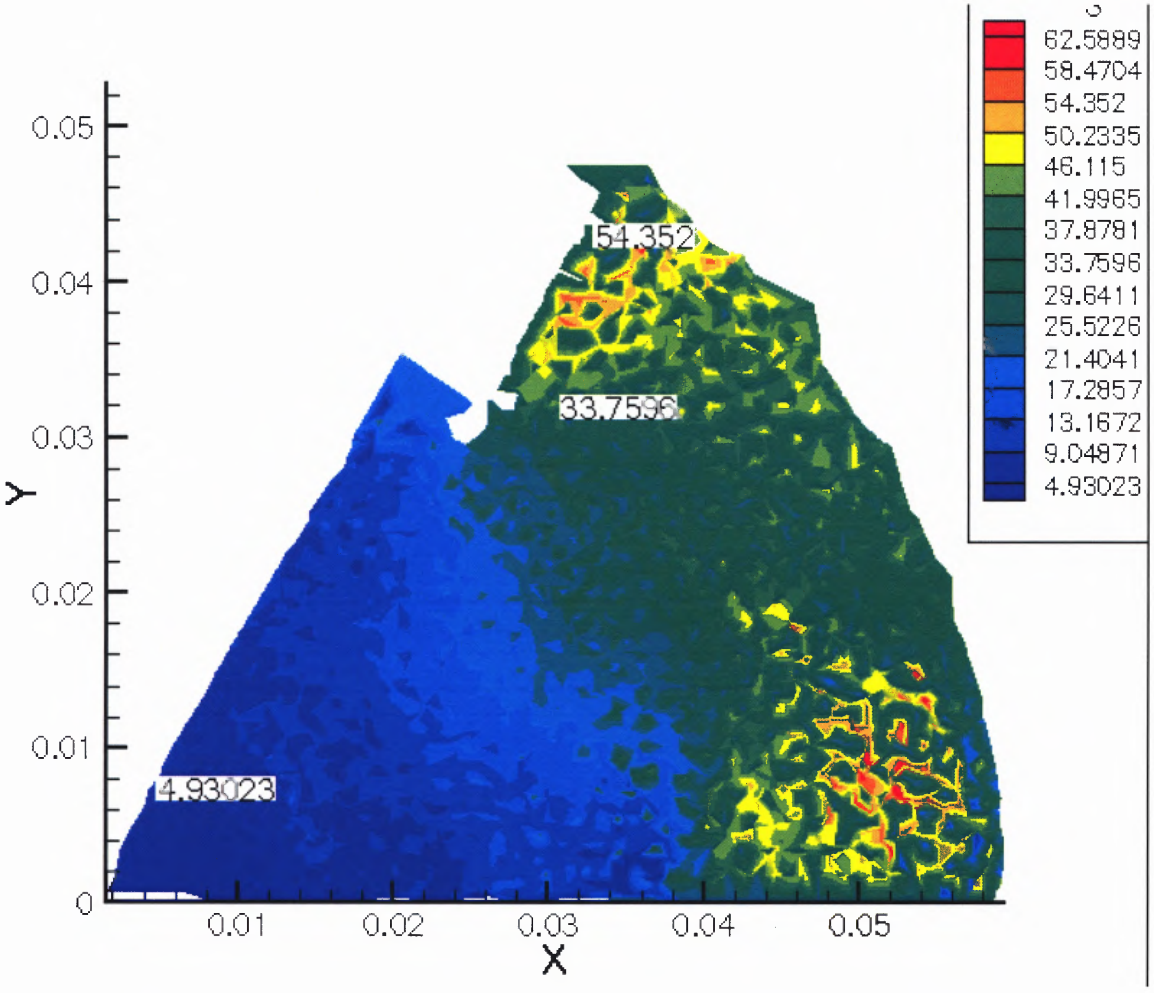

Figure 5.1 Sectorial section considered for the calculation of drag force.

In DEM numerical code, the region between the two blades is divided into number of areas as shown in Figure 5.2.

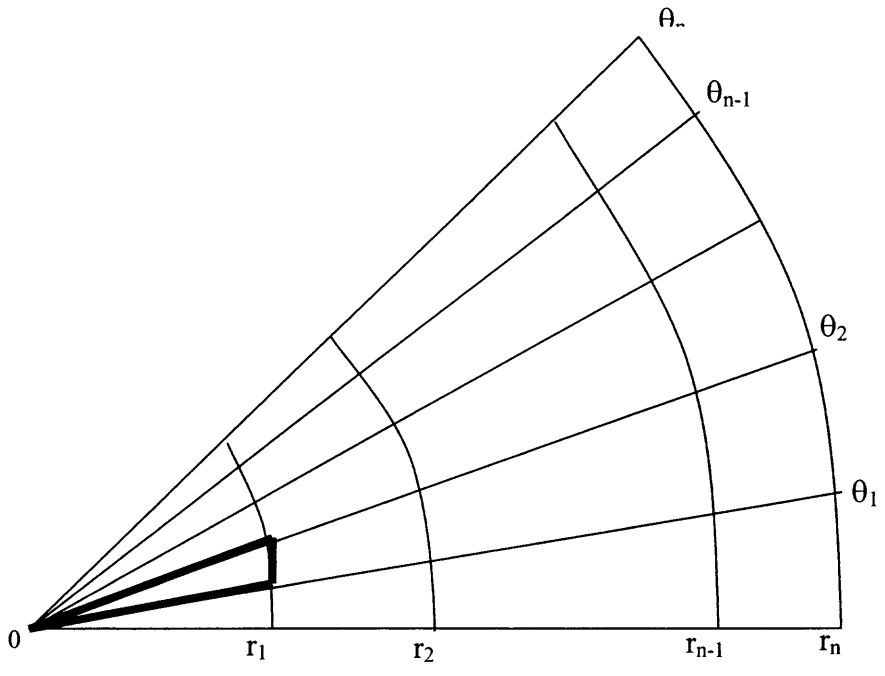

Figure 5.2 Designated regions in DEM code.

During the simulation, the particles falling into these regions, (for example the region highlighted in above figure) finds the nearest node in that region and the air velocity is assigned to that particle for the consideration of the drag force. This is true for every particle in the region falling between these two blades as well as in the regions formed similar to this in the other blades as well. In the next time instant, the particles are assigned new positions and velocities, thus they may fall under different regions. The same flow field is mapped according to the new position of particles and the new node, which is closer to the particle influences the drag associated with it. This process is continued till the end of the simulation.

The air drag force is calculated using following equation.

$$\vec{F}_D = \frac{1}{2} C_D \rho_g A_s \mid \vec{U}_a - \vec{U}_p \mid (\vec{U}_a - \vec{U}_p)$$

$$R_{e_p} = \frac{\rho_g \mid \vec{U}_a - \vec{U}_p \mid}{\mu_g} \tag{5.1}$$

where F_D is the drag force; C_D is the coefficient of drag which is calculated on the basis of Reynolds number.

$C_D = 24 / Re;$ $\quad Re < 2$

$C_D = 18.5 / Re^{0.6};$ $\quad 2 < Re < 500$

else, $C_D = 0.4$

ρ_g is the gas density; As is he surface area of the particle; U_a and U_p are the air and particle velocities in that time instant.

Simulations were run for different rotational speeds as well as different loading conditions and the quantities such as the particle-particle, particle-boundary collisions, average tangential and normal forces were computed. The results are presented below.

5.2.2 Collisions Analyses

Particle-particle as well as particle-boundary interactions inside the mixing chamber of the hybridization system were carried out including the air drag force. The results for particle-particle interactions are shown from Figures 5.3-5.6. Particle-boundary interactions are illustrated from Figures 5.7-5.10.

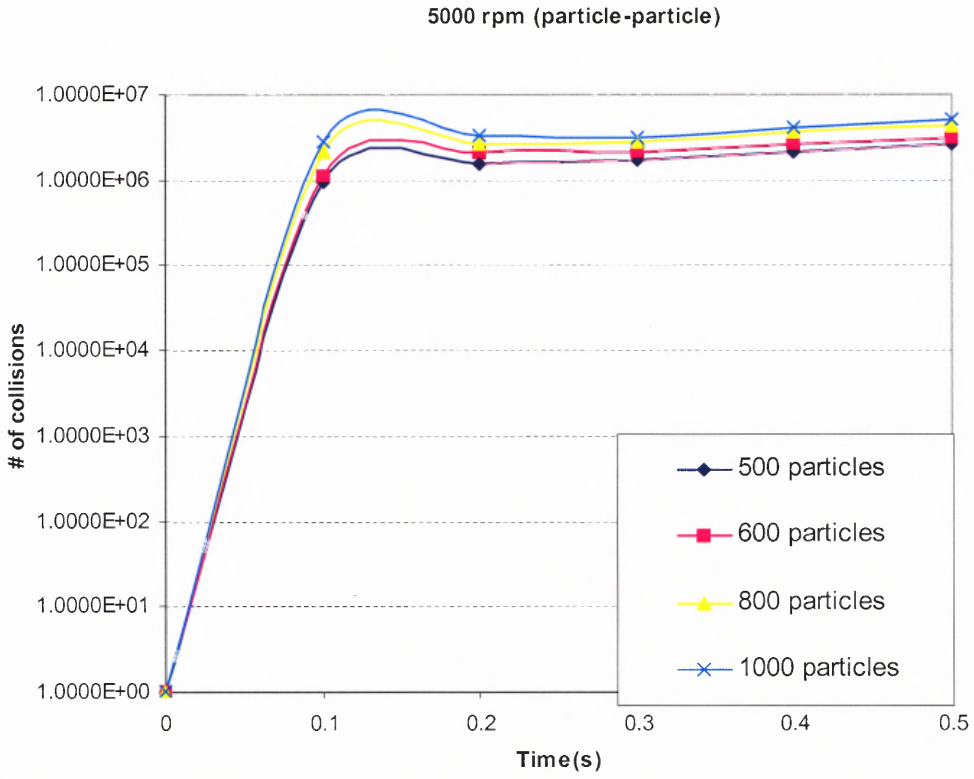

Figure 5.3 Particle-particle interactions for 5000 rpm.

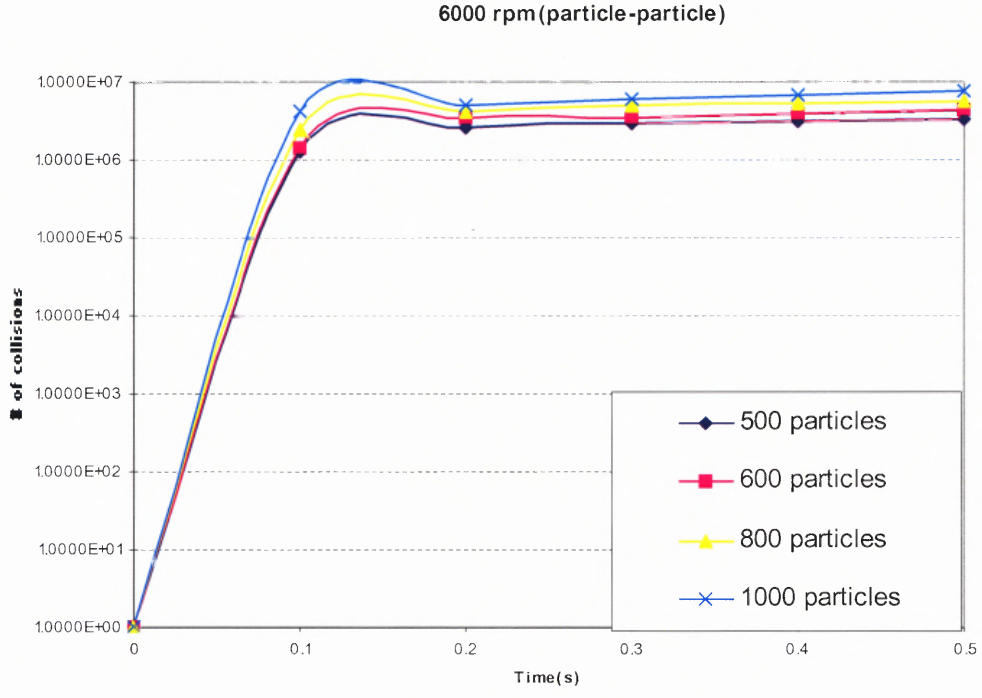

Figure 5.4 Particle-particle interactions for 6000 rpm.

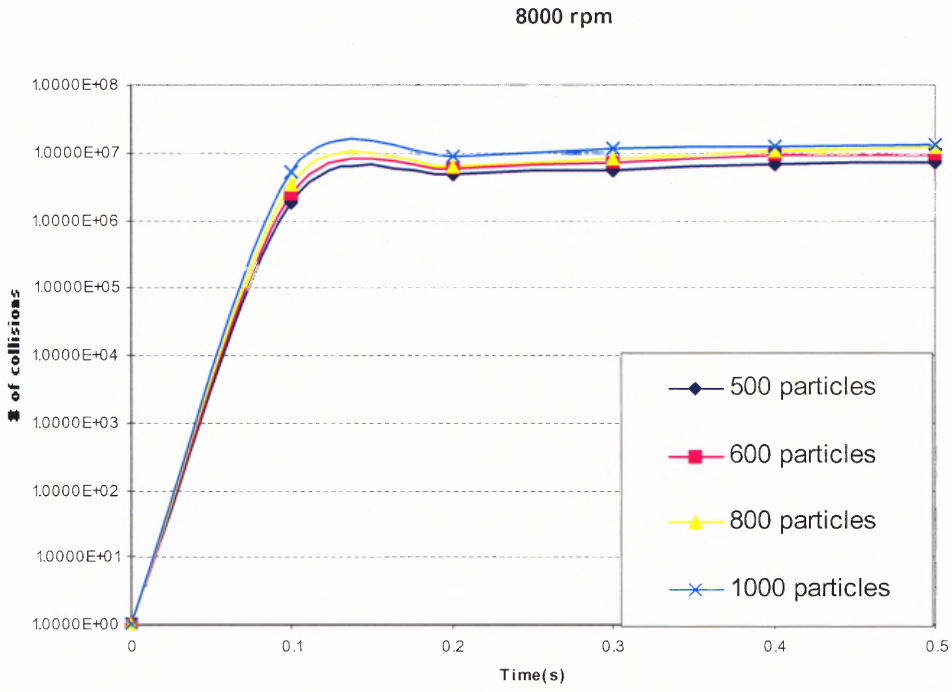

Figure 5.5 Particle-particle interactions for 8000 rpm.

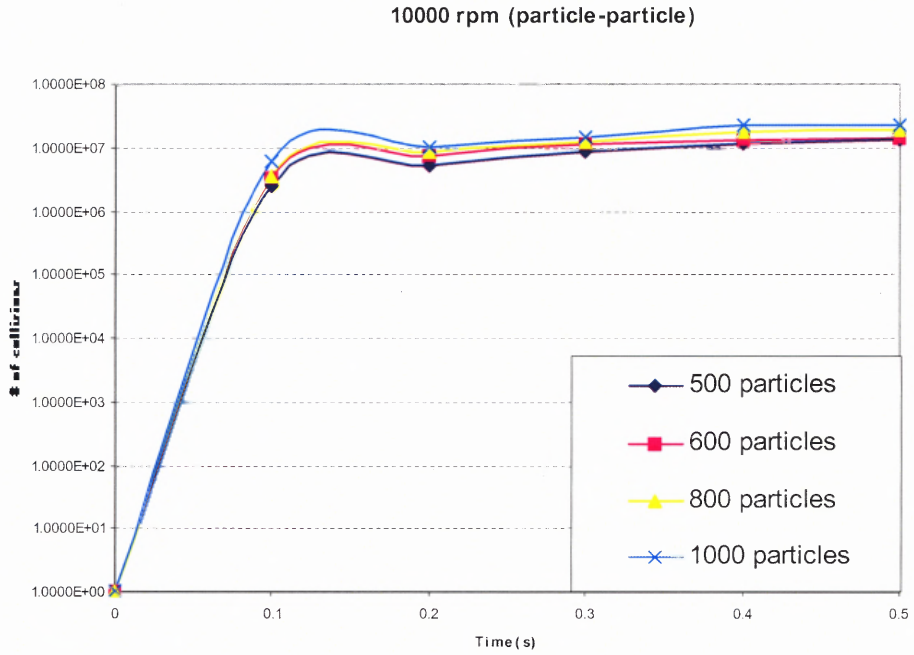

Figure 5.6 Particle-particle interactions for 10000 rpm.

The particle-particle collisions, as seen earlier in the case of absence of air drag (discussed in chapter 3) increases with time. Up to 0.2 seconds of simulation time, the rise in the collisions is not distinct for different loadings, however, after 0.2 seconds, number of collisions seem to be rising linearly with time. The number of collisions per particle is in the order of 10^7.

Particle-boundary collisions on the other hand present a different scenario. The number of collisions is less as compared to the case of absence of air drag. The rise in the collisions is linear unlike the particle-particle collisions. Also, different loading conditions and different rotational speeds do not seem to make much difference in the collisions of particles with the boundary.

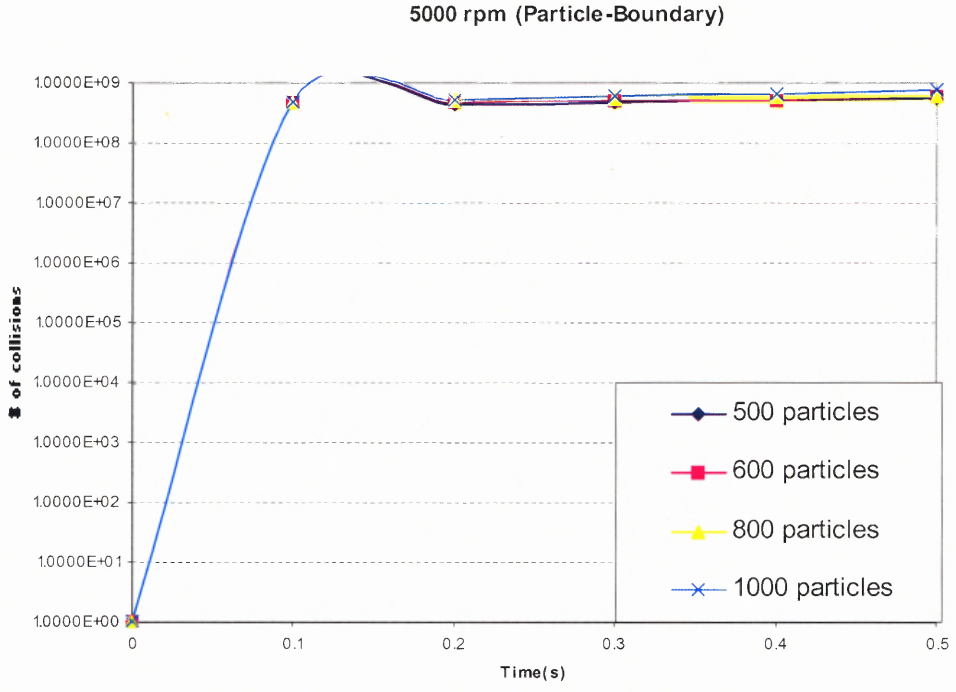

Figure 5.7 Particle-boundary interactions for 5000 rpm.

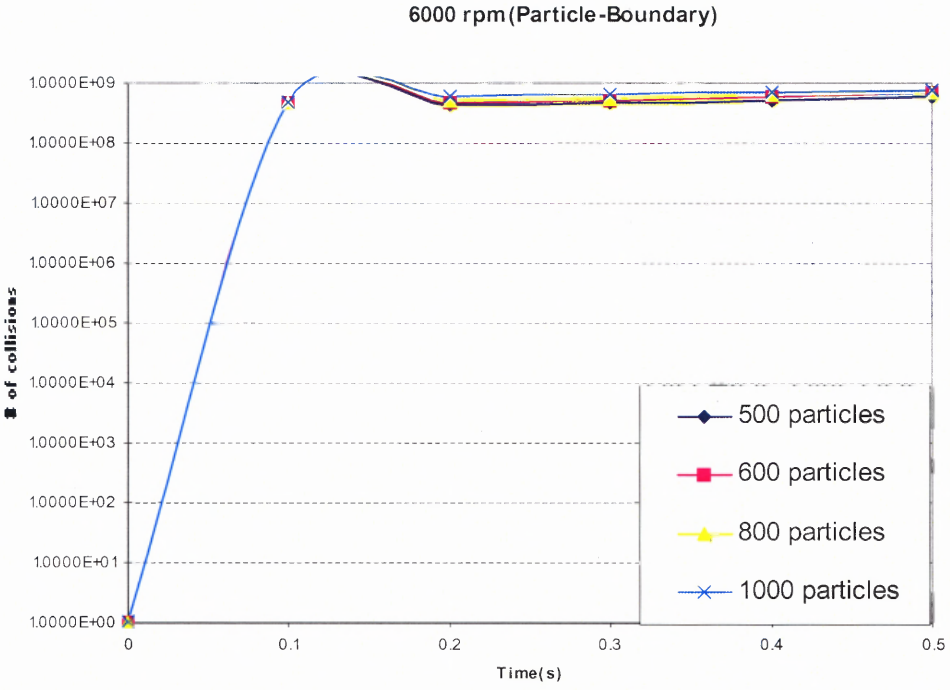

Figure 5.8 Particle-boundary interactions for 6000 rpm.

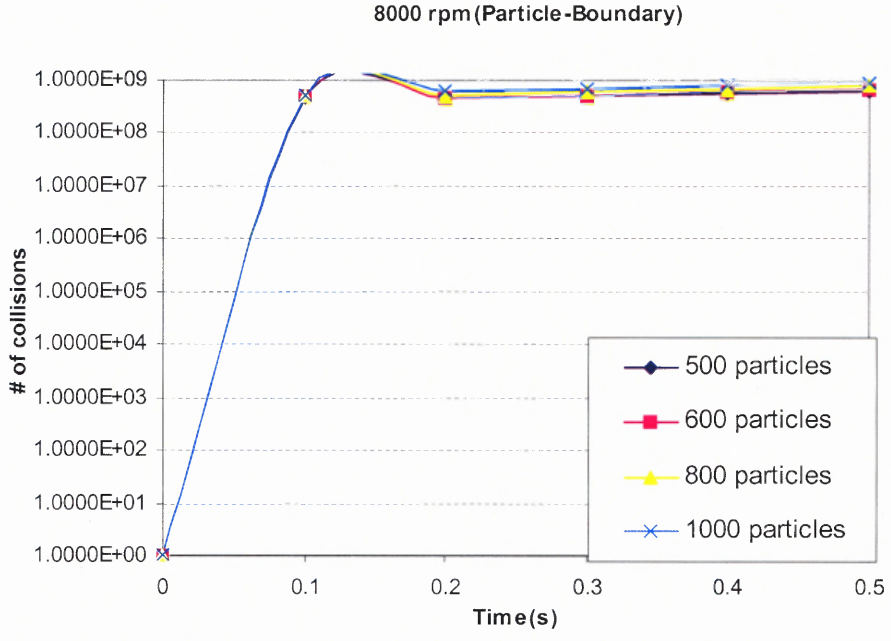

Figure 5.9 Particle-particle interactions for 8000 rpm.

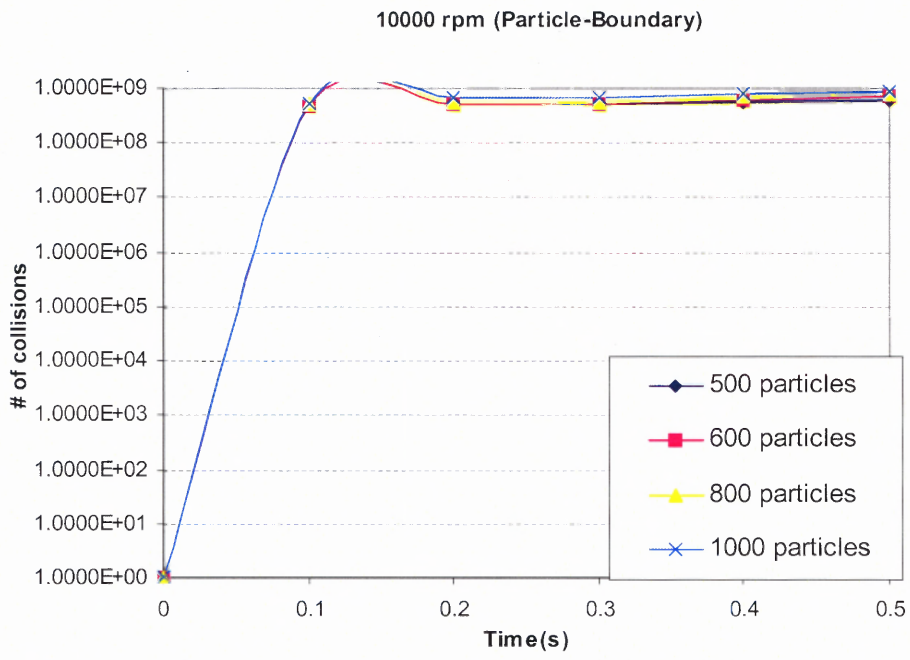

Figure 5.10 Particle-boundary interactions for 10000 rpm.

5.2.3 Forces

Computations of forces inside the mixing chamber of the Hybridization system were carried out in order to understand the impact of particles on one another. Tangential forces and normal forces were computed for the different loadings and the rotational speeds. These forces are the long-term average values and are obtained by all the instant values during the simulation. As seen (Figure 5.11) in the absence of air drag effect on the particles, tangential forces were seen to be in the range of 10^{-3}N. Forces were higher for the higher loading cases. Up to 8000 rpm, the forces for the loading cases of 500, 600 and 800 particles were seen to be in the similar range, these however increased from 8000 to 10000 rpm. At 10000 rpm and 1000 particles loading case, the tangential forces were particularly seen to be very high as compared to other loading cases. In the presence of

air drag, the magnitude of the forces was higher by the order of magnitude. The general trend with the increasing loading was seen to be the same as compared to the absence of air drag case.

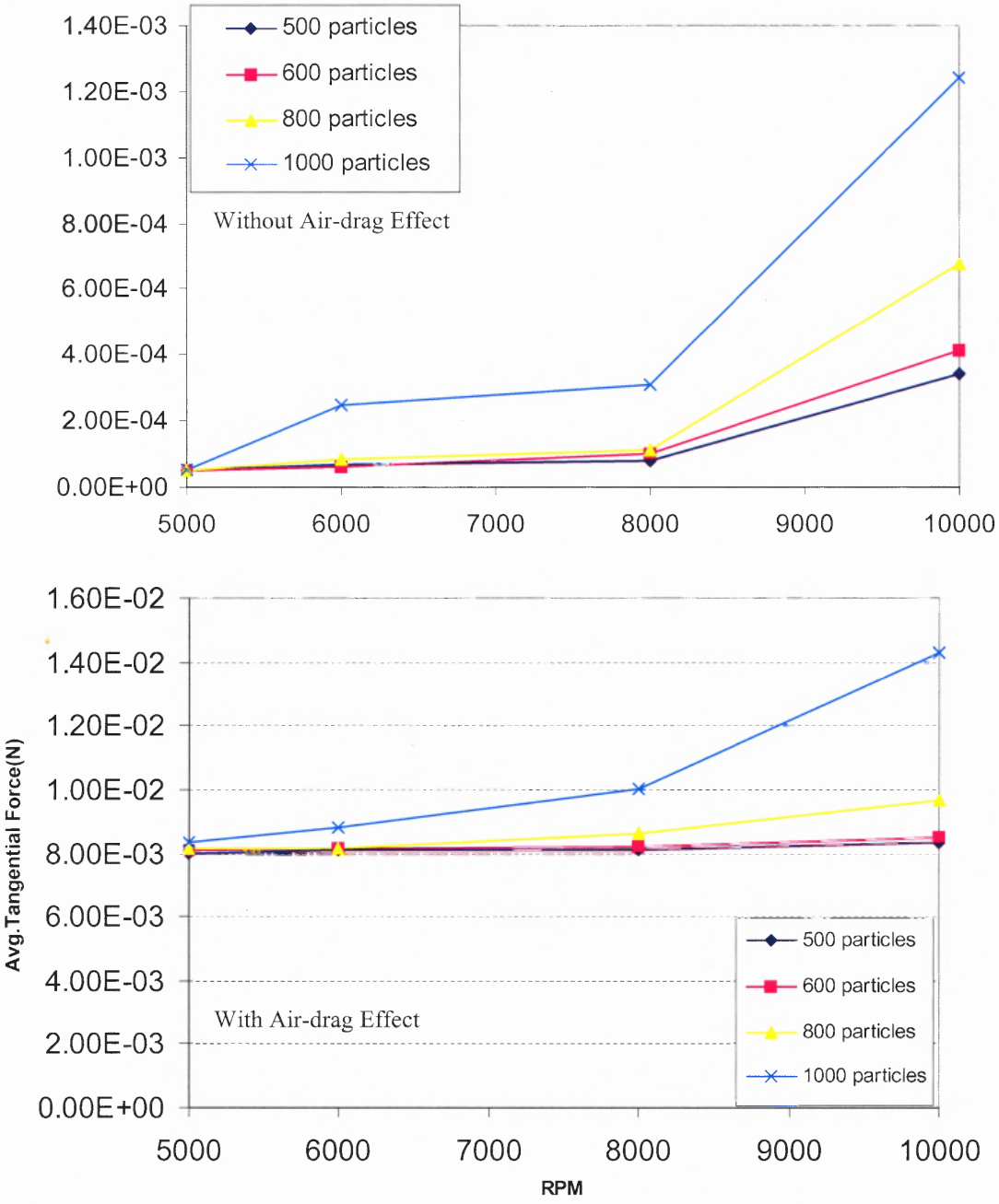

Figure 5.11 Average Tangential forces.

On the other hand, in the case of normal forces (Figure 5.12), there was not much significant change observed as the loadings and rotational speeds changed, which means the tangential forces had an important role in the operation of the system. However, the normal force was seen to be much higher than the tangential forces, which was in the range of 10^{-2}.

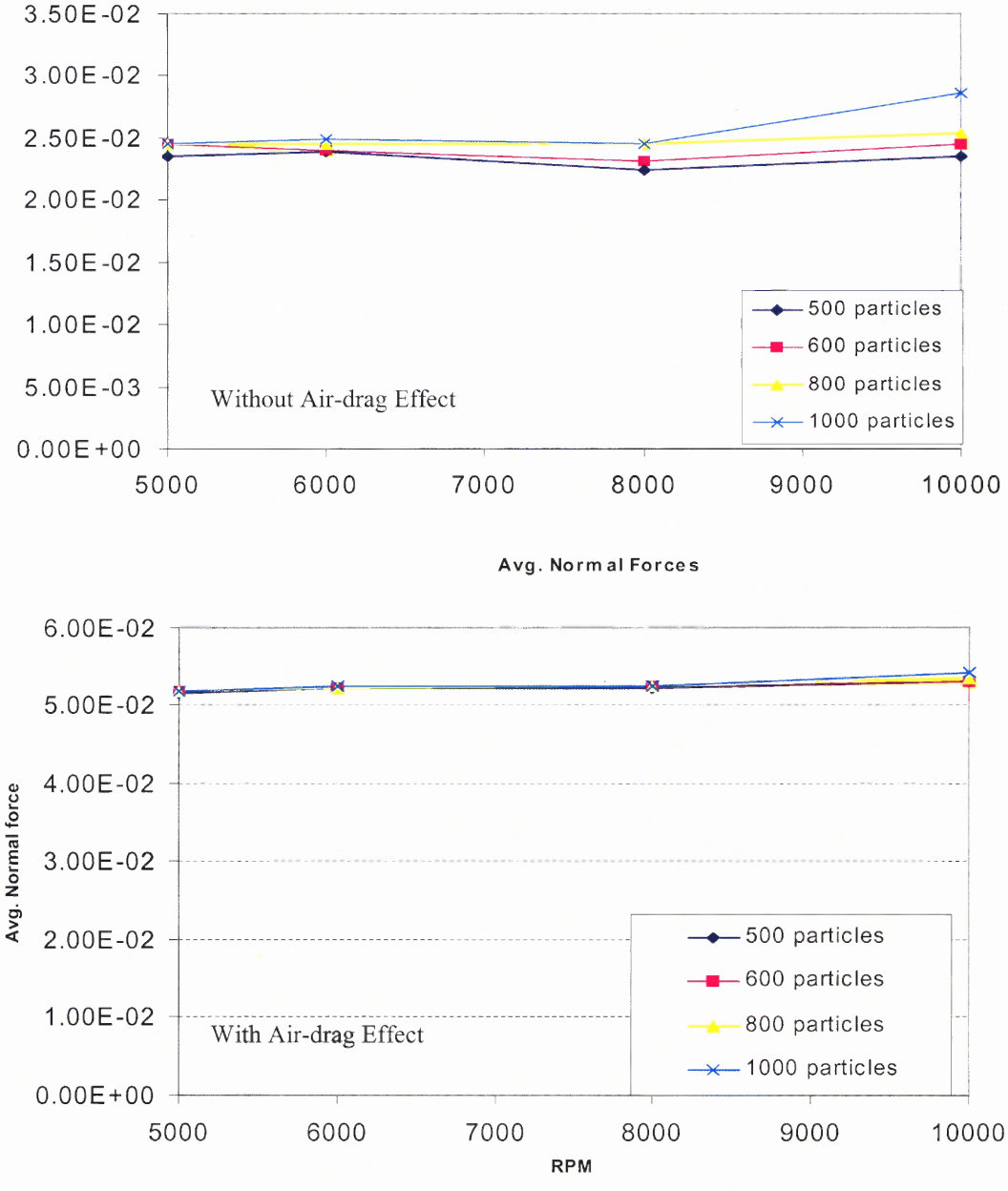

Figure 5.12 Average Normal forces.

The strength of normal forces was seen to be even higher when the particles experienced the air drag due to the fluid force. As seen in Figure 5.12, increase in the loading does increase the normal force experienced by the particles, but not by a comparable margin.

5.2.4 Number Density Distribution

In order to see the distribution of the particles inside the mixing chamber with the effect of air drag, the number density of particles were computed in three different zones. The zones were divided into three concentric circular regions in such a way that the zones neat the blades is designated as 'Blade', the middle part of the chamber is designated as 'Middle' and the zone near to the inner cylinder is termed as 'Inner'. It is illustrated in the following Figure 5.13.

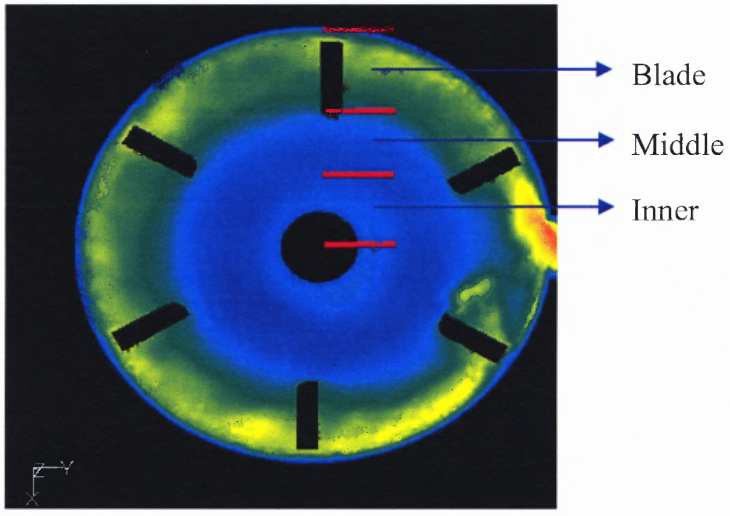

Figure 5.13 Three regions of the mixing chamber for evaluating the number density.

As shown, three regions are separated on the basis of velocity profiles obtained from Fluent. Simulations were run for the rotational speeds of 5000 and 10000 for loading of particles of 600, 800 and 1000. The results for 5000 rpm are presented below.

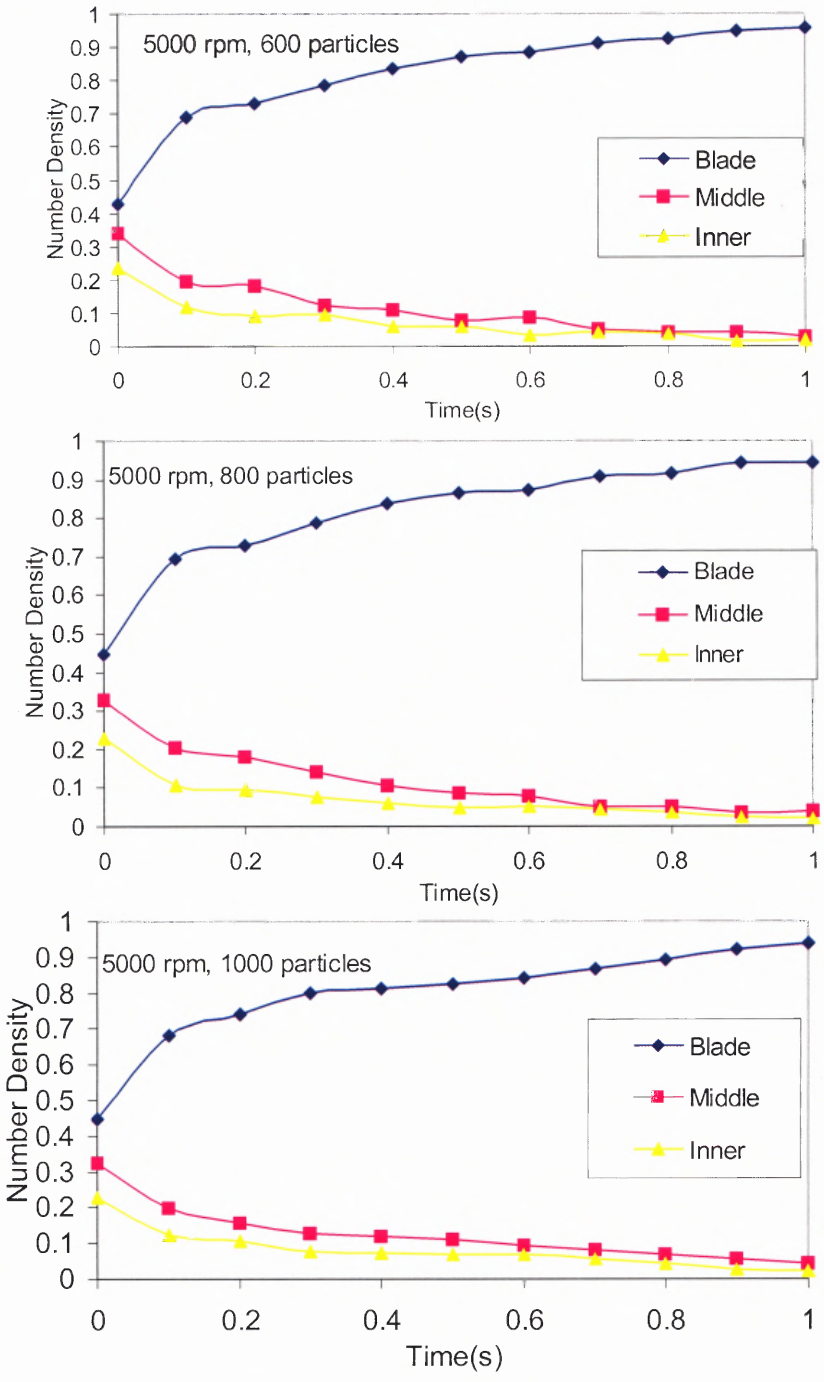

Figure 5.14 Number density plots for 5000 rpm.

As the simulation started, the particles start colliding with each other as well as with the walls of the mixing chamber including blades. From the Figure 5.14, it is clear that the particles due to the effect of air drag and due to the centrifugal force are positioned to the outer part of the chamber i.e. near the blades region. 90 % of the particles are seen to be following the motion of the blades, while remaining 10 % particles are seem to be distributed evenly between the middle and the inner part of the mixing chamber. Same results are obtained for the case of 10000 rpm, which means that the effect of loading of particles as well as the rotational speed of the mixing chamber has a very little effect on the distribution of the particles, and the particles are driven by the air drag force. Therefore, it can be concluded that the important region in the mixing chamber is the one near the blades, which may decide the coating quality of the particles.

5.2.5 Coating Time

Coating time calculations are done based upon the minimum time required for the particles to cover the complete surface area of all the host particles. It can be estimated in the following way.

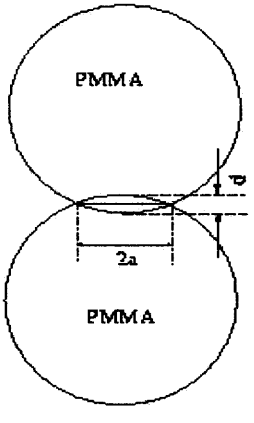

Figure 5.15 Coating Time Calculation.

- Calculate maximum central displacement d for each host-host contact
- Calculate the contact radius a of this contact by equation $a = \sqrt{d * R}$
- Calculate the summation of contact area until it equals to the total surface area of the system, which is equal to N*S, where N is the total number of host particles and S is the surface area of each host particle.

For the rotational speed of 5000 rpm, and the loading of particles: 500, the total coating time required is found out to be equal to 0.23 seconds. This time is should be much less than the actual experimental measurements, since it is assumed here that each contact occurs on different position of particle surface. There this coating time is the only estimation and not the exact value.

5.2.6 DEM of Re-circulating Pipe

Numerical simulation of re-circulating pipe is also initiated and the preliminary results are presented in this section. As shown in Figure 5.16 velocity contour of cross section taken in the pipe is illustrated. The velocities are in the range of 1-17 m/s.

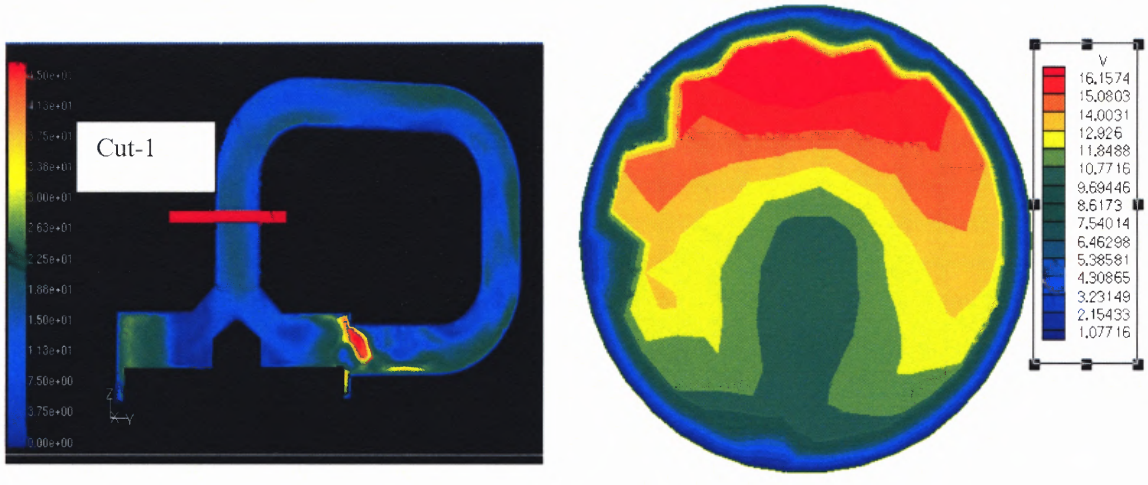

Figure 5.16 Velocity field (5000 rpm) inside the re-circulating tube at the section cut-1.

This velocity field is used to assign the air drag to the particles in DEM modeling. DEM simulation is run for the set of 100, 200, 300, and 400 particles. Initially, the particles are arranged randomly and the velocity field is assigned to the particles with the help of the velocity field taken from fluent. In order to take the bends in the recirculating pipe into account, an equivalent length of the pipe is estimated and the simulations are run for the velocity field at 5000 rpm. The snapshots from the DEM results at 0, 0.5 and 1 seconds of simulation are shown in Figure 5.17. As seen, the particles initially starts moving with the flow field and at the end of simulation are cornered inside the pipe. In order to get an estimate of the number and types of collisions, the particle-particle as well as the particle-boundary interactins is also computed and the results are shown in Figure 5.18.

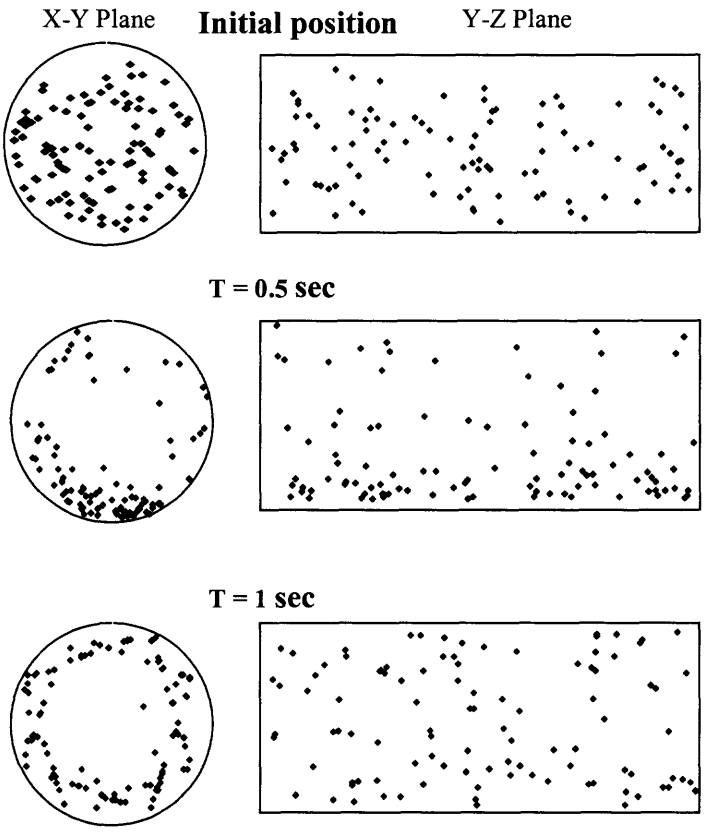

Figure 5.17 Snapshots of particles inside the re-circulating tube.

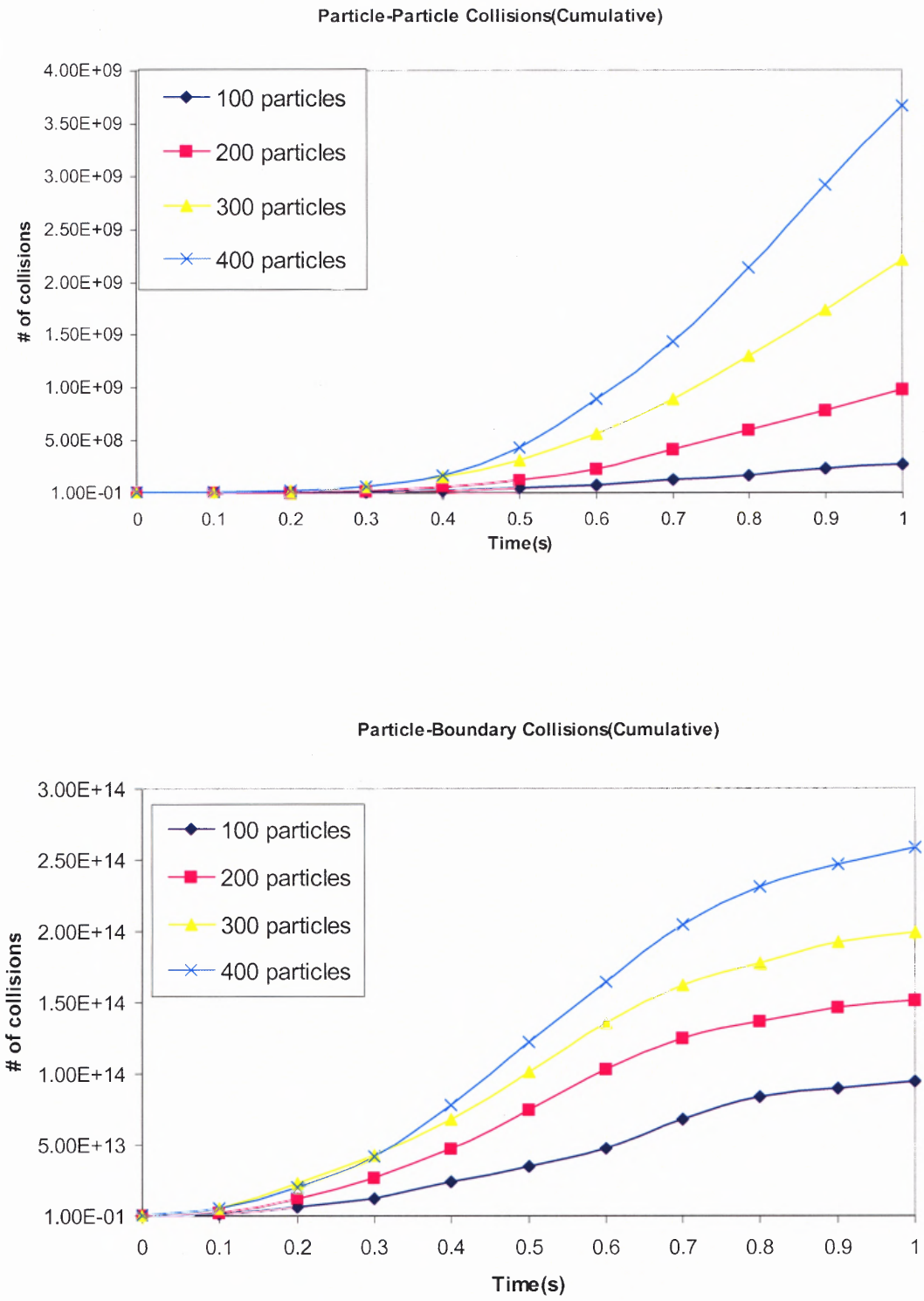

Figure 5.18 Cumulative collisions of particles inside the re-circulating tube.

It is clear from these plots that the particle-boundary interactions are more than the particle-particle collisions by at least 3 orders of magnitude. Number of collisions per particle are also computed and shown below in Figure 5.19.

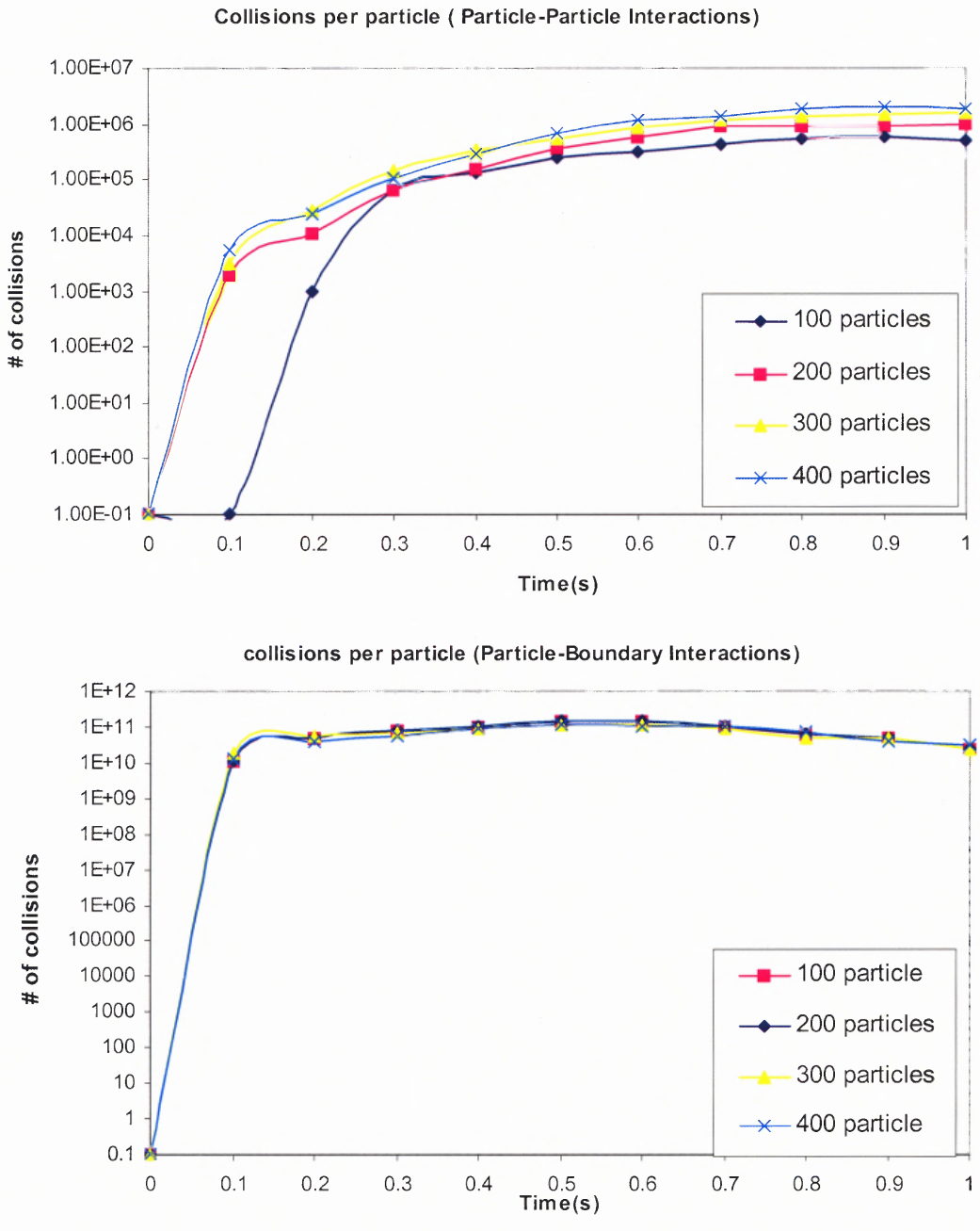

Figure 5.19 Collisions per particle inside the re-circulating tube.

The trend seen from above plots clearly indicate that the flow inside the pipe gets stabilized quickly. The particle-particle interactions computed as per particle is of the order of 10^6 whereas the particle-boundary interactions per particle is of the order of 10^{11}. Loading does affect the particle-particle collisions but does not seem to affect the particle-boundary interactions much. It should be noted that with few number of particles as used in this run (100 to 400), these number of collisions are extremely high and thus indicate the effect of re-circulating pipe in the coating of particles. The forces calculated as averaged per particle, normal and tangential are shown in the Figure 5.20.

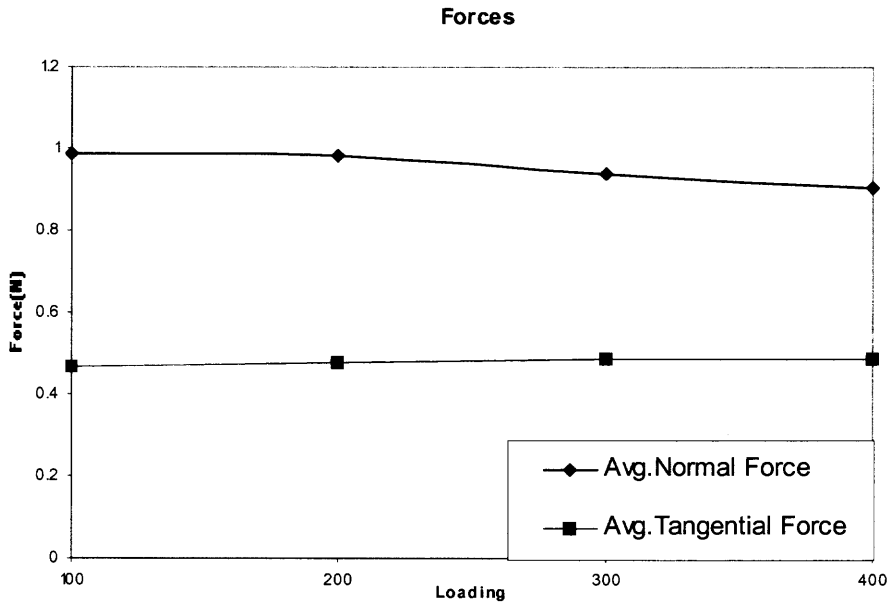

Figure 5.20 Average forces per particle inside the re-circulating tube.

Average normal force is higher than the average tangential force per particle for different loading of particles. Average normal force of the order of 0.9 N, while the average tangential force is of the order of 0.45 N. It may be noted as this magnitude of the forces

is also extremely high. However, the loading does not seem to affect the the magnitude of both normal as well as tangential forces.

5.3 Coupling Using CFD

5.3.1 Introduction

Another effort in the direction of coupling of gas and solid phase has been made in this section, using CFD techniques. Commercial software Fluent (v. 5.5) is used to analyze the flow inside the mixing chamber of the hybridization system. The algebraic slip mixture (ASM) model was employed as the multiphase model in the computation. The velocity profiles, volume fraction and pressure profiles for the gas and particulate phases were analyzed. In addition, the results of different volume fractions were compared.

The advantage of ASM model is that the two-phase model can be simplified that allows the phases to move at different velocities. Continuity and the momentum equation were solved to model the two phases (fluid and particulate), the volume fraction equation for the secondary phase, and an algebraic expression for the relative velocity. An interface between two immiscible phases was not considered and the phases were considered to be interpenetrating. The volume fractions α_q and α_p for a control volume was taken in the range from 0 and 1, depending on the space occupied by phase q and phase p.

5.3.2 The Continuity Equation

The continuity equation for the mixture is

$$\frac{\partial}{\partial t}(\rho_m) + \frac{\partial}{\partial x_i}(\rho_m u_{m,i}) = 0 \qquad (5.2)$$

Mass transfer is not allowed in the algebraic slip mixture model.

5.3.3 The Momentum Equation

The momentum equation for the mixture was obtained by summing the individual momentum equations for both phases.

It is expressed as

$$\frac{\partial}{\partial t}\left(\rho_m u_{m,j}\right)+\frac{\partial}{\partial x_i}\rho_m u_{m,i}u_{m,j} = -\frac{\partial p}{\partial x_j}+\frac{\partial}{\partial x_i}u_m\left(\frac{\partial u_{m,i}}{\partial x_j}+\frac{\partial u_{m,j}}{\partial x_i}\right)+\rho_m g_j + F_j + \frac{\partial}{\partial x_i}\sum_{k=1}^{n}\alpha_k\rho_k u_{D_k,i}u_{D_k,j} \tag{5.3}$$

where n is the number of phases and ρ_m is the mixture density:

$$\rho_m = \sum_{k=1}^{n}\alpha_k\rho_k \tag{5.4}$$

μ_m -viscosity of the mixture: $$\mu_m = \sum_{k=1}^{n}\alpha_k\mu_k \tag{5.5}$$

$\vec{u}_m$ - Mass-averaged velocity:

$$\vec{u}_m = \frac{\sum_{k=1}^{n}\alpha_k\rho_k\vec{u}_k}{\rho_m} \tag{5.6}$$

and $\vec{u}_{D_k}$ are the drift velocities:

$$\vec{u}_{D_k} = \vec{u}_k - \vec{u}_m \tag{5.7}$$

5.3.4 The Relative (Slip) Velocity and the Drift Velocity

The relative velocity (also referred to as the slip velocity) is defined as the velocity of the secondary phase *(p)* relative to the primary phase *(q)* velocity:

$$\vec{v}_{pq} = \vec{u}_p - \vec{u}_q \tag{5.8}$$

The drift velocity and the relative velocity $\vec{v}_{pq}$ are connected by the following expression:

$$\vec{u}_{D_p} = \vec{v}_{pq} - \sum_{i=1}^{n} \frac{\alpha_i \rho_i}{\rho_m} \vec{v}_{qi} \tag{5.9}$$

The basic assumption of the ASM model is that, to prescribe an algebraic relation for the relative velocity, a local equilibrium between the phases should be reached over short spatial length scales. The form of the relative velocity is given by

$$\vec{v}_{pq} = \tau_{pq} \vec{a} \tag{5.10}$$

where $\vec{a}$ is the secondary phase particle's acceleration and τ_{pq} is the particulate relaxation time:

$$\tau_{pq} = \frac{\rho_p d_p^2}{18 \mu_q} \tag{5.11}$$

where d_p is the particle diameter.

5.3.5 The Volume Fraction Equation for the Secondary Phase

From the continuity equation for the secondary phase, the volume fraction equation for the secondary phase can be obtained as:

$$\frac{\partial}{\partial t}(\alpha_p \rho_p) + \frac{\partial}{\partial x_i}(\alpha_p \rho_p u_{m,i}) = -\frac{\partial}{\partial x_i}(\alpha_p \rho_p u D_{p,i}) \tag{5.12}$$

5.3.6 Simulation Parameters

Simulation studies were studied into two different parts. In the first part, to have a better understanding of the dynamic behavior of gas/particle flow, a simple case of single phase

(gas) Hybridizer system was studied. In the second part, two cases with the particle volume fraction of 3% and 10% were studied respectively for comparisons. The particle properties were set to those of silicon. Gas properties were set to equal those of air.

The system geometry is previously shown in Chapter 4. A total of around 278,000 tetrahedral meshes were used in the simulation and the rotational speed was set to 5000 rpm for both cases.

5.3.7 Results

Simulated flow fields are shown in Appendix B for the rotational speeds of 5000, 8000, 10000 and 15000 rpm. The velocities of airflow are increasing with the rotational speed as seen in the fluid only case and as discussed in chapter 4. The magnitude of the velocities decreases in the multi-phase flow by approximately 10%. There are still three distinct regions where the velocity field is different. The velocities start increasing from the center of the mixing chamber till the outer wall. Airflow is dominant near the blade zones.

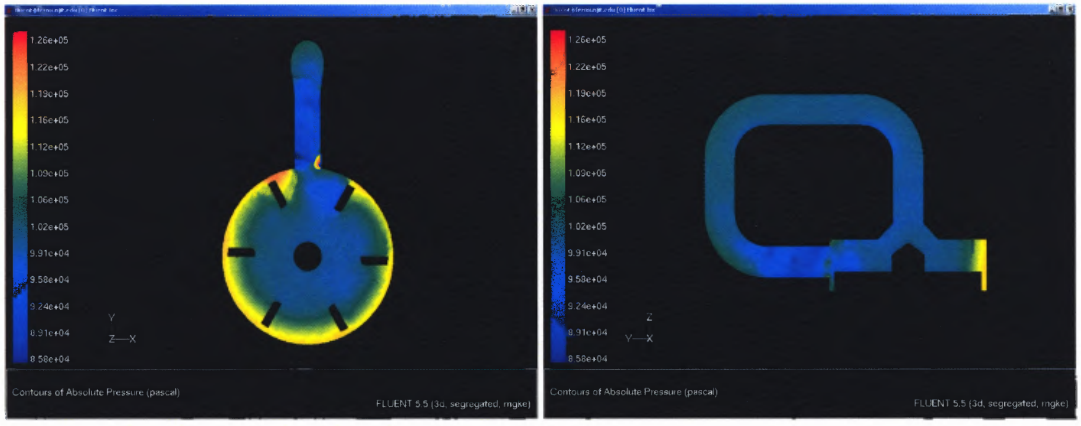

Figure 5.21 Pressure Contours (Volume Fraction of 0.03).

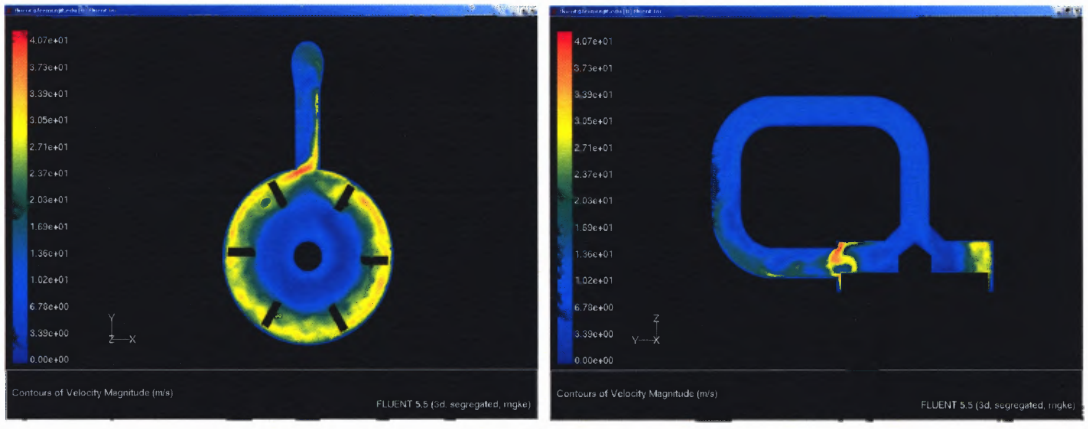

Figure 5.22 Velocity Contours (Volume Fraction of 0.03).

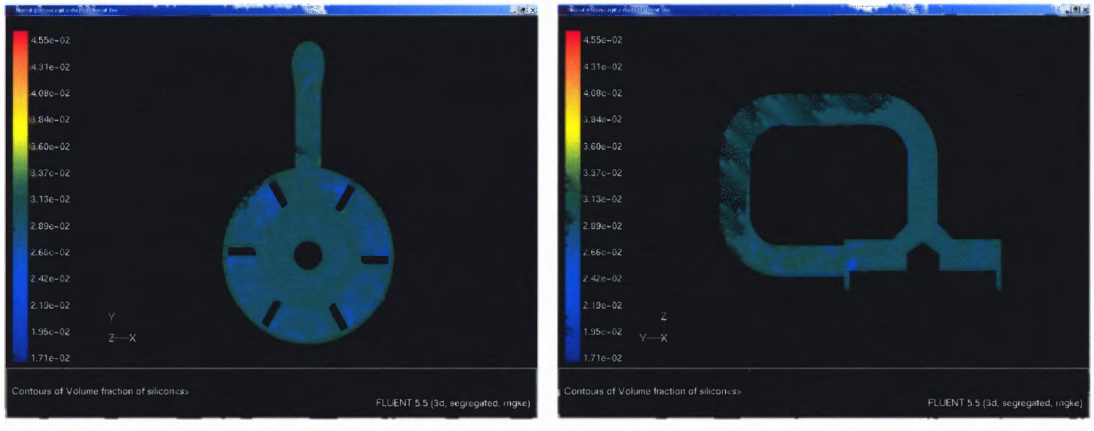

Figure 5.23 Volume Fraction Contours (Volume Fraction of 0.03).

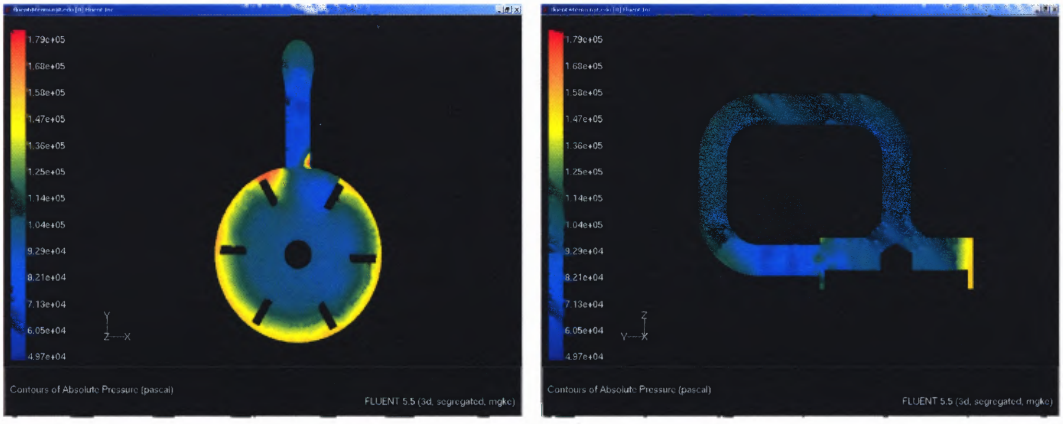

Figure 5.24 Pressure Contours (Volume Fraction of 0.1).

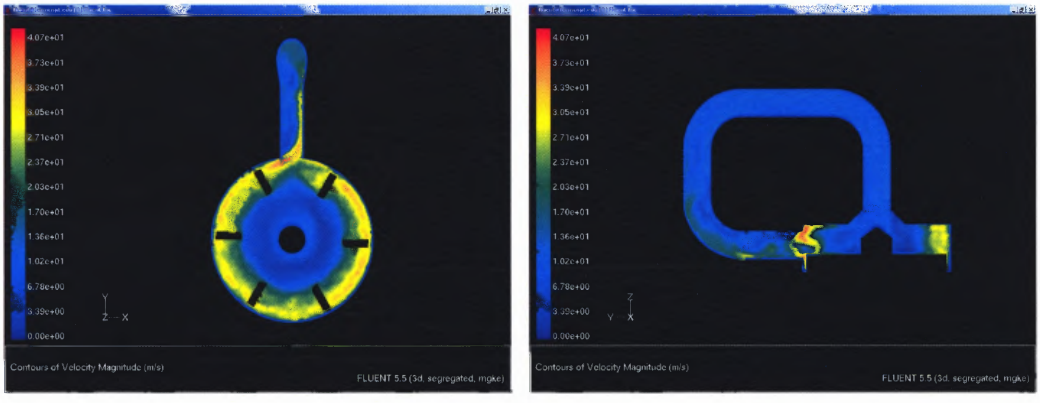

Figure 5.25 Velocity Contours (Volume Fraction of 0.1).

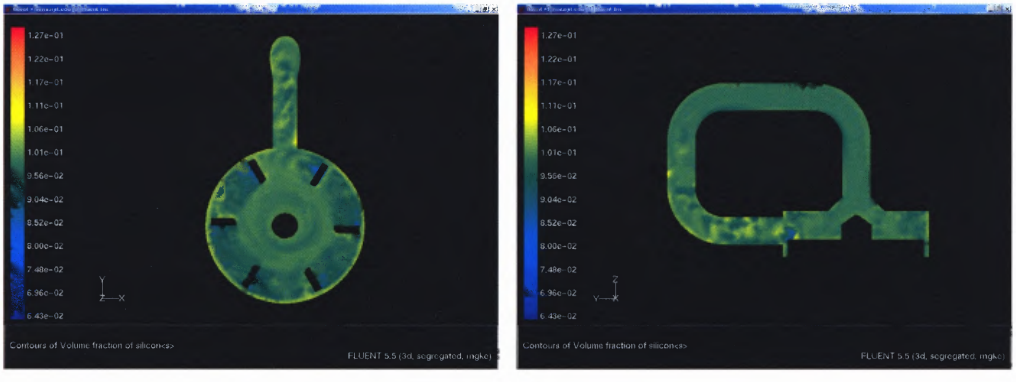

Figure 5.26 Volume Fraction Contours (Volume Fraction of 0.1).

Two cases of different volume fraction were studied using the multi-phase model. The volume fraction was taken as 0.03 and 0.1 for these cases, respectively. The results are

shown in Figures 5.21-5.23 and 5.24-5.26 for the volume fractions of 0.03 and 0.1 respectively. The velocity contours for both the cases remain almost identical, thus we can conclude that the flow is dominant enough not to be affected by the increase in the volume fraction. However, the pressure profiles are different. As the volume fraction is changed from 0.03 to 0.1, the pressure distribution becomes wider. Higher pressure is obtained near the outer walls of the mixing chamber. This may be because of higher gradient of pressure, needed to drive the particles flowing with the gas stream since the average density for the two-phase flow is increased with higher volume fraction of the particles. The regions where velocities endured greater changes in values were also evident. These areas included the regions near the outer rims of the six blades and the outlet region from chamber to pipe. Based on Newton's Second Law, these areas must also be the regions that experience higher forces. From the volume fraction contours, it was seen that the volume fraction of particles fluctuated by a small amount around the average value of the whole system.

5.3.8 Scaling Investigation of the Hybridizer System

Another attempt to further investigate the hybridization system is done by scaling up and down its normal size by keeping the tip velocity constant. The scaled versions are studied using CFD techniques to understand the effect on velocity, pressure, and turbulent intensity profiles for both single and multi-phase flows. The scaled down version used is 20% of the original size while the scaled up version is 5 times bigger than the original size. The results of velocity profiles are shown in Figure 5.27.

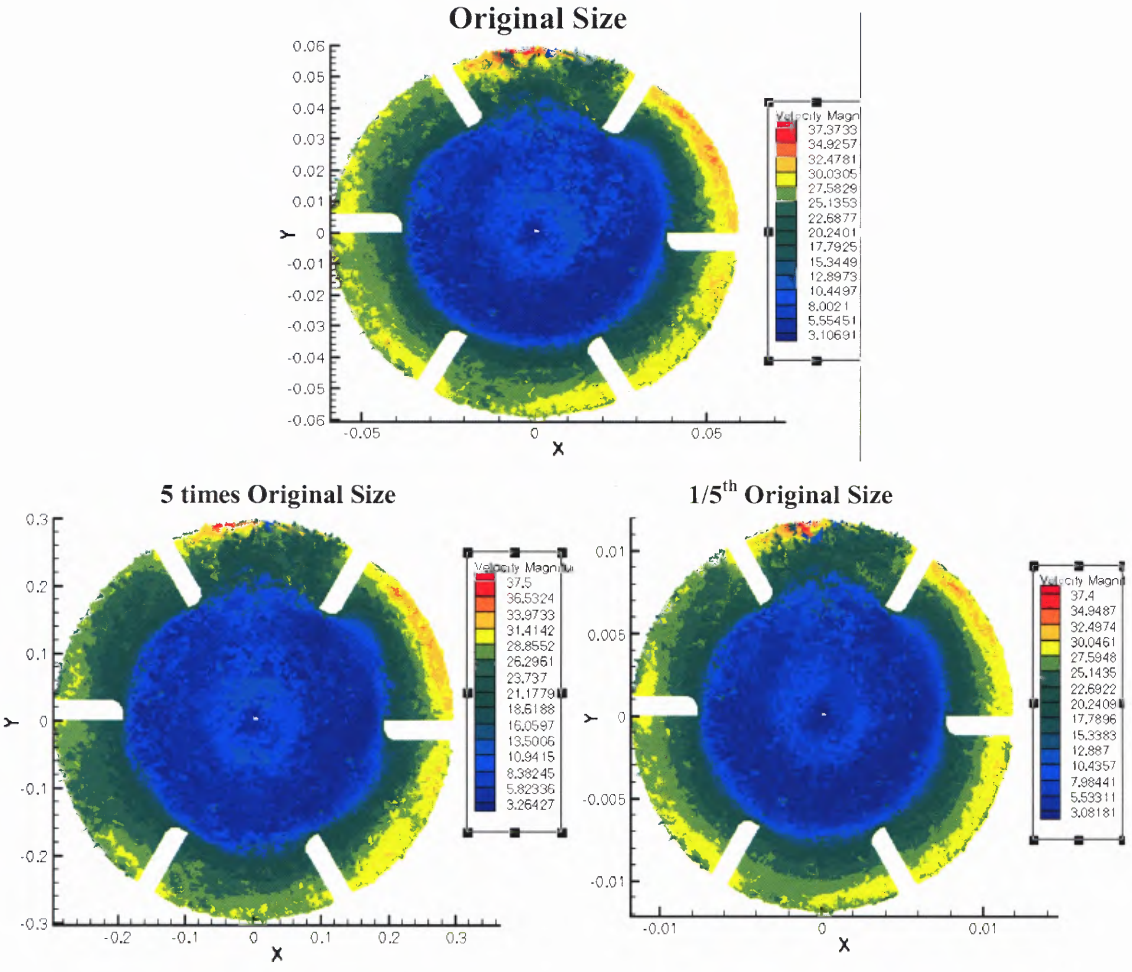

Figure 5.27 Velocity contours of scaled up and down systems.

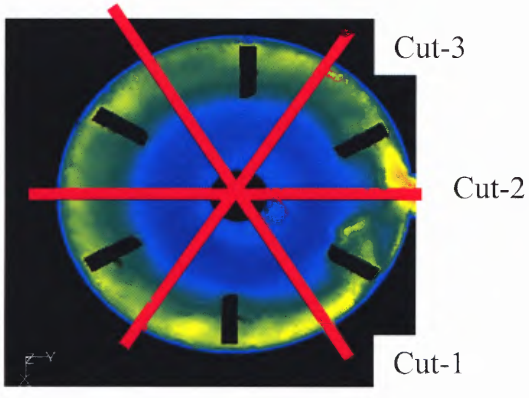

Figure 5.28 Cuts taken at different sections inside the mixing chamber.

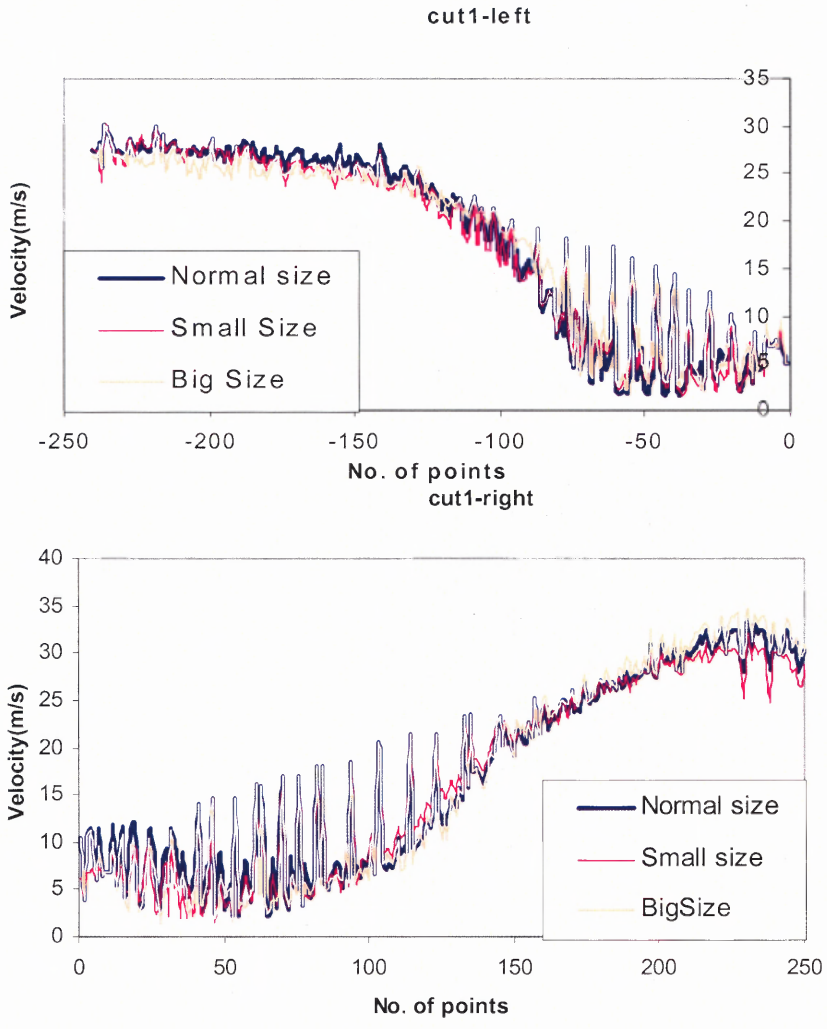

Figure 5.29 Velocity field across the section taken at cut-1.

As shown in the Figure 5.28, cuts are taken at different sections to analyze these velocity contours quantitatively. The plots shown in Figure 5.29, illustrate the velocity magnitudes at these cuts. As seen, the velocities are not affected significantly even after scaling up and down the original size of the hybridizer system.

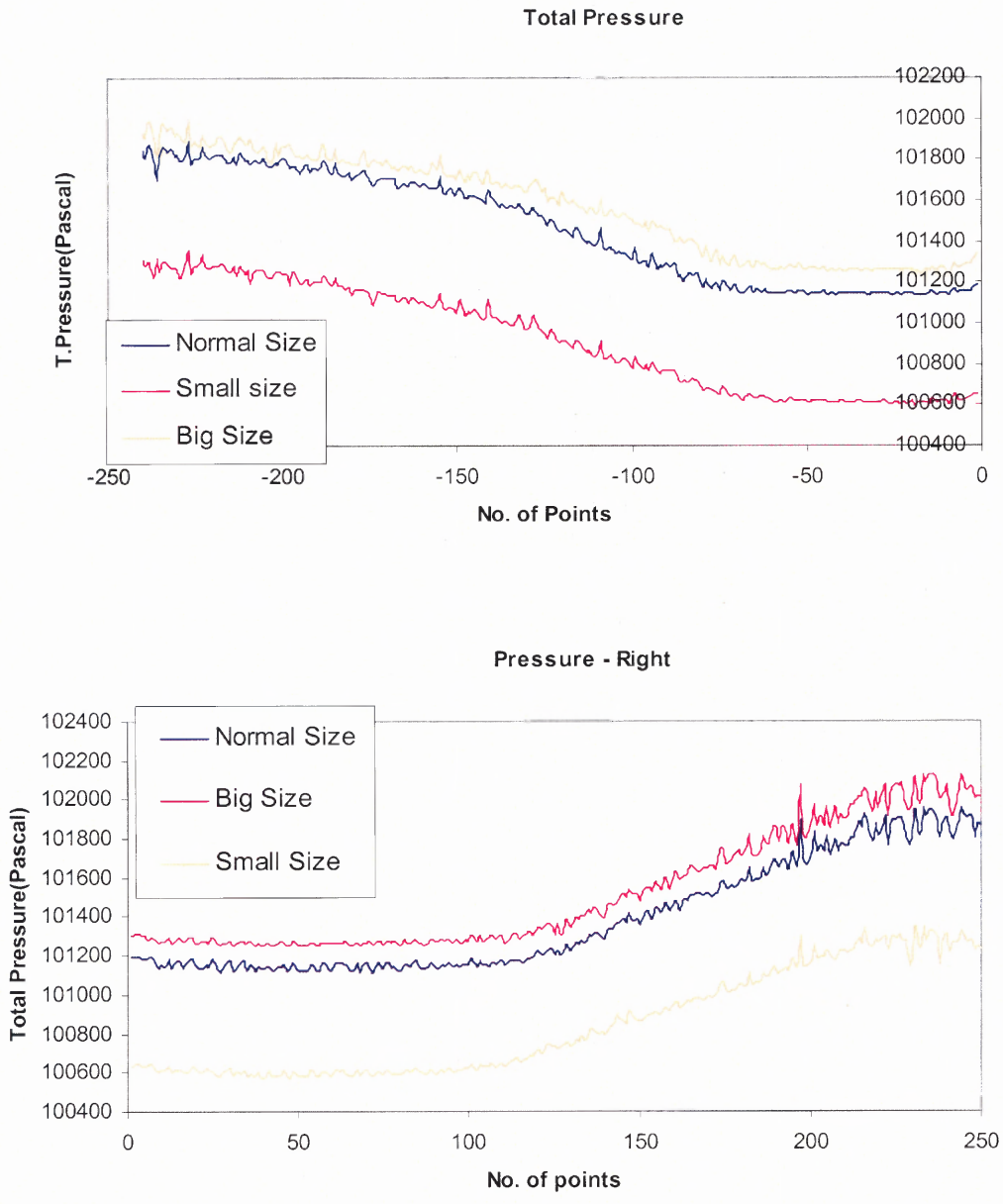

Figure 5.30 Pressure field across the section taken at cut-1.

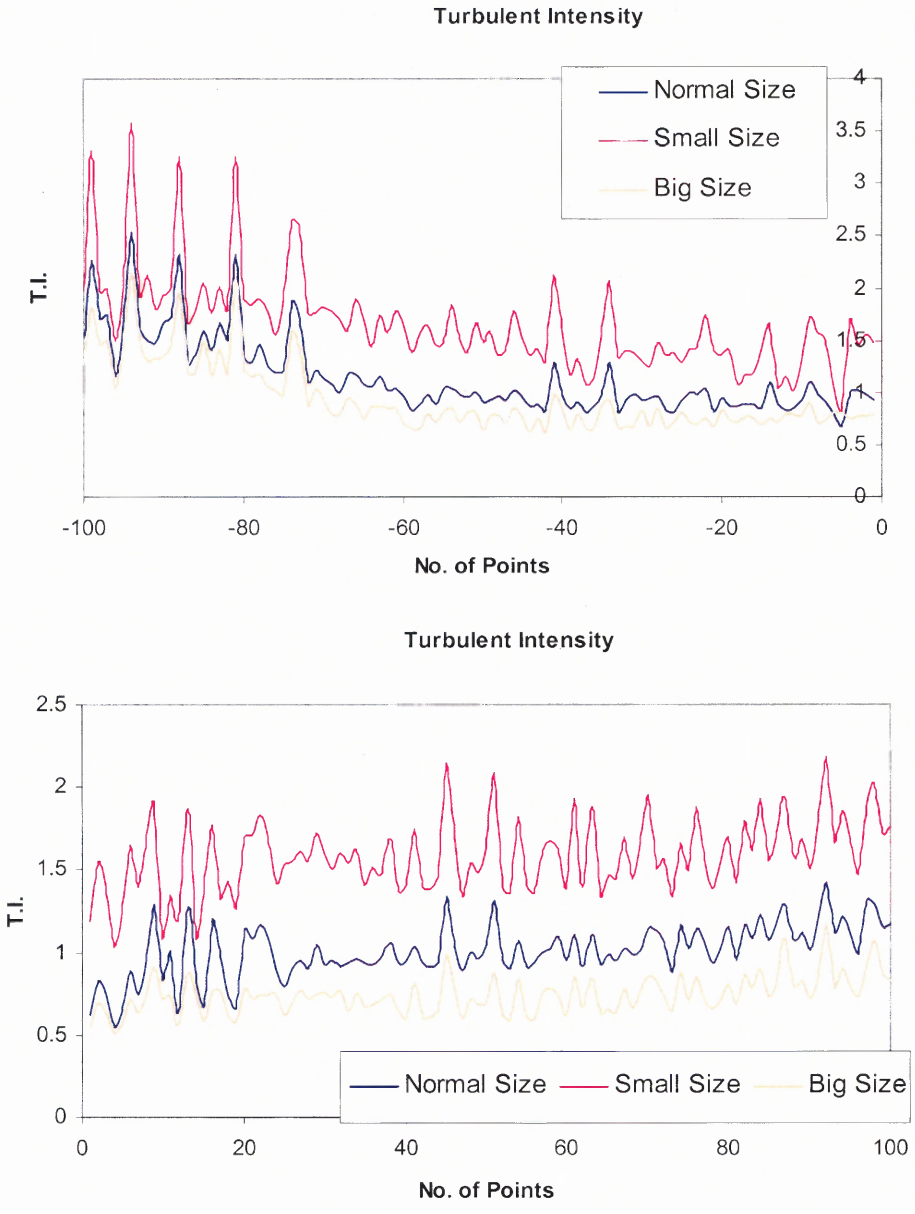

Figure 5.31 Turbulent Intensity field across the section taken at cut-1.

As shown from Figures 5.30, and 5.31, pressure as well as the turbulent intensity distributions across the chamber varies significantly for the scaled down system, however the scaled up system has close resemblence to the values of original size system.

Similar approach is adopted while analyzing the multiphase model of the scaled up and scaled down systems. Volume fraction is varied from 1 to 3%. It is seen that the

velcoties of particles as well as the airflow are not affected by increasing the volume fraction even upto 10%. Figure 5.32 shows the magnitude of velocities comparison for 1% and 3% volume fractions for the original size system. Similar trend is seen for the scaled sizes.

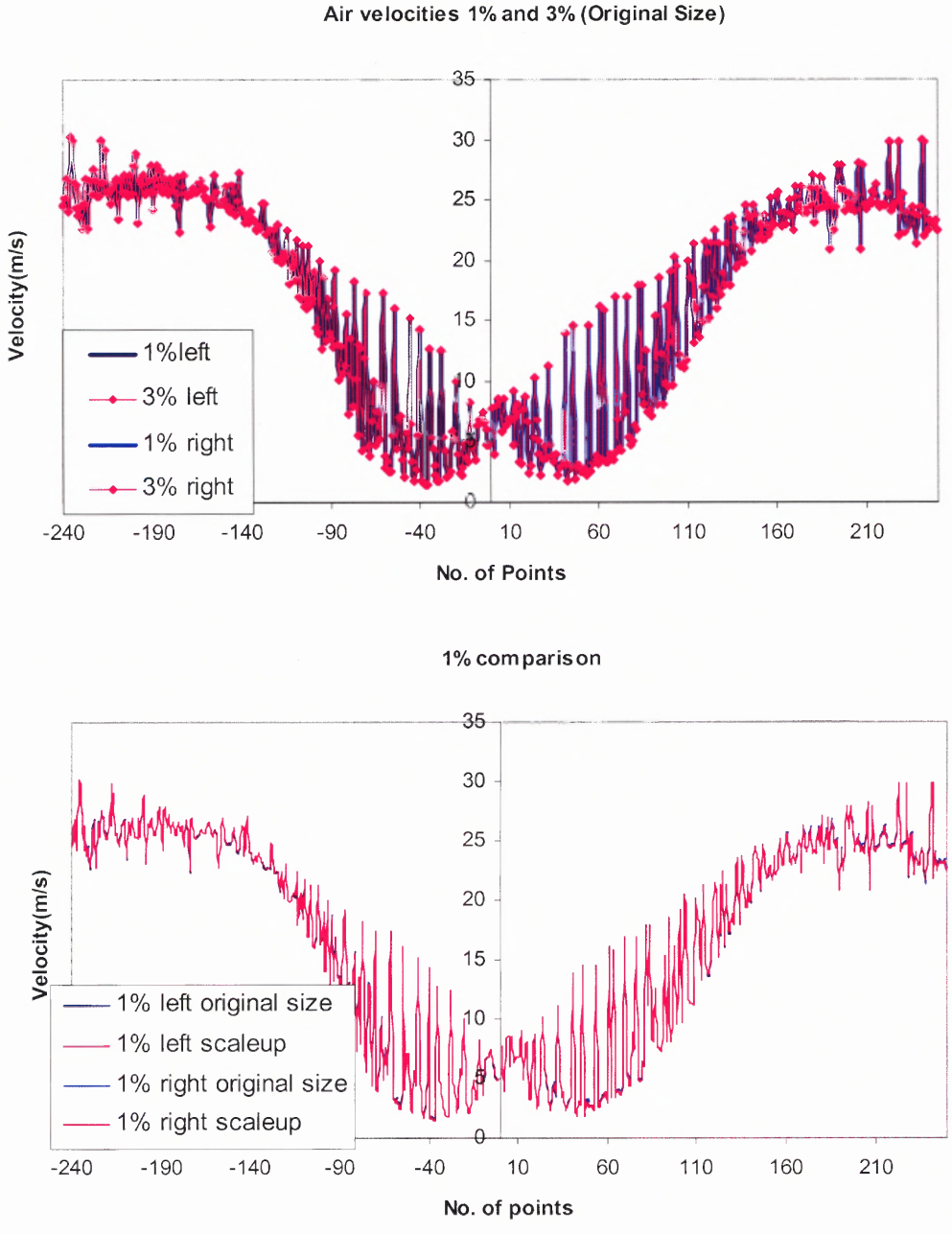

Figure 5.32 Comparison of Multiphase model velocities.

5.4 DEM of Original Size System

As may be noted, the DEM simulations carried out earlier in this chapter as well as explained in chapter 3, the size of the system was scaled down, in order to achieve the faster computational speed. In this section, attempt has been made to model the hybridizer system by increasing the particle diameter up to 1mm. Results shown here include the particle-particle as well as particle-boundary interactions and the forces. Velocities in different zones inside the mixing chamber are compared to the velocities obtained using multiphase model of Fluent. Rotational speeds used for the simulations are 5000 and 10000 for the loading of 1000 and 1500 particles. Figure 5.33 and 5.34 show the particle-particle and particle-boundary collisions as calculated per particle for 5000 rpm.

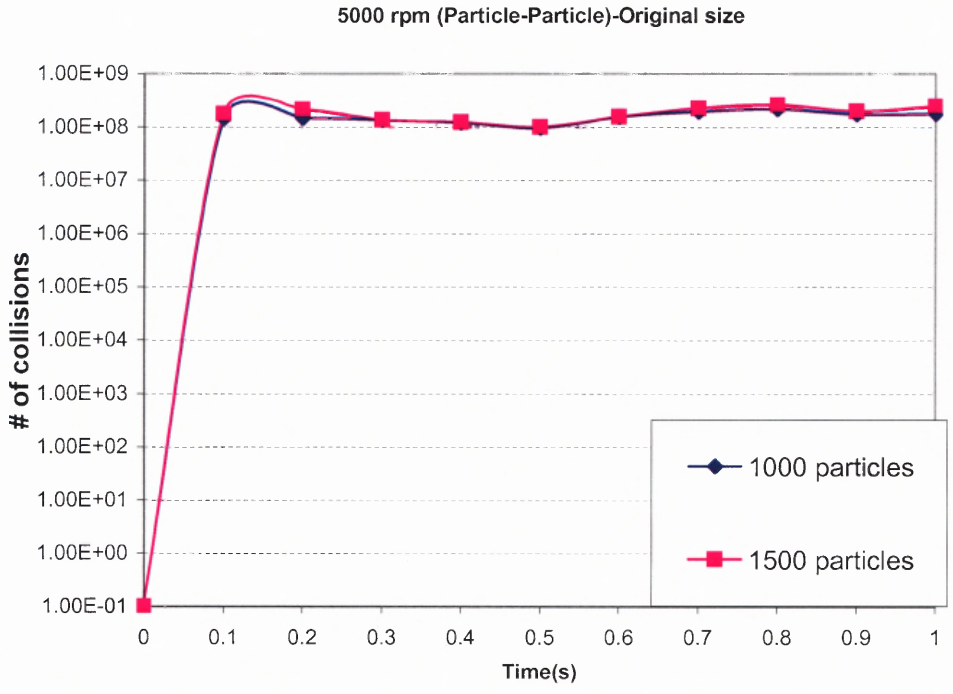

Figure 5.33 Particle-particle interactions for 5000 rpm.

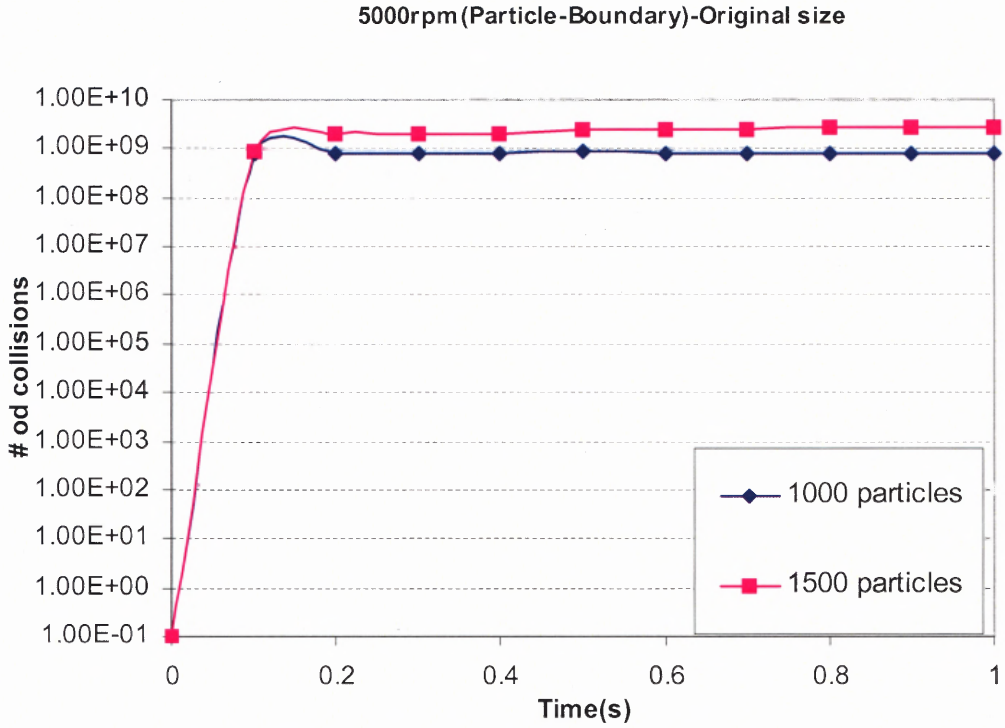

Figure 5.34 Particle-boundary interactions for 5000 rpm.

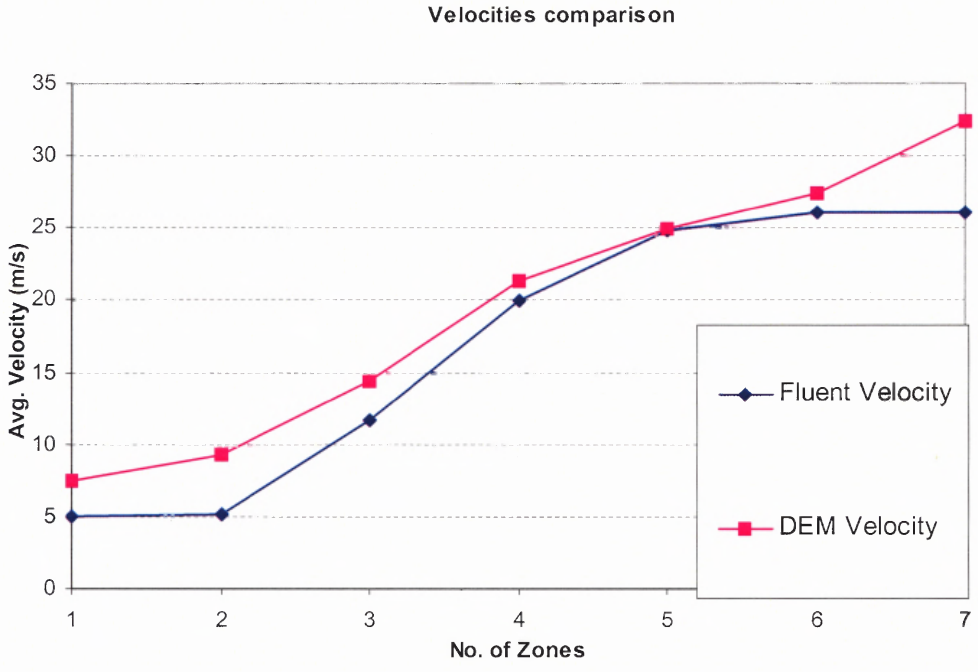

Figure 5.35 Velocity comparison for original size system.

As seen from these plots, the particle-particle interactions are of the order of 10^8, while the particle-boundary interactions are of the order of 10^9. The particle-particle interactions are not affected by the loading particles but there is a significant rise in the number of collisions for the particle-boundary interactions. Velocities are compared for the different zones in the mixing chamber. The values are found to be in good agreement.

5.5 Conclusions

In this chapter, the effect of air drag on the particles inside the mixing chamber of the hybridization system is studied using different available numerical techniques. The effect of air drag on the particles studied using the coupling of DEM and the fluid velocities obtained from Fluent indicated an increase of normal and tangential forces on the particles. The normal forces indicated that the effect of loading of particles is not a predominant factor. The number of collisions between the particles as well as with the boundaries of the system were seem to be reduced under the affect of air drag. The non-cumulative curves of the collisions indicated that the system got stabilized after about 0.2 seconds of simulation. Number density distribution of particles showed that the particles were occupying about 90% of the region near the blades. Hence, the flow of particles under this drag effect is dominated near the outer part of the chamber, where the blades are rotating at very high speeds. The multi-phase model was studied for two different volume fractions. The velocity contours did not indicate much change, however, there was a pressure rise for the higher volume fraction of particles.

CHAPTER 6

IMPROVEMENT OF HUMIDITY RESISTANCE OF MAGNESIUM POWDER USING DRY PARTICLE COATING

Dry particle coating is used to enhance the humidity resistance of ground magnesium powder (primary size 75mm) by coating its surface with carnuba wax (primary size 15mm). Coating is done using MAIC (Magnetically Assisted Impact Coating), and two high-speed impaction-coating devices, the Hybridizer and Mechanofusion system. The uncoated and coated samples are characterized by scanning electron microscopy (SEM), humidity tests, and X-ray diffraction (XRD). SEM images indicate that in addition to being coated, ground magnesium particles, which are irregularly shaped, are smoothened and rounded off in all of the coating machines. The wax particles coated onto the surface of the magnesium particles in MAIC are mainly observed in and around the cracks, whereas in the Hybridizer and Mechanofusion the wax is softened and spread more evenly over the magnesium surface. The results of the humidity tests show a significant improvement in the humidity resistance of ground magnesium powder after coating in all three devices. These results are also verified by XRD analysis. It is shown that the humidity resistance of the coated ground magnesium is comparable to that of atomized magnesium even when only 1 to 2% by weight of wax is applied.

Powdered magnesium has a wide range of applications in various chemical, pharmaceutical, metallurgical, and agricultural industries. Specific applications include steel desulphurization, pyrotechnics, metal matrix composite filler, powder metallurgy, etc., see Dreizen et al. (2001), Shoshin et al. (2001).

6.1 Introduction

Magnesium is a highly energetic material, i.e., it has a tendency to catch fire, and it also has a high affinity for oxygen and water. Figure 6.1 shows a scanning electron micrograph (SEM) image of commercially available magnesium powder. In its ground form as shown, the particle is irregularly shaped with a large number of cracks where the formation of hydroxide occurs, when exposed to moisture. Figure 6.2 shows a higher magnification SEM image of as-received ground magnesium after 100 hours of exposure to the atmosphere. It clearly shows the very different morphology of magnesium hydroxide, a needle type structure. The formation of magnesium hydroxide deteriorates many of the desirable properties of ground magnesium, e.g., the reduction or even elimination of its pyrotechnic properties and hence severely limits its applications.

An alternative to ground magnesium powder is atomized magnesium. Atomized magnesium particles are spherical shaped and have a lower tendency to form hydroxide on its surface, i.e., it has a greater shelf life than ground magnesium. Kalyon et al. (1996) showed that when ground and atomized magnesium powders were exposed to 100% humidity and 65°C for a short test duration, ground magnesium powder formed hydroxide close to 5% by weight, or about 2.5 times greater than that formed by atomized magnesium powder. The main reason for this difference appears to be the larger surface area to volume ratio in the ground form. However, the manufacturing and handling cost of atomized magnesium is significantly higher than that of ground magnesium. Hence, it is desirable to develop a method that can cost-effectively improve the moisture resistance property of ground magnesium.

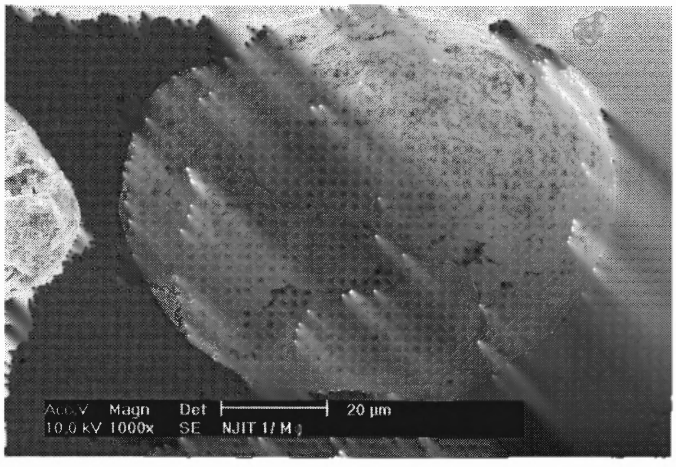

Figure 6.1 SEM image of ground magnesium particles (as received).

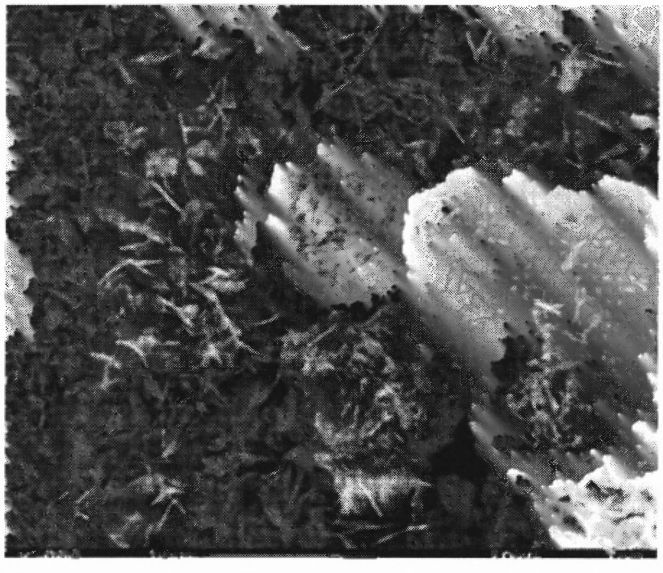

Figure 6.2 Hydroxide formation on the surface of as-received magnesium after 100 hours of exposure to atmosphere.

Kaneyasu et al. (1995) observed that crushing ground magnesium powder into finer particles increases the water absorption properties of magnesium. In order to achieve a better hydration resistance, they used a wet coating technique to add organic silicon compounds on the surface. Surface modification of metal powders such as sodium, magnesium, aluminum and tantalum was also done using a resin binder in a solvent by Mitsui Mining and Smelting (1990). The metal was coated with metal alkoxides, the condensate having non-hydrolyzable groups attached to the metal. The hydrophobic nature of the non-hydrolyzable groups improves the hydration resistance.

Alternatively, dry particle coating techniques can be used to modify particle surfaces by coating a protection layer to achieve hydration resistance. Several dry particle-coating systems have been developed, such as Magnetically Assisted Impaction Coating (MAIC) (Ramlakhan 1998, Singh et al. 1997), Mechanofusion (Yokoyama et al. 1987, Naito et al. 1983), Theta composer (Alonso et al. 1989, Miyanami et al. 1994), Hybridizer (Honda et al. 1987, Takafumi et al. 1993) and Rotating Fluidized Bed Coater (Masaru et al. 1996). A comprehensive review of dry particle coating is given in (Pfeffer et al. 2000). In dry particle coating methods, as we have seen in Chapter 2, fine particles (guests) are attached or embedded onto the surface of larger particles (hosts) by means of high shear and/or impaction forces. The Hybridizer and Mechanofusion systems generate higher local temperatures as compared to MAIC and other dry coating methods. The coating strength also differs to a great extent depending on the properties of the hosts and guests and the particular dry coating process that is used. Dry particle coating methods are becoming more important in powder processing industries because of their ability to modify particle surface properties to suit the requirements of the particular applications

(Pfeffer et al. 2000). A distinct advantage of dry coating techniques over conventional wet coating methods is that they don't require any liquids or binders that may result in waste products. Additionally, no complex chemistry is involved to achieve the coating. Moreover, they do not require drying of the product and are therefore highly cost-effective and save energy.

The objective of this study is to develop a potentially cost-effective technique to preserve the pyrotechnic properties of ground magnesium by dry coating wax or silica onto the surface of ground magnesium particles. Various dry coating systems are used to accomplish this goal. The products are characterized by their morphology, speciation and moisture absorption. The performance of the various systems is also compared.

6.2 Experimental

Three dry particle-coating systems, MAIC, Hybridizer and Mechanofusion are used in this study to coat the particles. The coating mechanism and operating variables of these processes are described in detail in Chapter 2. Only some of the main features are briefly reviewed here. The experimental procedure is as follows. A weighed amount of host particles (magnesium powder) and guest particles (wax or silica) is placed into a processing chamber. Batch sizes of magnesium powder and guest particles are varied depending on the type of instrument and time of operation.

In MAIC, a pre-weighed mass of magnetic particles is also placed in the chamber, followed by the application of an oscillating external magnetic field around the processing device to agitate the magnetic particles. The magnetic particles spin and translate which results in collisions with host and guest particles, allowing coating to be

achieved by means of impaction of the guest particles onto the surface of the host particles. In the Hybridizer system, guest and host particles are mixed and due to the 6 ultra high-speed rotating blades in the mixing chamber, they collide with each other as well as with the walls of the unit. Coating is accomplished through the impaction between hosts and guests resulting from the high-speed rotation of the blades. The temperature inside the chamber is varied from 22°C to 60°C by controlling the temperature of inlet water into the cooling jacket of the mixing chamber. The mixing chamber is flushed with nitrogen gas to prevent ignition of the magnesium powder. In the Mechanofusion system, a mixture of guest and host particles is forced to pass through a very narrow clearance in a rotating chamber where high shear and compression forces are responsible for the coating. A scraper is used to remove the powder layer attached on the chamber wall.

The physical properties of the materials used in the experiments are given in Table 6.1. Two sets of experiments were carried out and the experimental conditions are listed in Table 6.2. In the first set of experiments, the choice of which guest particles (hydrophobic fumed silica or carnuba wax) should be used to coat the host particles (ground magnesium) was determined by comparing the performance of the coated products by humidity testing. In the second set of experiments, the effect of guest particle loading and different operating conditions were studied. The coated, as well as the uncoated, samples were then tested under nearly 100% humidity at 65°C. The morphologies of the coated products were characterized using a Philips XL 30 scanning electron microscope (SEM) as well as a Leo 982 Field Emission SEM. The products were

also characterized using X-ray diffraction (XRD) to determine the level of hydroxide formation on the surface of the coated and uncoated samples.

Table 6.1 Physical Properties of Materials

Host particle mean size: Magnesium (μm)	75
Guest particle mean size: Carnuba Wax (μm)	15
Guest particle mean size: Hydrophobic fumed silica (μm)	0.7
Magnetic particles (mm)	0.8 to 1.4
Melting point of wax °C	65

Table 6.2 Experimental Conditions of the Coating Processes

Set No	Guest Material	Mass ratio of guest to host	Coating device	Operating conditions	Processing Time (min)
I	1) Carnuba Wax 2) Hydrophobic Fumed silica	2%	Hybridizer	10000 rpm	2
II	Carnuba Wax	1%, 2%, 4% 5%, 10%, 20%	MAIC	Average Magnetic field strength- 1.4 mT Weight of Magnets to Sample- 3:1	10
		1%, 2%, 5%, 10%, 20%	Hybridizer	5000, 10000 rpm	2
		1%, 2%, 5% 10%, 20%	Mechanofusion	1000, 3000 rpm	5, 10, 20

6.3 Results and Discussion

6.3.1 Determination of Coating Material

The first set of experiments was carried out to choose a better coating material between hydrophobic silica and carnuba wax. The Hybridizer was used to accomplish the coating, and 2% by weight of the coating material was added. When magnesium comes in contact with water, hydrogen gas is generated through the following reaction:

$$Mg + 2H_2O \rightarrow Mg(OH)_2 + H_2 \qquad (6.1)$$

Therefore, the amount of water absorbed can be determined by measuring the amount of hydrogen gas generated. In each test, the magnesium powder batch size was 5g. The results generated, using the experimental test rig at Picatinny Arsenal, Dover, NJ are shown in Figure 6.3. The coated samples were also tested (fired) at Picatinny Arsenal and the coating showed no adverse effect on their pyrotechnic properties.

As shown in the Figure 6.3, the as-received Mg powder generated the highest amount of H_2. Magnesium coated with hydrophobic fumed silica reduced the amount of hydrogen generated but the wax-coated product showed the best performance, resulting in about half of the H_2 pressure increase as compared to the former. The large difference can be explained by observing the morphologies of the coating layers. Silica particles were discretely lodged on the surface of the magnesium while wax particles formed a film, which covered a larger fraction of the magnesium surface (as will be shown in the later sections). The film provided a greater coverage and hence less water absorption.

Due to its superior performance, only wax was used to coat the magnesium in subsequent experiments.

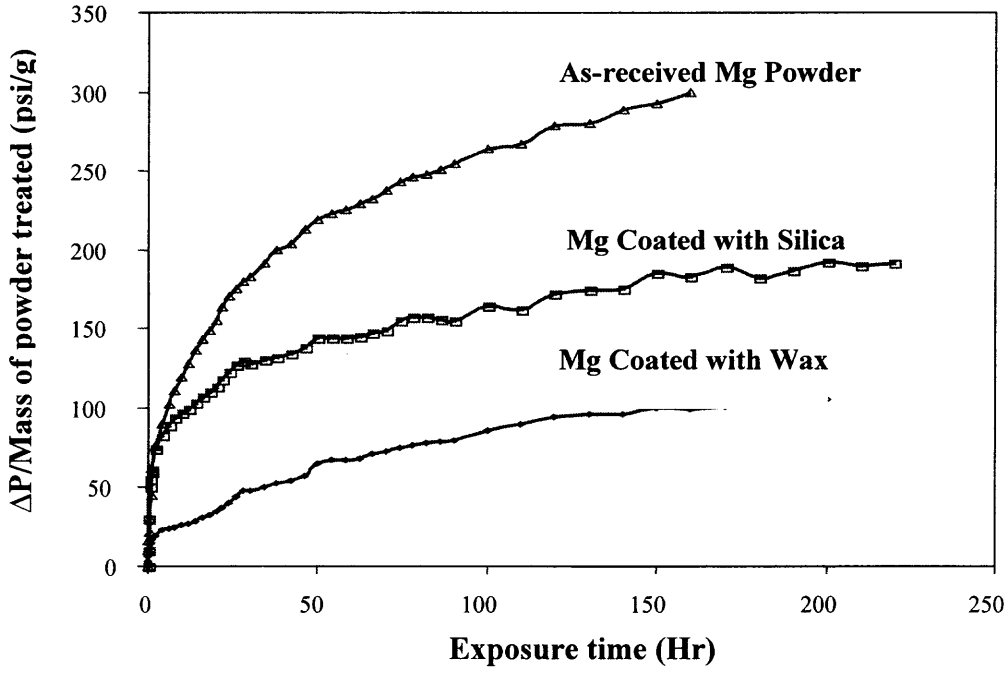

Figure 6.3 Comparison of H_2 pressure increase from coated samples with wax, hydrophobic fumed silica (processed in Hybridizer) and as-received magnesium powder.

6.3.2 Surface Morphology (SEM)

In the second set of experiments, the use of different dry coating systems and the effect of varying operating conditions on the coating were assessed. The surface morphology of the coated product from the MAIC process with different wax loadings is shown in Figure 6.4. In SEM, lighter elements absorb more electron energy and emit fewer electrons when illuminated with a beam of electrons, whereas denser materials

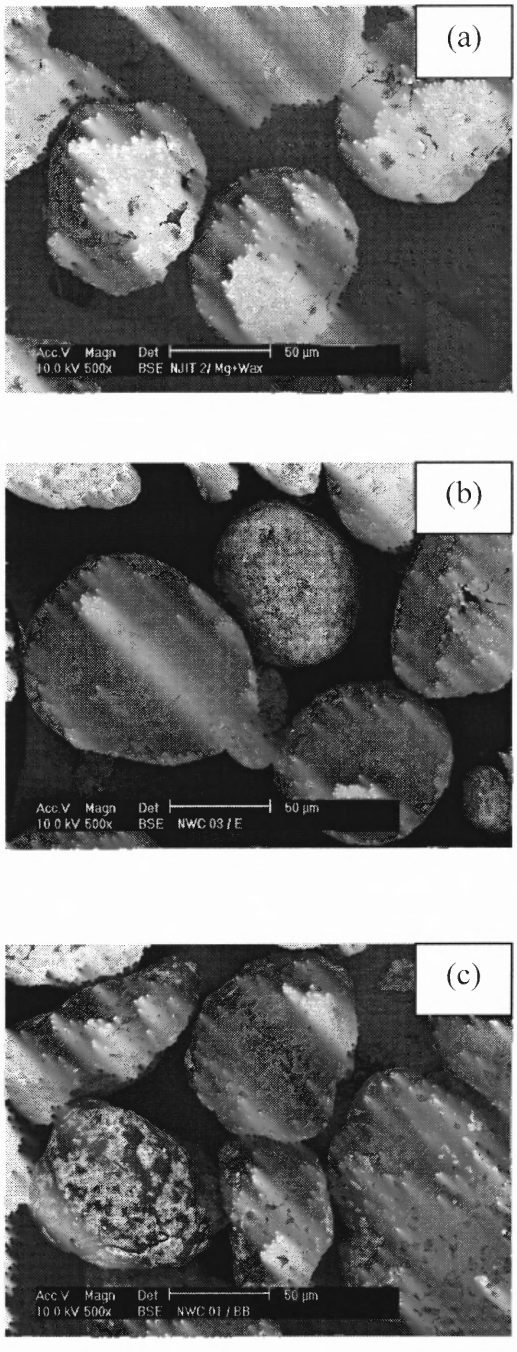

Figure 6.4 SEM images of magnesium coated with various loadings of wax in MAIC (a) 1% (b) 2% (c) 4%.

emit more electrons. Consequently, the dark spots correspond to wax coverage on the surface of magnesium assuming that carbon is the major component of wax. The SEM image of the as-received ground magnesium has been shown earlier in Figure 6.1. The particle in its original form is irregularly shaped with lots of cracks and a rough surface. As shown in Figure 6.4, particles processed in MAIC were smoother and rounded off as compared with the uncoated ground magnesium and the wax guest particles were discretely distributed on the surface. Greater wax coverage is observed on the surface of magnesium as the wax percentage is increased from 1% to 4%.

The coatings obtained using the Hybridizer and Mechanofusion with 2% wax are shown in Figure 6.5. Differences in the morphology of the wax coating in the three different coating devices is readily observed. More wax can be seen on the particles when they are processed in the Hybridizer or by Mechanofusion. Due to the higher forces and higher local temperature in these devices, wax was softened and spread over the surface of the particles, increasing the surface coverage. The higher surface coverage is critical to better moisture resistance as will be demonstrated in the following sections.

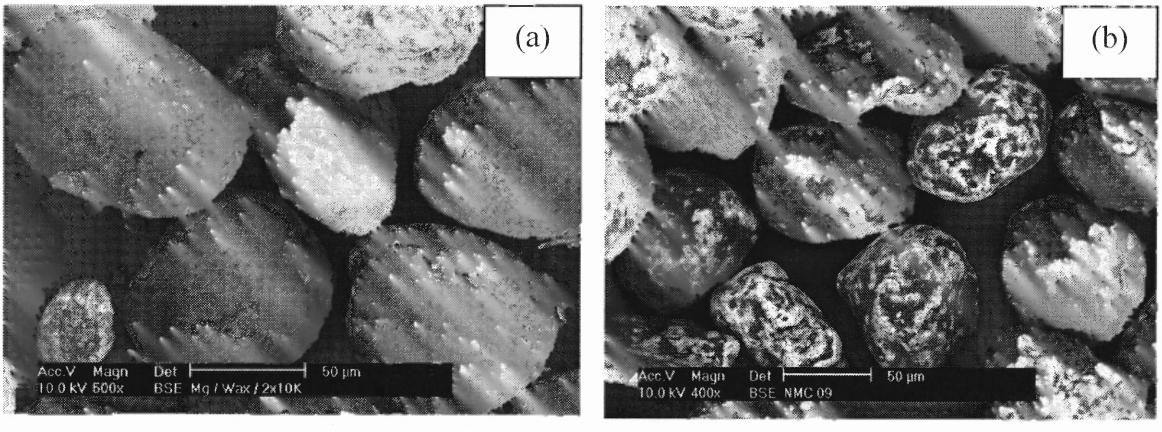

Figure 6.5 SEM images of magnesium coated with 2% wax:
(a) Hybridizer (5000 rpm, 2min) (b) Mechanofusion (1000 rpm, 10 min).

6.3.3 Water Immersion Test

Since the wax is hydrophobic, the coating should make the hydrophilic magnesium surface become hydrophobic. To qualitatively test if the coated magnesium becomes hydrophobic (i.e., less hydrophilic), the coated and uncoated samples were immersed in water to observe their hydrophilic or hydrophobic behavior. As expected, the uncoated sample settled in water (Figure 6.6). On the other hand, the coated sample (processed in the Hybridizer at 10000 rpm, for 2 minutes with 2% wax and exposed to the atmosphere for several months) floated on water. The coated product was observed to be still floating on water after 30 days, even though much of the surface was not coated with wax as shown in the SEM micrographs This transformation is due to the high hydrophobicity of the wax coatings.

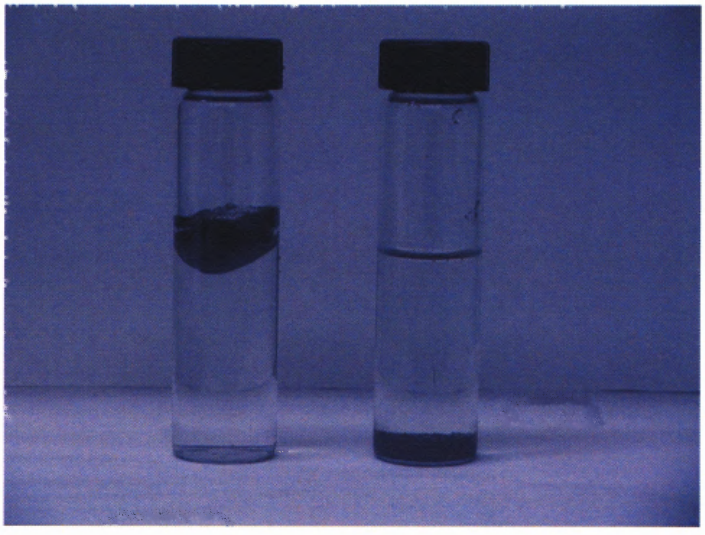

Figure 6.6 Ground magnesium powder settled in water (right) while the coated sample floating on water (left) after 30 days of exposure to atmosphere.

It is also likely that the wax may have sealed some of the free cracks, preventing the entry of water into the particle, further reducing its hydrophilicity. While this test does not provide quantitative results, it indicates that the layers of wax on the magnesium surface would repel moisture from the atmosphere, making it less hydrophilic. In the next section, humidity resistance tests, which are more quantitative, are described.

6.3.4 Humidity Tests

To evaluate the impact of the coating on the improvement in moisture resistance, humidity tests were carried out for the various coated products as well as uncoated samples. The test samples were kept in a container at nearly 100% humidity at 60°C for 100 hours or more to allow the formation of hydroxide on the surface of the magnesium particles. These were accelerated tests to simulate the increase in hydroxide formation after six months of normal shelf life. As the melting point of wax is 65°C, the temperature inside the chamber was kept at 60°C in order to avoid complete melting of the wax. Nevertheless, it is high enough to soften the wax so that it would cover the small cracks remaining on the surface of magnesium after the coating process. The samples were weighed at regular intervals of time. The weight increase in the samples was compared with the uncoated ground magnesium sample as well as the atomized magnesium sample tested at the same conditions.

The results of the samples coated in the Hybridizer at 5000 rpm and 10000 rpm with various wax loadings are shown in Figure 6.7. As seen, the water absorption rate was the highest for the uncoated ground magnesium, as expected. Very encouragingly, the coated samples reduced the absorbed amount of moisture to almost the same level as

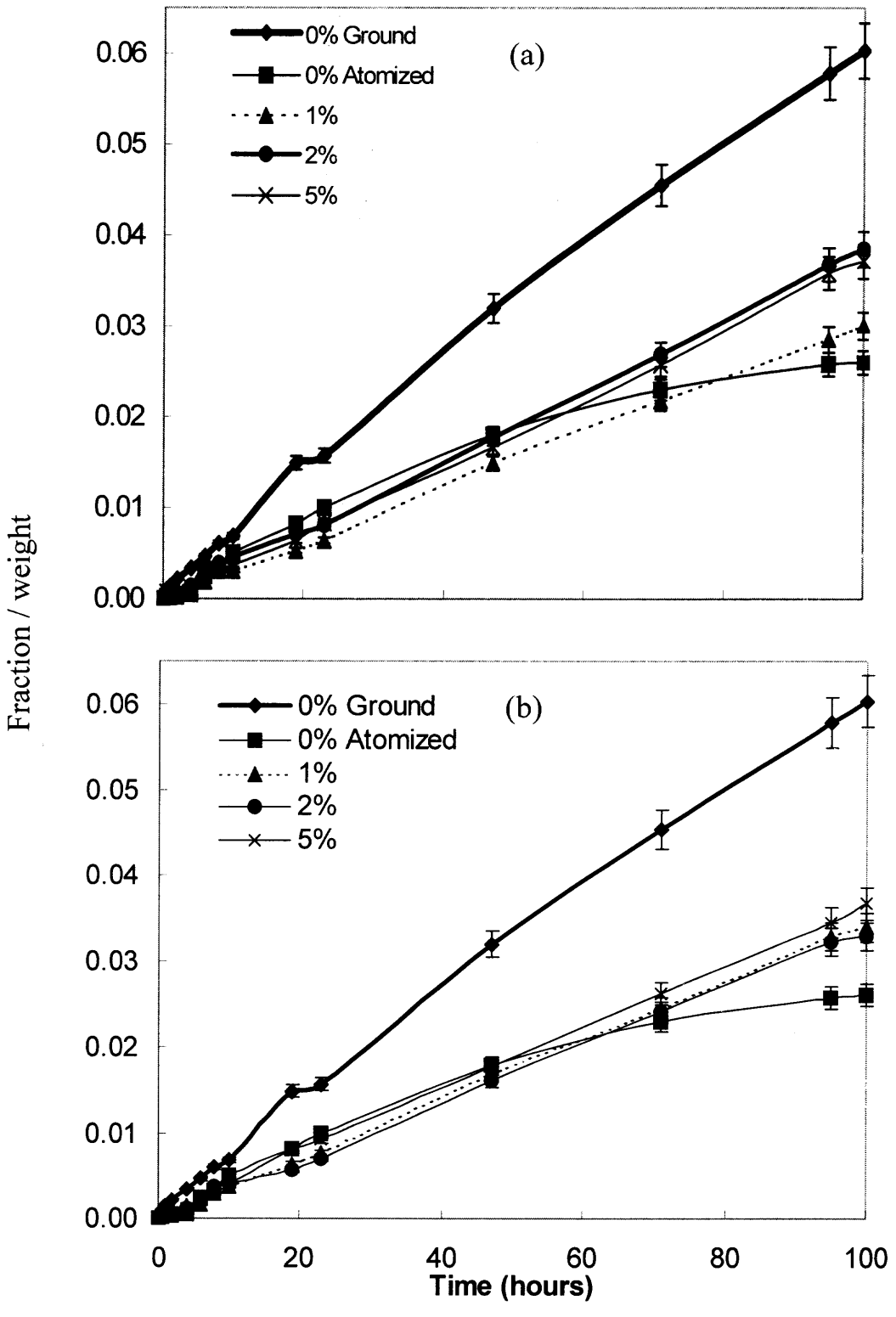

Figure 6.7 Humidity test for the Hybridizer products (2 minutes processing time): (a) 5000 rpm (b) 10000 rpm.

the atomized magnesium. The different percentages of wax used in the coating process did not yield much difference in the humidity tests. All these samples absorbed approximately the same amount of water indicating that 1% wax was enough to produce satisfactory results. In addition, there was also no discernable difference in water absorption for the products processed at different rotating speeds.

It should be noted that since the weight increase in these and subsequent tests is rather small, and that the test procedure requires frequent handling of these samples to measure their weight, the results are not highly accurate. In other words, they provide only a semi-quantitative description of the increase in humidity resistance.

Humidity tests were also performed for samples processed in the Mechanofusion and MAIC systems. The results are shown in Figures 6.8 and 6.9 respectively. For Mechanofusion, moisture absorption of the coated samples at various processing times is seen to be marginally less than that for the atomized uncoated magnesium. However, looking at the trend of these curves, it appears that as time increases beyond 70 hours of exposure, the atomized magnesium absorbs less water than the coated samples. This may be attributed to the fact that as the coated sample surface converts to hydroxide, the integrity of the wax coating is disturbed (refer to Figure 6.2), and its moisture resistance is somewhat reduced as compared to the uncoated atomized magnesium. It is also noted that higher processing times do not seem to show any major difference. For the MAIC experiments, the moisture absorption of the coated product is quite similar to that of the Mechanofusion processed samples, except that their degradation is faster, i.e., their moisture absorption becomes greater after 50 hours of testing.

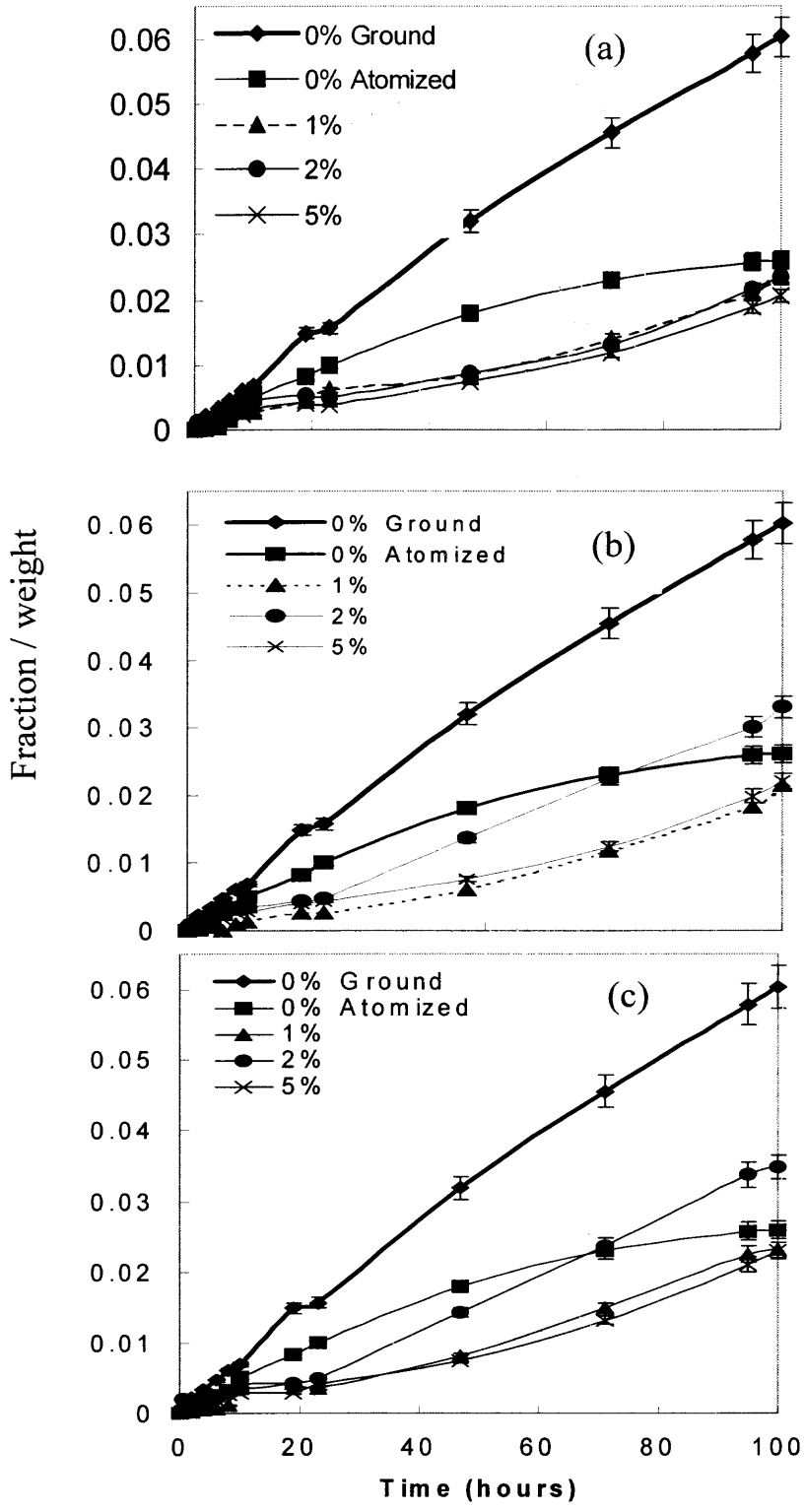

Figure 6.8 Humidity test for samples processed in the Mechanofusion system: (a) 5 minutes, (b) 10 minutes, (c) 20 minutes.

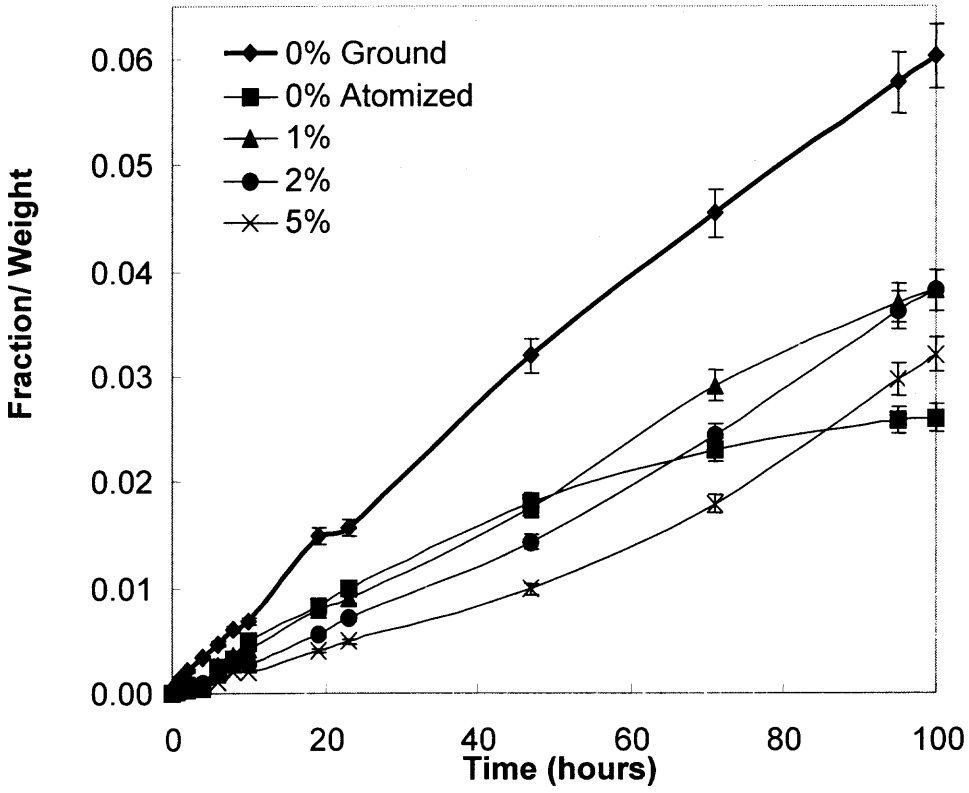

Figure 6.9 Humidity test for MAIC 10 min sample.

As seen from these results, while there were some differences, all of the products processed in the different coating systems showed practically similar results in the reduction of moisture absorption. The similarity for all the coated samples appears to be due to the fact that the humidity tests were carried out at 60°C so that the wax coated on the surface of the magnesium was softened. Therefore, all the cracks remaining on the surface of magnesium after coating were eventually filled with softened wax, resulting in better surface coverage and leaving less room for water entry. It should be noted that the coated product yielded even better moisture resistance (e.g., compare the Mechanofusion

and MAIC samples showing Mechanofusion to be better) if the wax was already softened in the coating process.

Generally, the moisture absorbed by the coated samples was about half that of the uncoated ground magnesium, and nearly the same as that of the atomized magnesium. In some cases (e.g., Mechanofusion), the coated products fared better than the atomized magnesium for up to 60 hours of testing. While these results are still not highly quantitative, they show that our objective of developing a cost effective method to reduce moisture absorption of ground magnesium powder has been successfully achieved.

Another set of separate experiment was conducted to see the weight increase in the coated samples tested in the humidity chamber for 400 hours. The results are shown below from Figures 6.10-6.12.

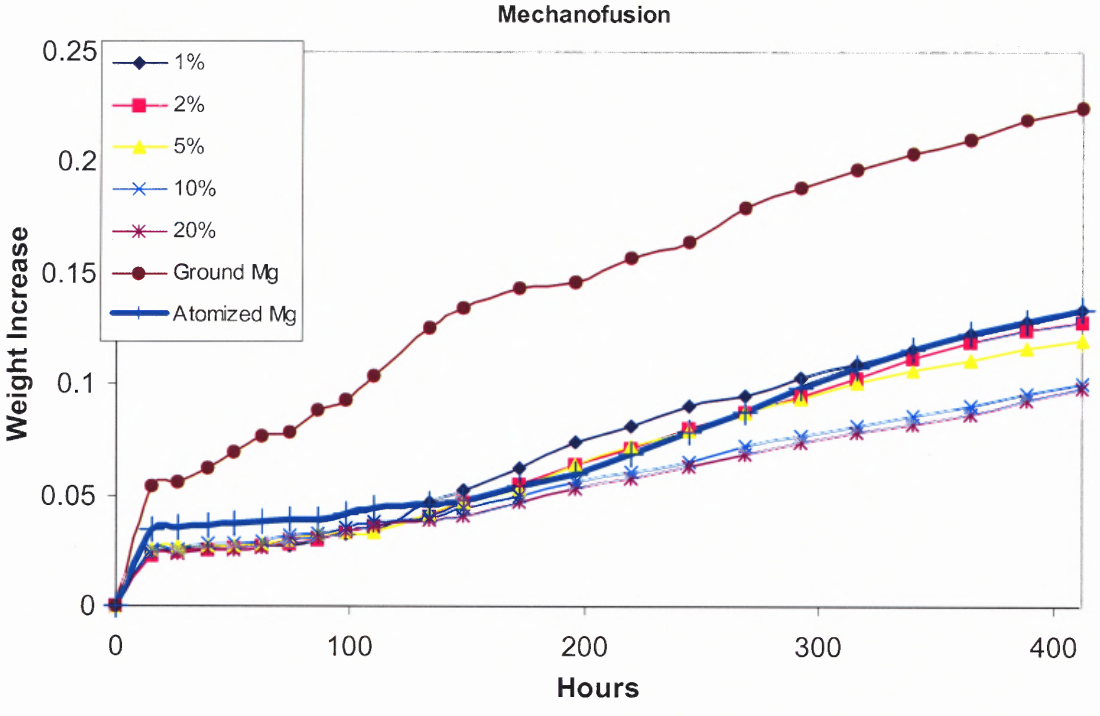

Figure 6.10 Humidity test for samples coated in the Mechanofusion system.

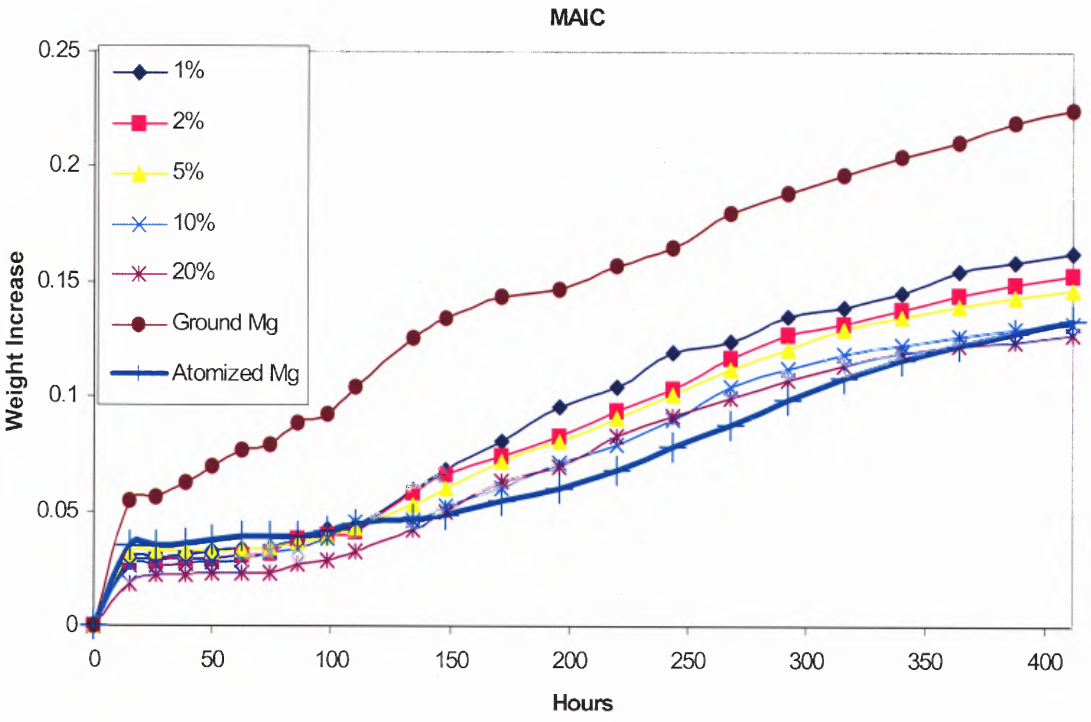

Figure 6.11 Humidity test for samples coated in the MAIC system.

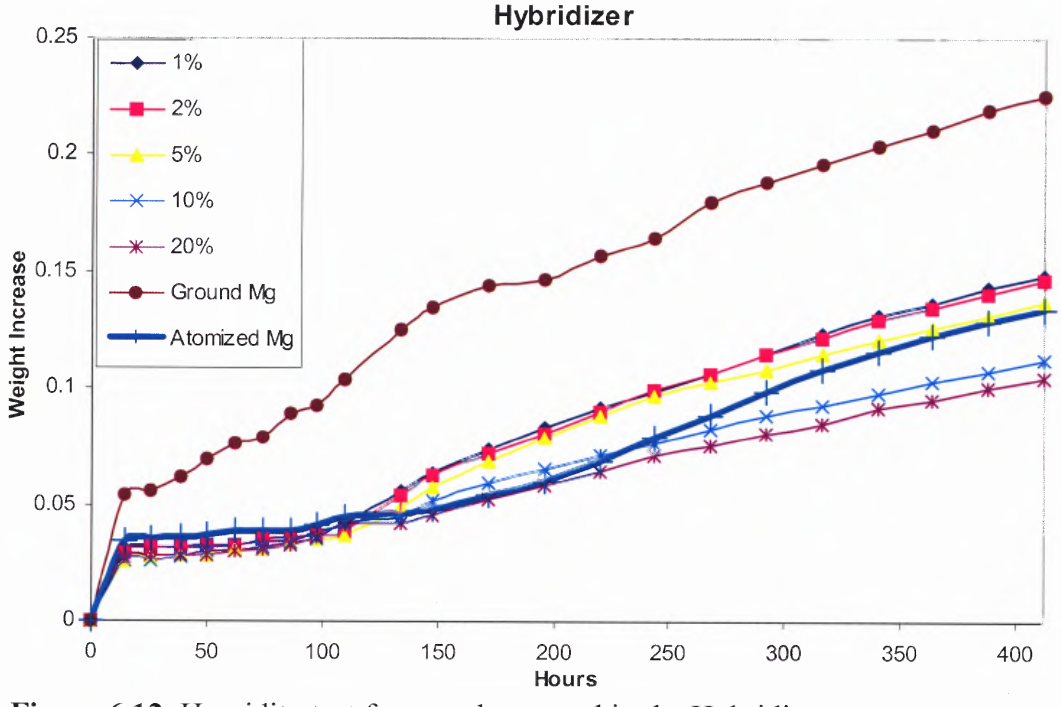

Figure 6.12 Humidity test for samples coated in the Hybridizer system.

As seen from Figures 6.10-6.12, the coated samples seemed to be performing better than atomized magnesium until 100 hours after which the moisture absorption rate in the coated samples was seen to be higher than the atomized magnesium. At the end of 400 hours, all the coated samples processed in the Mechanofusion system seemed to be performing better than atomized magnesium, while only 10% and 20% samples were better than atomized magnesium for the samples processed in the MAIC and Hybridizer system. Clearly, the Mechanofusion system was seen to be a better choice for coating ground magnesium.

6.3.5 XRD

In addition to the humidity test, a more quantitative technique, X-ray diffraction, was used to characterize the hydroxide formation on the surface of the magnesium powder in order to get further insight into the process. The results for samples exposed to humidity over 400 hours are shown in Figure 6.13. One representative sample using 5% wax from each processing device was taken. The sample processed in MAIC was for 10 minutes using a magnets to particles ratio of 3:1 by weight. The Mechanofusion sample was processed at 1000 rpm for 10 minutes and the Hybridizer sample was processed for 2 minutes at 5000 rpm. The samples were scanned from 15° to 75°. The major α-magnesium peak was seen at 34°-36°, whereas, the major α-magnesium hydroxide peaks were around 18° and 39°.

The XRD scans show that the uncoated ground magnesium was transformed into much more magnesium hydroxide at the surface than either the coated or atomized magnesium samples. For clarity, the region between 17° and 20° is highlighted and shown in Figure 6.14a for samples of 150 hours exposure time. As shown, the uncoated

ground magnesium sample had the highest concentration of hydroxide on its surface as compared to the coated as well as the atomized samples. The atomized magnesium sample appeared to have the least hydroxide formation, and there was no significant difference in the patterns of hydroxide in the coated samples processed in different devices. The results of coated samples exposed to more than 400 hours are shown in Figure 6.14b. The absorbed moisture was higher as compared to the 150 hours test. Still the ground magnesium had the highest hydroxide content as compared to the other samples. As a matter of fact, it turned into white powder at the end of this prolonged humidity test while the other coated samples retained their original dark black color. It should be noted that at this prolonged humidity test, the coated products outperformed the atomized magnesium as their hydroxide peaks were seen to be lower than that of the atomized magnesium. XRD analysis was also carried out for 10% and 20% wax coated samples, exposed to humidity for 150 hours, and the results are shown in Figures 6.14c and 6.14d. There is no significant difference in the intensity counts of hydroxide formation on 10% and 20% wax coated samples as compared to the 5% sample. The results imply that the lower wax loading is enough to obtain excellent hydration resistance. It should be noted that the samples processed in Mechanofusion showed the least amount of water absorption for 10% and 20% wax, the same trend reported in the humidity tests for samples processed by Mechanofusion using much less wax, indicating that better distribution and softening of wax during the coating process does enhance moisture resistance.

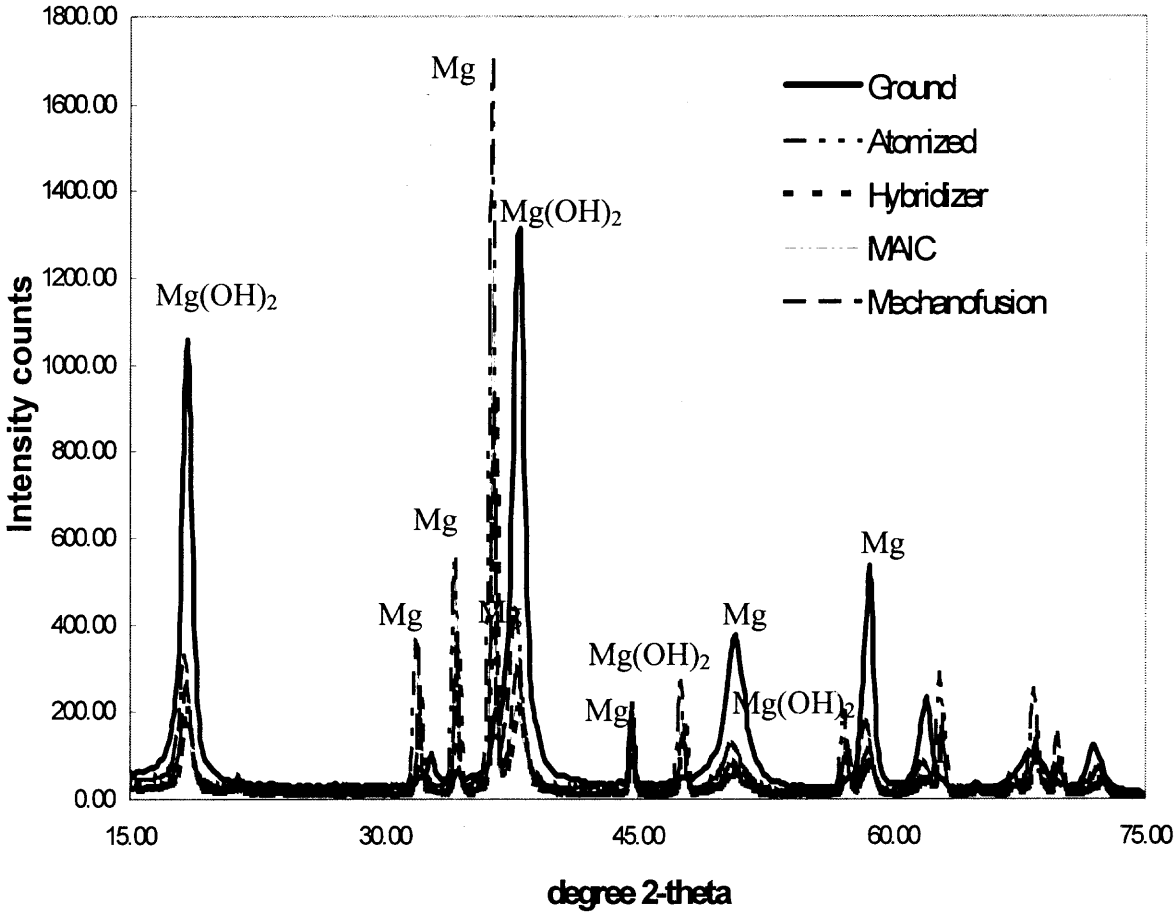

Figure 6.13 Typical XRD pattern for ground magnesium, atomized magnesium and samples processed in different systems.

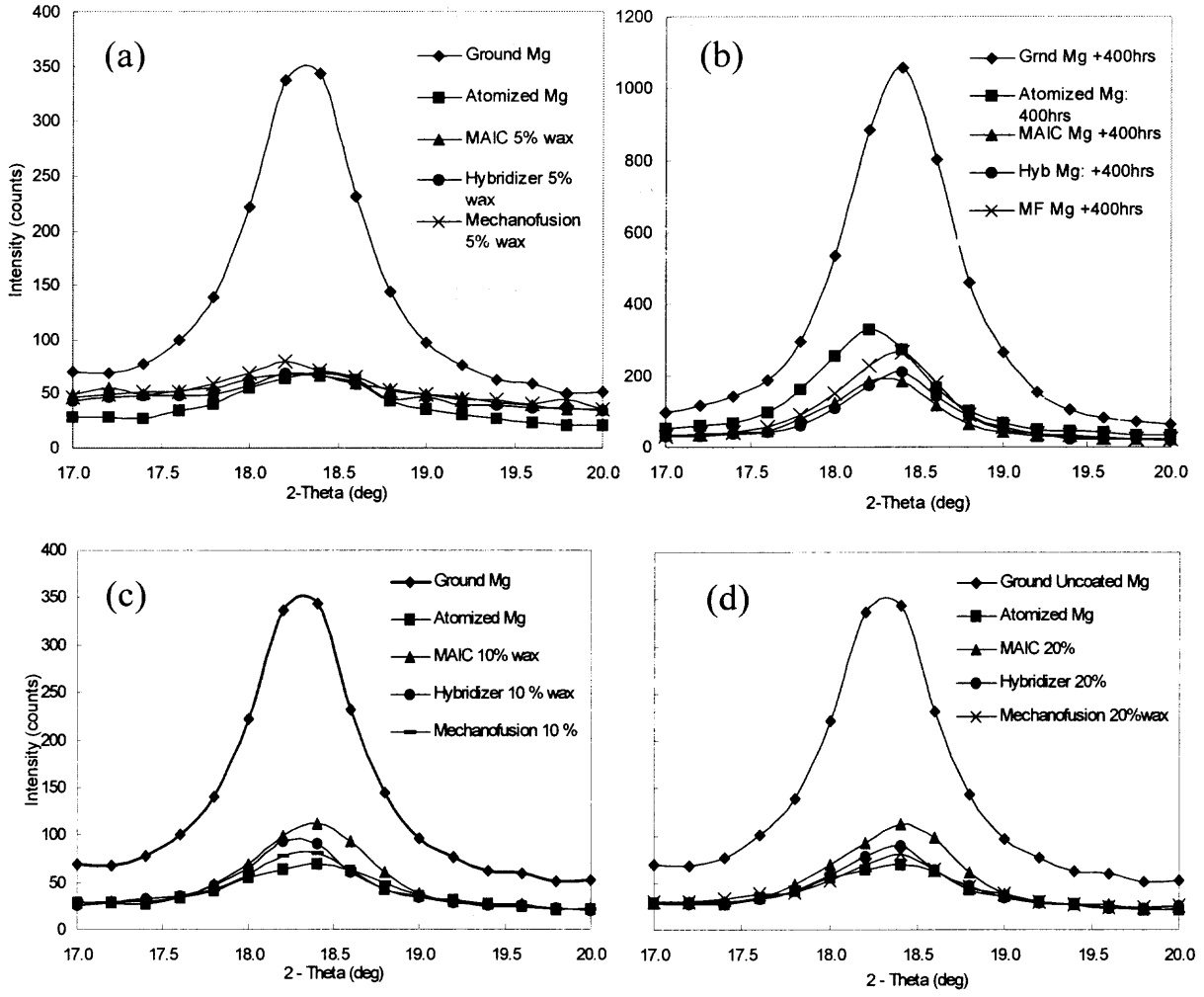

Figure 6.14 XRD for magnesium hydroxide peaks for coated and uncoated magnesium (a) exposed for 150 hours (b) exposed for 400 hours (c) coated with 10% wax (d) coated with 20% wax.

6.4. Summary

In this study, a cost-effective, environmentally benign method has been developed which improves the moisture resistance of ground magnesium to a level comparable to, or even better than that of uncoated atomized magnesium. This was accomplished using various dry particle coating methods to coat ground magnesium powder with carnuba wax or fumed silica. Carnuba wax was found to be a superior coating material as compared to fumed silica. The wax coated magnesium samples were tested (fired) at Picatinny Arsenal and the coating showed no adverse effect on their pyrotechnic properties.

Immersing the uncoated and coated samples into water demonstrated that hydrophilic magnesium can be transformed into a much more hydrophobic product by coating a layer of wax onto the magnesium surface. The humidity tests showed that the product's humidity resistance increased significantly even with only 1-2% by weight of wax. The improved humidity resistance was further verified through XRD tests, which showed that hydroxide formation on the surface of magnesium was significantly less in the coated samples as compared to the uncoated one, and was similar to that of atomized magnesium in the 150-hour (accelerated test) runs. In the extended 400-hours runs, the wax coated samples actually performed better than the atomized magnesium.

The particles processed in the different coating systems were smoothed and rounded, as compared to the uncoated product. Wax was softened and spread over the magnesium surface for the Mechanofusion and Hybridizer samples, but the wax particles remained discretely distributed over the surface of the MAIC samples. Better distribution and softening of wax yielded better moisture resistance. Nevertheless, the different devices used for dry coating of ground magnesium and their different operating

conditions did not make a significant difference in the humidity tests of the coated samples, as long as the system temperature was close to the melting point of wax. Thus, it has been clearly demonstrated that dry coating techniques can be used to improve the moisture resistance, and hence, the shelf life of ground magnesium powders.

CHAPTER 7

NUMERICAL STUDY OF OSCILLATING PARTICULATE SYSTEM USING DISCRETE ELEMENT METHOD (DEM)

In this work, the well-known Cundall-Strack (1979) discrete element simulation is employed to investigate the flow characteristics of unary and binary particulate beds in oscillating sectorial containers. The simulated flow characteristics of both unary and binary granular beds have similarities with those of particulate beds subjected to combined vertical and horizontal vibrations in that the granular bed heaps toward one of the container walls. However, for a given frequency, heaping in an oscillating container shifts alternately from one radial wall to another during an oscillation cycle. It is found that there is a critical frequency at which heaping becomes symmetrical and that the asymmetric heaping patterns at frequencies below and above the critical frequency are just opposite to each other. In a binary particulate bed, with initially separate layers of two different size particles, the movement of particles from one layer to another remains small at frequencies of oscillation below the critical frequency. However, the binary particulate bed seems to get well mixed at oscillation frequencies above the critical frequency. Mixing rate constant is calculated for binary system to analyze the mixing of granular system quantitatively and compared for the wide range of operating frequencies of the oscillating container.

7.1 Introduction

The particulate system inside the chamber is multidisperse in which a set of host particles is coated/mixed with the guest particles. In order to understand the flow characteristics of

the particles inside the coating/mixing chamber, two-dimensional simulation studies of granular flows in oscillating, a sectorial container was carried out. Both unary and binary particulate systems were considered. In what follows herein, the geometry of the container, the contact model of interacting particles, and the mathematical equations used for simulation are described. Next, the results of simulation studies are presented and discussed. The conclusions of the investigations are included in the last section of the chapter.

7.2 Simulation Method

The sectorial container of interest is shown in Figure 7.1. The container is subjected to harmonic angular oscillations of the form

$$\theta = \theta_0 \sin(2\pi ft + \Phi) \tag{7.1}$$

where f is the frequency of oscillations, t is the time, the θ is the amplitude, and Φ is the phase angle.

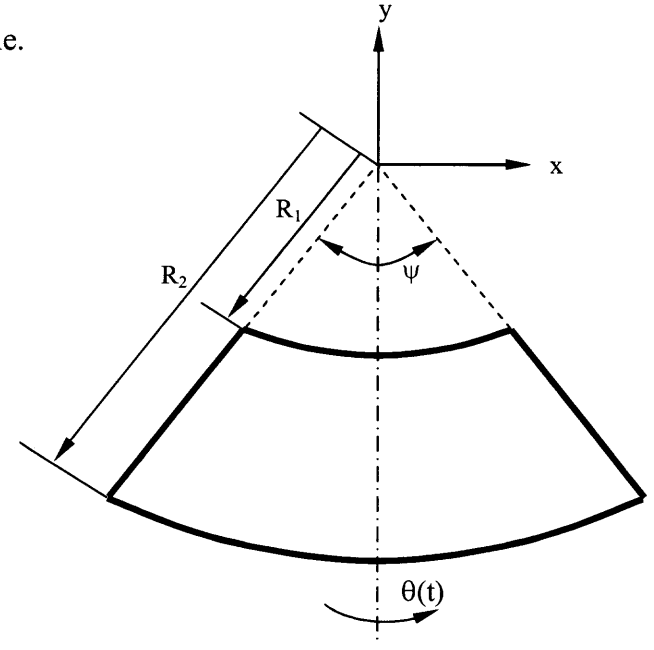

Figure 7.1 Oscillating sectorial container.

The container is filled partially with a set of non-cohesive, spherical particles. The motion of the granular material inside the container is confined in the transverse xy-plane only with each particle having two degrees of translational and one degree of rotational motion. The motion of particles inside the container is delineated using two-dimensional, discrete element method (DEM) of Cundall and Strack (1979). Simulation involves the solution of the Newton's equations of motion of each individual particle taking into account the various body and interaction forces acting on the particles. The model used in the present simulations includes force of gravitation as the only body force, and the interaction forces are the ones that come into play due to collision between the particles. Accordingly, the equations of motion of an i^{th} particle may be written as

$$m_i \ddot{x}_i = \sum_{j \neq i}^{n_i} \left[\left(F_{nij} \right)_x + \left(F_{sij} \right)_x \right] \tag{7.2}$$

$$m_i \ddot{y}_i = \sum_{j \neq i}^{n_i} \left[\left(F_{nij} \right)_y + \left(F_{sij} \right)_y \right] - m_i g \tag{7.3}$$

$$I_i \ddot{\theta}_i = \sum_{j \neq i}^{n_i} \left(r_i F_{sij} \right) \tag{7.4}$$

where n_i is the instantaneous number of particles, including the solid boundaries (walls), in contact with the i-th particle. Note that n_i does not include the i-th particle itself. Also $n_i < N$, the total number of particles in the container. In Equations (7.2)-(7.4), m_i is the mass, I_i is the rotational moment of inertia, r_i is the radius, (x_i, y_i) are the position coordinates with respect to the Cartesian axes (Figure 7.1), and θ_i is the angular rotation of the i-th particle. F_{nij} and F_{sij} are, respectively, the normal (radial) and tangential (shear) components of the contact force exerted by the j-th particle on the i-th particle. The n-

direction is along the outward normal at the point of contact on the particle i, i.e., along the line of centers from i to j. The direction s is along the common tangent at the point of contact such that n-s directions make right-handed pair of axes. Subscripts x and y indicate components along the x and y axes, respectively, and overdots denote time derivatives.

Figure 7.2 shows a contact model, proposed originally by Cundall and Strack (1979), that have been used extensively (with some variations, e.g., including a linear dashpot for tangential contact as well Tsuji et al. (2000) in granular flow simulations. The same model is employed for the present simulation studies.

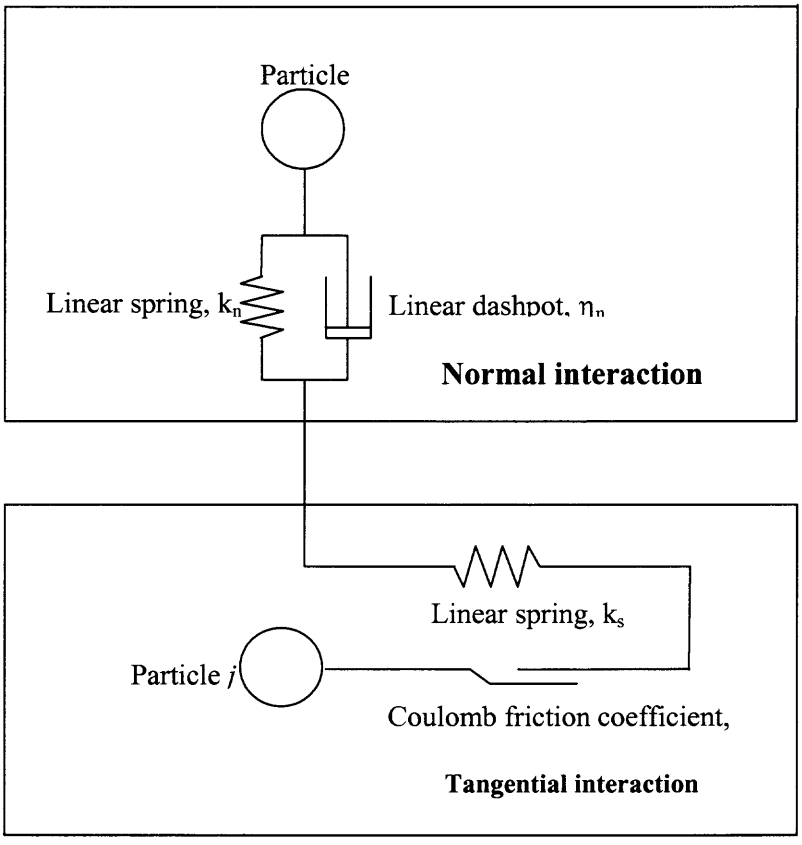

Figure 7.2 Interaction model of two contacting particles.

Based on this model, using the symbols defined in Figure 7.2, the normal contact force is determined by the linear spring (k_n) and dashpot (η_n) elements:

$$F_{nij} = -k_n \delta_{nij} - \eta_n \left(v_{ni} - v_{nj} \right) \tag{7.5}$$

where δ_{nij} is the total displacement of the particles i and j in the direction of the common normal (along the lines of centers), and is given by

$$\delta_{nij} = r_i + r_j - \sqrt{\left(x_i - x_j \right)^2 + \left(y_i - y_j \right)^2} \tag{7.6}$$

and v_{ni} and v_{nj} are components of particles' velocities along the common normal. The tangential contact force is determined by either the linear spring element k_s or the Coulomb friction element μ_s; it is given by

$$F_{sij} = \begin{cases} -k_s \delta_{sij} & if \quad k_s \left| \delta_{sij} \right| < \mu_s \left| F_{nij} \right| \quad otherwise \\ sign \left(-k_s \delta_{sij} \right) \mu_s F_{nij} \end{cases} \tag{7.7}$$

where δ_{sij} is the relative tangential displacement between the particles. The above equation implies that the tangential force of interaction is determined by the tangential spring force as long as its magnitude is less than the limiting friction force. However, as soon as the magnitude of tangential spring force reaches the limiting friction force value, tangential deformation stops, and frictional sliding sets in between the particles. In the above equation, sign ($-k_s \delta_{sij}$) is the sign of the tangential spring force just before the initiation of sliding. The equations for the constants of spring and dashpot elements are given in the Appendix C; these are adopted from Wassgren (1997), and are included here for a ready reference.

7.3 Results and Discussion

In this section, the results of discrete-element simulation studies based on the model of the foregoing section are presented. The data needed for simulation are related to the geometry of container (R_1, R_2, ψ), the size and number of particles, the model parameters (k_n, η_n, k_s, μ_s), and the operating condition (f, θ_0). In view of the highly time consuming computations and a rather large number of data variables of the problem, the simulation studies were aimed to bring out the basic features of granular flow in oscillating containers. For this reason, it was deemed fit to investigate the effect of frequency of oscillations for a set of fixed valuess of all other data variables Two types of particulate beds, namely, one with unary set of uniform size particles, and the other with binary set of two types of uniform size particles of diameter ratio 1:2, were considered. The data used for simulation of the two types of particulate beds are given in Table 7.1. In all the results being presented herein, simulation was initiated with the following conditions of the container:

$$\theta = 0; \quad \dot{\theta} = 2\pi f\theta_0 \quad at \ t = 0 \tag{7.8}$$

i.e., giving an angular speed of $2\pi f\theta_0$ to the right from the vertical equilibrium position with a phase angle $\Phi = 0$. The particles were given initial random velocities with a distribution ±100 times (particle diameter) using a C++ pseudo-random number generator. The initial rotational velocities of the particles were taken as zero. In the following, first the results of simulation of unary particulate bed are presented. The results of unary particulate simulation are an extension of the work published in AIChE

Annual Meeting CD-ROM proceedings, 2000; see Mujumdar et al. (2000). The simulation results of binary particulate bed are presented next.

Table 7.1 Data for Simulation of Granular Bed in an Oscillating Sectorial Container

Sectorial Container	**Binary system**			**Unary system**		
Inner radius: R_1	15mm			10mm.		
Outer radius: R_2	60mm			30mm.		
Arc length: ψ	60 deg.			60 deg.		
Granular bed						
Nominal diameter	0.6 mm (small);1.2mm(large)			0.4mm		
Number of particles	1320(small); 198(large)			1399		
Contact model						
Type of interaction	$k_n = k_s$ (N/m)	η_n (Ns/m)	μ_s	$k_n = k_s$ (N/m)	η_n (Ns/m)	μ_s
Particle-particle	77.79 1556.0	0.0045 0.0090	0.5(small) 0.5(large)	230.5	0.0013	0.5
Particle-wall	6224.0 1245.0	0.0361 0.0723	0.5(small) 0.5(large)	461.0	0.0027	0.5
Operating conditions						
Amplitude of oscillations	45 deg.			30 deg.		
Frequency range	0.5 to 3 Hz			0.5 to 3 Hz		

7.3.1 Simulation of Unary Particulate System

Figures 7.3 (a) and (b) show two settings that were used for simulation of unary particulate bed. In Figure 7.3(a), the particles are set in a regular sector-shaped fashion. The symmetric heaped setting of Figure 7.3(b) is obtained from that of Figure 7.3(a) in which, keeping the container stationary, the particles are given random motion, and then allowed to settle down until the granular bed becomes almost static. The two settings were actually used in only a few simulation runs to see the effect of initial setting of the particulate bed. As expected, no noticeable differences could be found in the stabilized granular flow patterns ensuing from the two settings. However, for uniformity, all the results of unary simulations being presented here are the ones obtained from the setting of Figure 7.3(b).

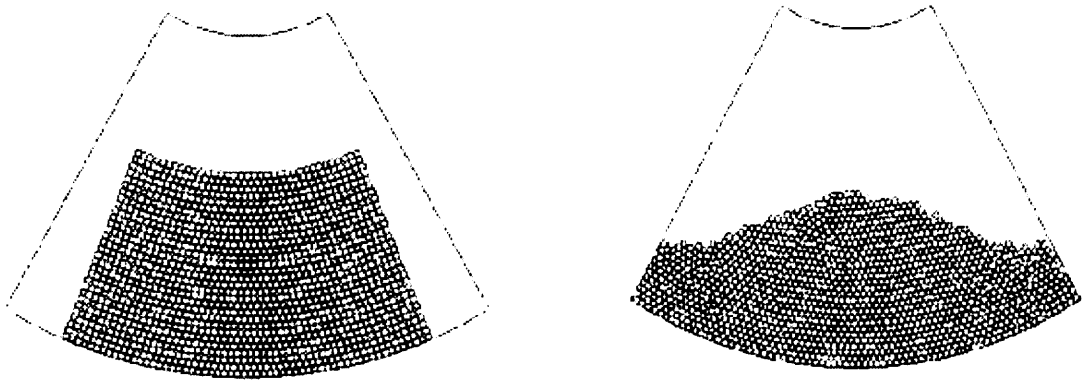

Figure 7.3 Setting of unary particulate bed before simulation.

Snapshots of the unary granular bed inside a sectorial container obtained at the end of twenty cycles of oscillations are shown in Figure 7.4 for a wide range of frequency of oscillation. Asymmetric heaping of the granules to one of the radial sidewalls of the

container is noticeable. In the lower frequency range, heaping first increases, as indicated by its height on the right side wall, up to a frequency of about f = 1.5 Hz, and then starts decreasing. Heaping starts increasing again, but now on the left side, when the container is subjected to frequencies f > 3 Hz, approximately. It may be seen in Figure 7.4 that the heaped beds are only slightly asymmetric to the right and left sides at oscillation frequencies of 2.5 Hz and 3 Hz, respectively.

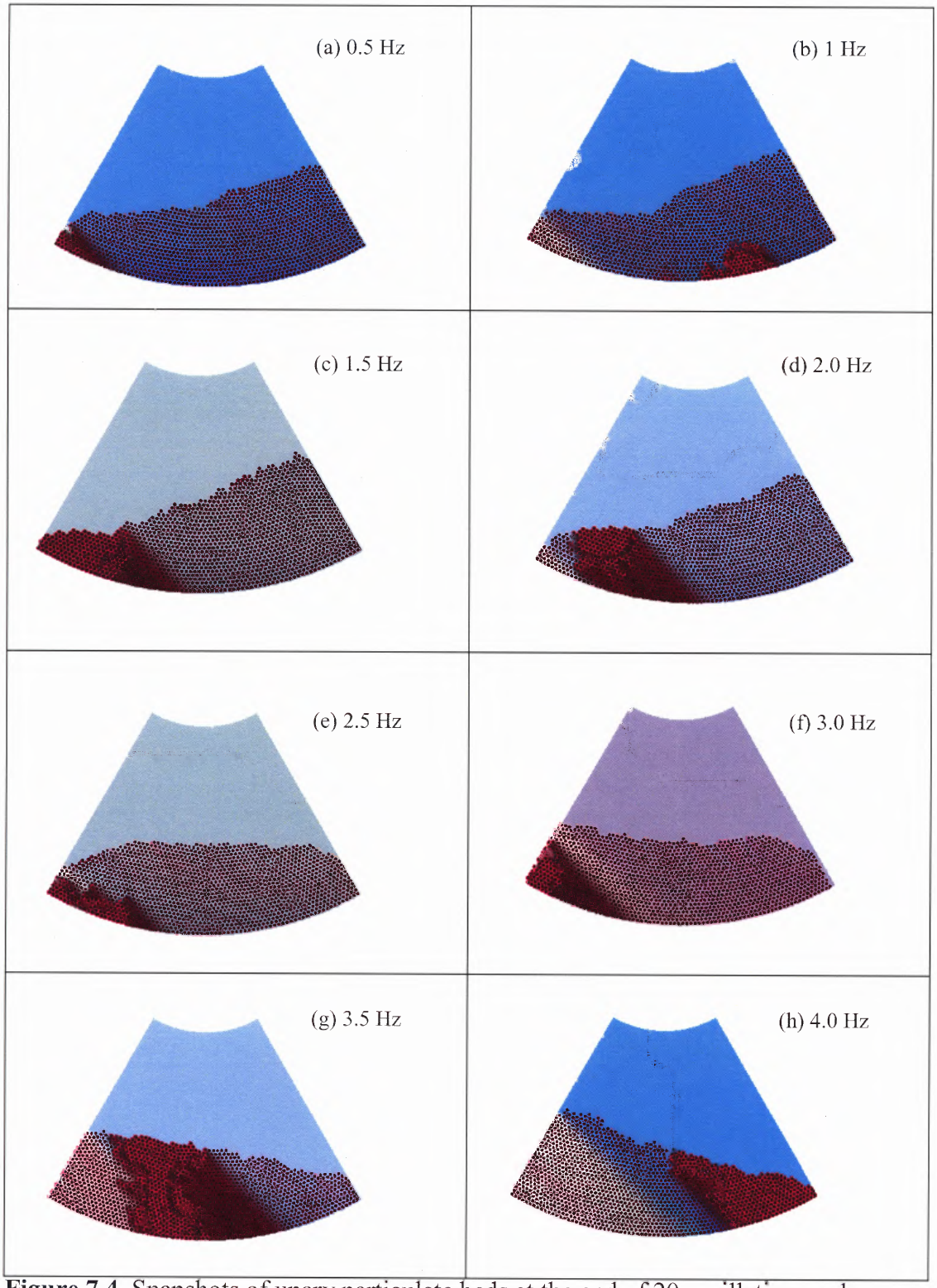

Figure 7.4 Snapshots of unary particulate beds at the end of 20 oscillation cycles for various oscillation frequencies.

There ought to be a critical frequency of oscillation f_{crit} of the container at which the granular bed would have a symmetric heaping pattern. By trials it was found that in a container oscillating at $f = f_{crit} = 2.6$ Hz, approximately, the granular bed actually forms a symmetric heap. Figure 7.5 illustrates how granular pattern changes during one cycle of oscillation. Here, granular flow snapshots in the twentieth cycle of oscillations at quarter cycle steps are shown for $f = 1.5$, 2.6, and 4.0 Hz. It may be noted that granular bed heaps alternately to the two sides of container every half cycle of oscillations, Figures 7.5(a) and 7.5(c). Also, for $f = 2.6$ Hz, which is the critical frequency of oscillation, the granular bed seems to retain its symmetrically heaped shape during the whole cycle of oscillation, Figure 7.5(b). Actually, it is observed in the graphic visualization that the unary bed becomes almost stagnant when the sectorial container oscillates at the critical frequency. Heaping of granular bed in oscillating container illustrated in Figures 7.4 and 7.5 is similar to the well known granular heaping phenomena in vertically-vibrated rectangular and wedge-shaped containers, which has been reported in many experimental studies; see, for instance, Wassgren et al. (1996) and the references sighted in that work.

Asymmetric heaping in these containers occurs possibly due to some angular misalignment between the axes of container and (vertical) vibration resulting in a horizontal component of vibration. In fact, the occurrence of heaping to be the result of combined vertical and horizontal vibrations has been shown by two-dimensional discrete element simulations as well, for both rectangular (Tsuji et al. 2000) and wedge-type containers (James et al. 2000, 2002). These containers do not change their orientation during vibration, and heaping stays in one direction, either to the left or to the right, only, depending on the direction of angular misalignment.

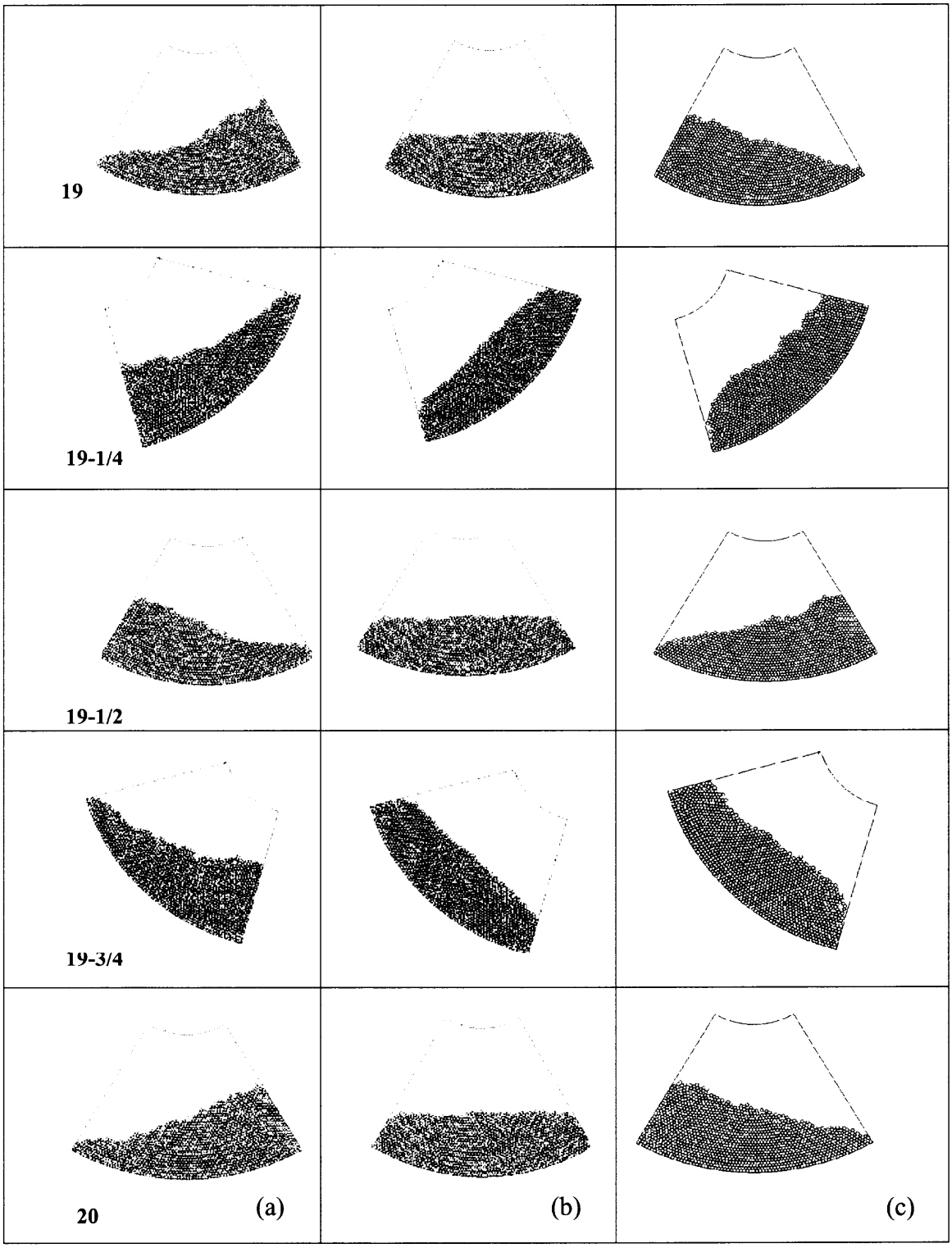

Figure7.5 Snapshots of unary particulate beds at quarter-cycle intervals in the 20th cycle of oscillation; the snapshot (b) is at critical frequency, and the snapshots (a) and (c) are at frequencies below and above the critical frequency.

In the present problem, a granular mass is subjected to both horizontal and vertical vibrations, and the orientation of the container changes every half-cycle. This accounts for asymmetric heaping with alternating orientation every half cycle.

A simple explanation of the heaping phenomena in an oscillating container is as follows. At low frequencies of oscillations, f < 2.6 Hz, as seen in Figure 7.5(a), the granular mass tends to accumulate near the bottom every quarter cycle due to dominant gravitational action. Consequently, the bed is seen to be heaping to the left and right sides after one-half and full cycles, respectively. At higher frequencies, f > 2.6 Hz, the centripetal force of the granular mass becomes dominant and, as seen in Figure 7.5(c), the heaping pattern is just reversed.

Figures 7.6 and 7.7 provide two additional sets of results. Figure 7.6 shows the loci of the center of mass ($\bar{x}, \bar{y}$) of granular mass in the initial first two and the last two cycles of 20-cycles simulation for f = 1.5, 2.6, and 4.0 Hz. As observed through the graphic visualization and snapshot, particulate motion stabilizes after two or three oscillation cycles. This is quite apparent from Figure 7.6 (and, as would be seen later, from Figure 7.7 as well). It may also be seen from Figure 7.6(b) that, for the case of critical frequency oscillations, the stabilized locus of the center of mass, is a circular arc (this is also checked from the actual numbers). This indicates, as pointed out earlier, the granular bed retains its symmetrically heaped shape during the container oscillations.

Figure 7.7 shows the variation of unit kinetic energy fluctuation $\Delta\bar{e}$ with time for f = 1.0, 2.5, and 4.0 Hz. The unit translational kinetic energy fluctuation is defined as

$$\Delta e = \frac{1}{2m}\sum_{i=1}^{N} m_i\left[\left(xi - \bar{\dot{x}}_i\right)^2 + \left(yi - \bar{\dot{y}}_i\right)^2\right] + \frac{1}{2I}\sum_{i=1}^{N} I_i\left(\theta i - \bar{\dot{\theta}}_i\right)^2 \qquad (7.9)$$

where $m = \sum_{i=1}^{N} m_i$ and $I = \sum_{i=1}^{N} I_i$ are the total mass and mass moment of inertia of the particulate bed, and

$$\bar{\dot{x}} = \frac{1}{2m}\sum_{i=1}^{N} m_i \dot{x}_i \; ; \quad \bar{\dot{y}} = \frac{1}{2m}\sum_{i=1}^{N} m_i \dot{y}_i \; ; \quad \bar{\dot{\theta}}_i = \frac{1}{2I}\sum_{i=1}^{N} \theta_i \dot{\theta}_i \tag{7.10}$$

are the velocity components of the center of mass of the particulate bed. In Figure 7.7, cyclic variations of fluctuating energy for f = 1.0 and 4.0 Hz are noticeable. The fluctuating energy is maximum every half-cycle when the container is close to the vertical position ($\theta = \pi, 2\pi$, where $\dot{\theta} = \pm 2\pi f \theta_0$). This is expected since every half cycle, the particulate bed changes its (heaped) orientation quickly as the container begins moving either to the left or to the right from the vertical position. Likewise, the energy fluctuations are minimum when the container is close to the either ends ($\theta = \pi/2, 3\pi/2$ where $\dot{\theta} = 0$}. It may further be seen that, for the case of critical frequency oscillations, the cyclic variation of fluctuating energy remains almost uniform with the simulation time.

7.3.2 Simulation of Binary Particulate System

As mentioned earlier, the data used for simulation of binary particulate system is given in Table 7.1. The initial setting of a binary set of particles is shown in Figure 7.8. As shown, the layers of small particles are set over the layers of large particles. In the present case, there are four layers of the large particles and fifteen layers of small particles.

Simulation snapshots of the binary particulate bed for various frequencies of oscillations are shown in Figure 7.9; each of these snapshots is taken at the end of twenty oscillation cycles. Comparing these snapshots with those of unary particulate system in

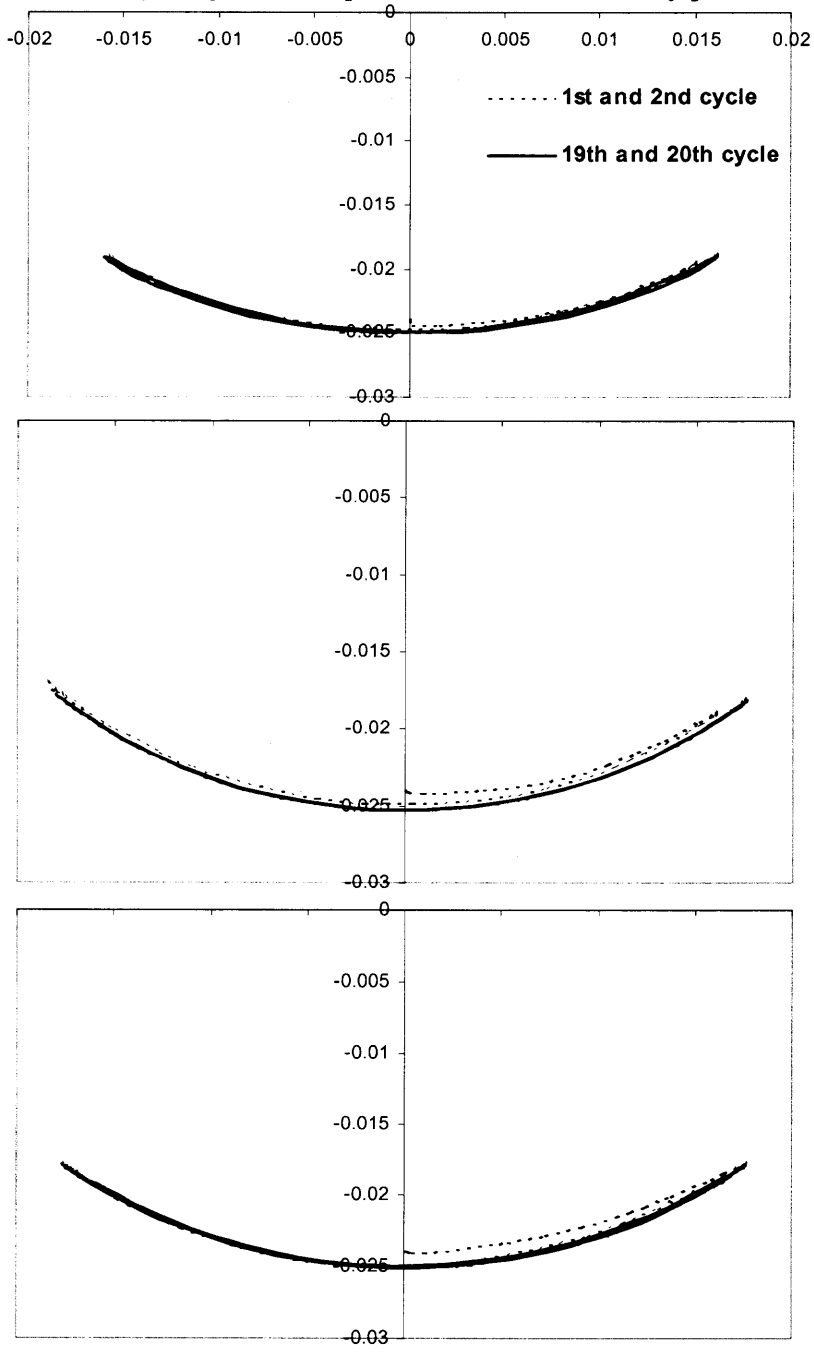

Figure 7.6 Loci of the mass center of oscillating unary particulate bed at frequencies below, equal, and above the critical frequency during first and last two oscillation cycles of 20-cycle simulations.

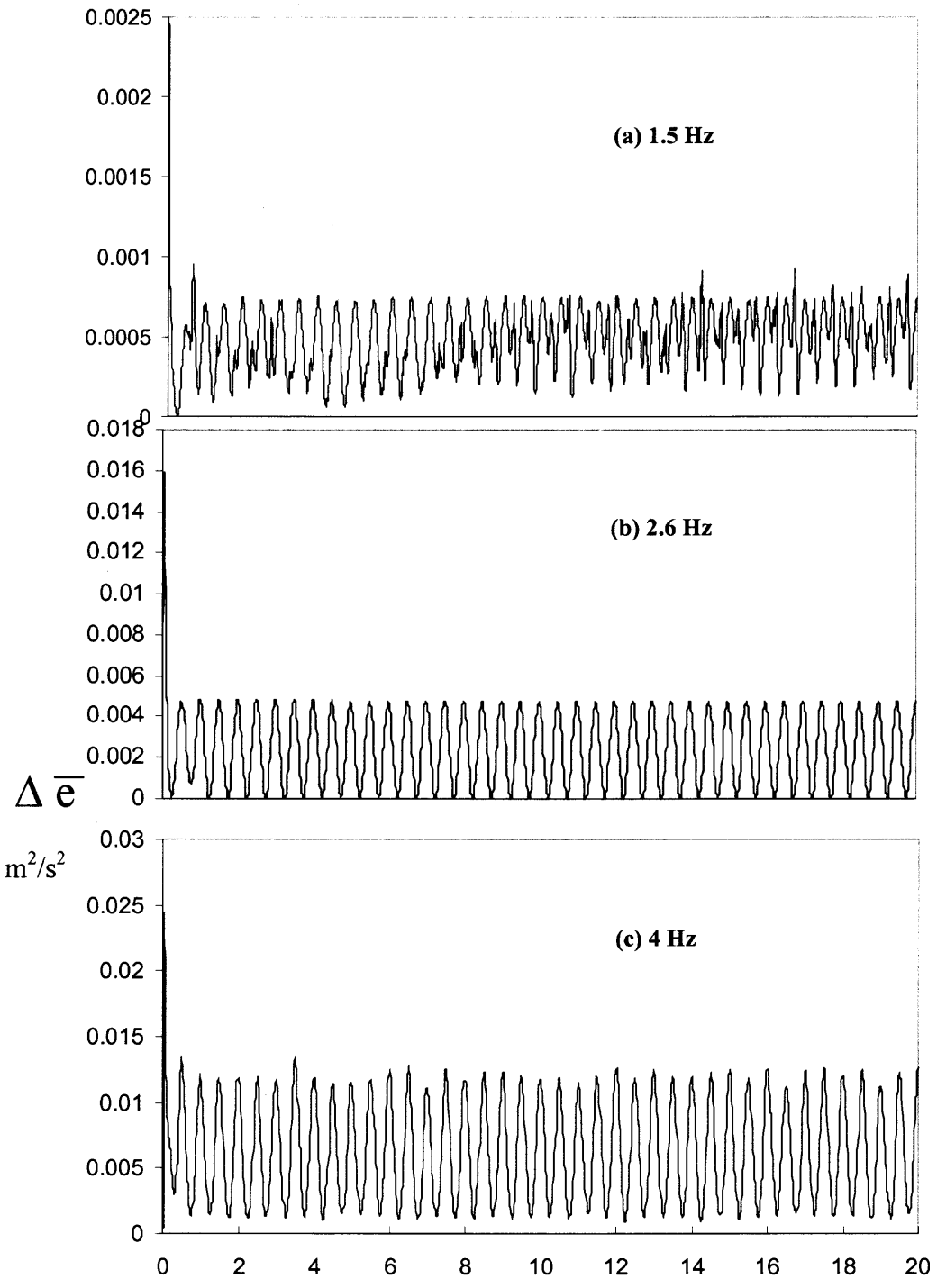

Figure 7.7 Variation of unit fluctuation energy of unary particulate bed at frequencies below, equal, and above the critical frequency during first and last two oscillation cycles of 20-cycle simulations.

Figure 7.4, occurrence of heaping and its right-to-left reversal pattern are immediately apparent. Thus, it may be seen that in the low frequency range, heaping on the right wall increases, as indicated by its height, up to about f = 1 Hz, and then starts decreasing. However, at higher frequencies of oscillation, heaping begins to increase, but is shifted to the left side.

Figure 7.8 Setting of binary particulate bed before simulation.

It was found by trials that the critical frequency for the binary bed under consideration was f_{crit} = 1.7 Hz, at which the binary bed develops symmetrical heap. Figure 7.10 shows the snapshots of the binary bed at quarter-cycle steps in the twentieth cycle of oscillations for f = 1, 1.7 and 3.0 Hz. These snapshots are of course similar to those of Figure 7.5 for the unary bed in that the heaping alternates from one side to another every half cycle. Also, in a container oscillating at f = f_{crit} = 1.7 Hz, the symmetric shape of the bed is maintained during the complete cycle of oscillation. Similar to the case of unary bed, the graphic visualization shows that the particles in a binary bed appear to be almost stagnant, and that there is no exchange of particles between the two layers.

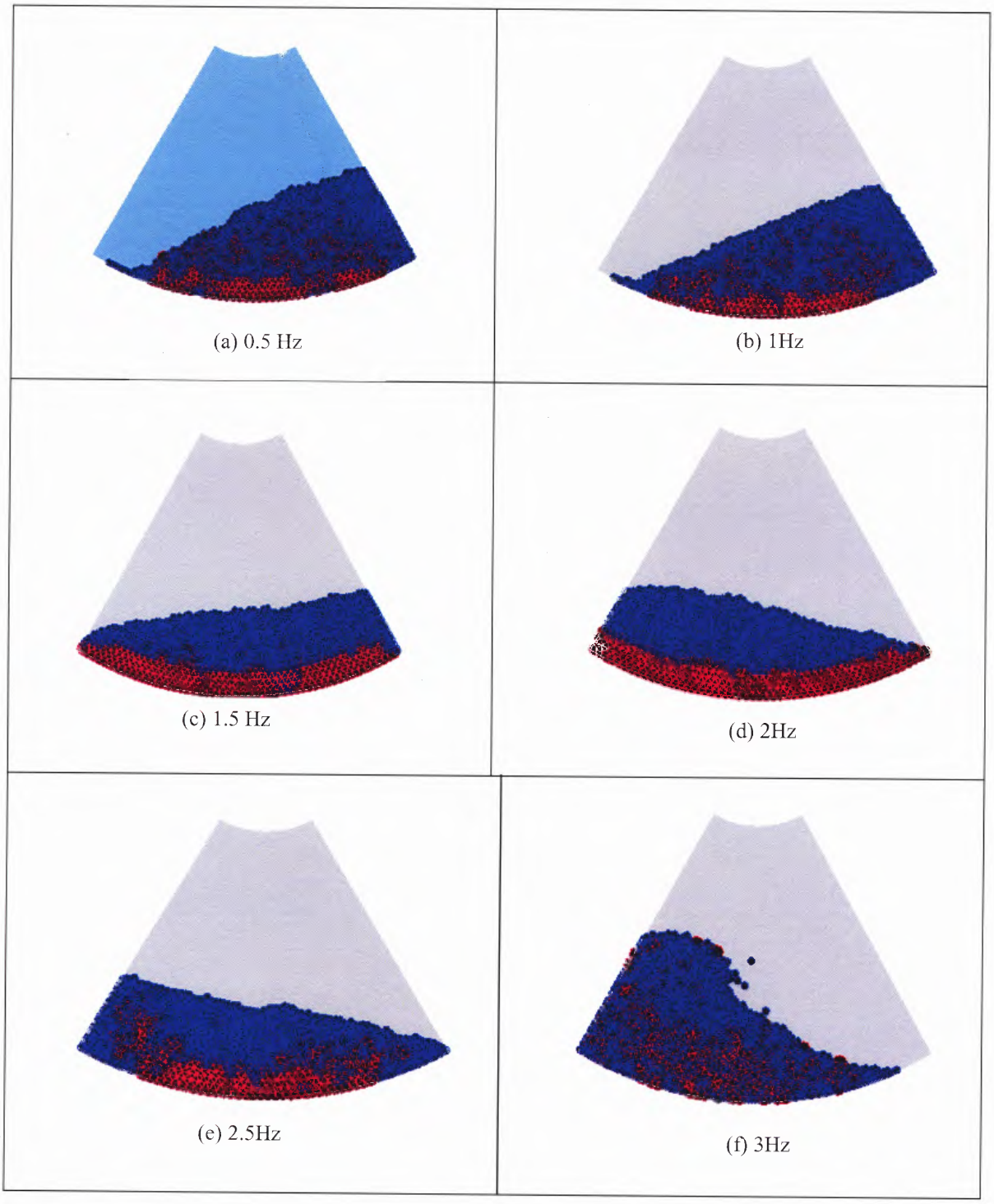

Figure 7.9 Snapshots of binary particulate beds at the end of 20 oscillation cycles for various oscillation frequencies.

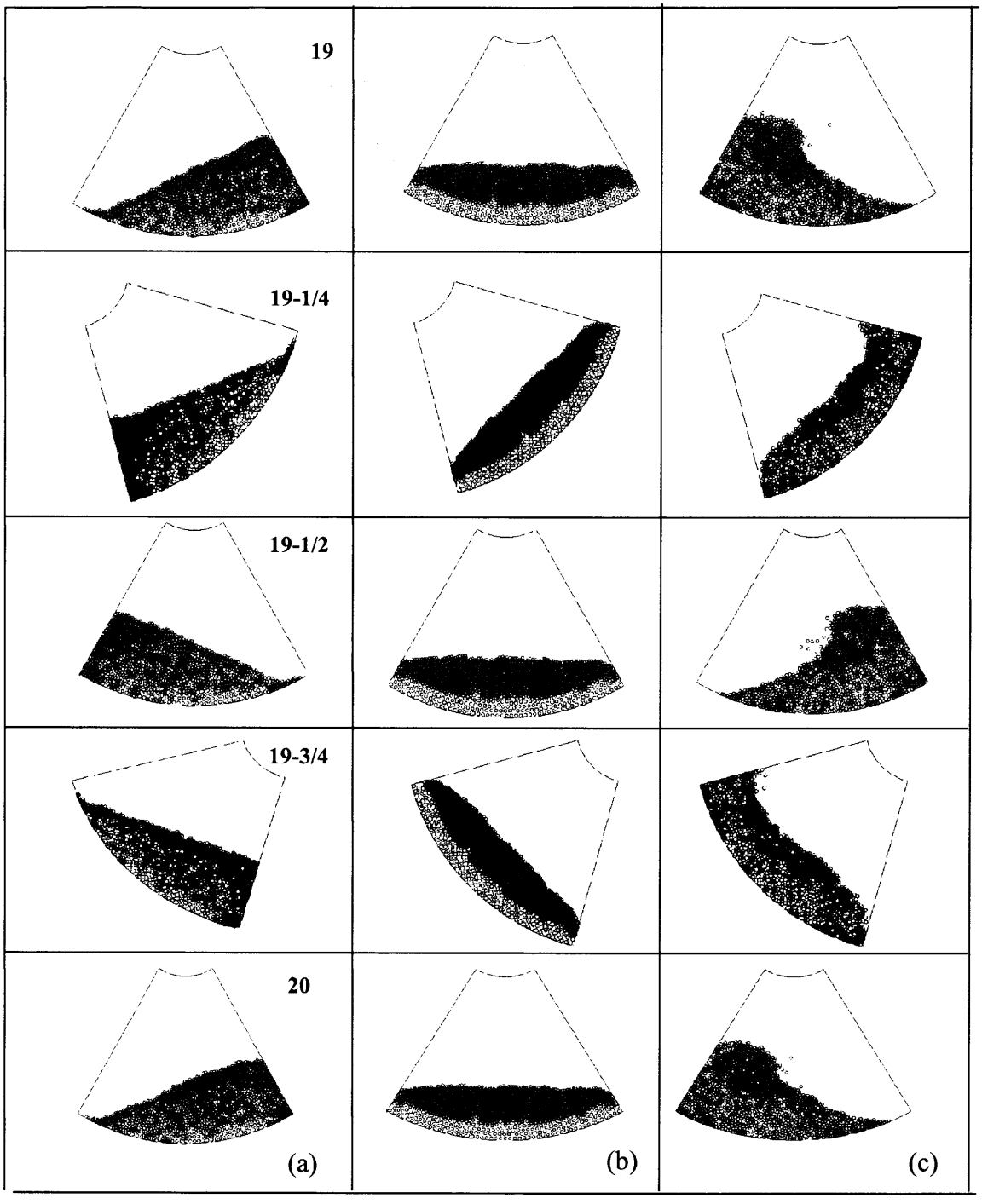

Figure 7.10 Snapshots of binary particulate beds at quarter-cycle intervals in the 20th cycle of oscillation; the snapshot (b) is at critical frequency, and the snapshots (a) and (c) are at frequencies below and above the critical frequency.

Figures 7.9 and 7.10 further reveal some interesting features of interaction of the two sets of particulates in three distinct frequency ranges. In a low frequency range of 0<f< 1 approximately, the small particles penetrate from the sides and the large particles disperse radially upward; see Figures 7.9(a) and 7.9(b). However, the two types of particles remain visibly separate with no signs of mixing even if simulation is continued beyond twenty cycles. Next, as shown in Figures 7.9(c), 7.10(b), and 7.9(d), in a moderate frequency range of $1 < f < 2$ approximately, the two layers remain separate with little exchange of particles between the two layers. At frequencies of oscillation $f > 2$ Hz, particulate motion becomes intense beginning with penetration of small particles from the walls into the lower layer and radially upward dispersion of large particles; see Figures 7.9(e) and (f). As the number of simulation cycles is increased, the particulate motion becomes increasingly intense, and after some time, the binary particulate body seems to become a well-mixed mixture.

The mixing characteristics of the binary set of particles may also be understood quantitatively. For this purpose the sectorial container is divided into cells of radial and mid-arc lengths each equal to αd_0, approximately (Figure 7.10), where $\alpha \geq 1$ is a size factor and d_0 is a nominal length defined as

$$d_0 = \sqrt[3]{\frac{N_1 d_1^{\,3} + N_2 d_2^{\,3}}{N_1 + N_2}} \tag{7.11}$$

where d and N, with subscripts, are the number and diameter respectively, of the two types of particles. During the course of simulations, the number of either type of particles is counted in each of the cells at the end of each discrete time interval used for time

marching in the solution of Equations (7.2)-(7.4). Then the concentration $\sigma_i^{(c)}$ of either type of particles in a cell c at the end of a discrete time interval may be calculated as

$$\sigma_i^{(c)} = \frac{N_i^{(c)}}{N_1^{(c)} + N_2^{(c)}} \quad i = 1,2 \tag{7.12}$$

where $N_i^{(c)}$ is the number of type i particles in the cell. The mean concentration $\bar{\sigma}_i$ of either type of particles in the entire particulate mass is then obtained as

$$\bar{\sigma}_i = \frac{\sum \sigma^{(c)}}{N_c} \quad i = 1,2 \tag{7.13}$$

where N_c is the number of non-empty cells. Also, the standard deviation of concentration $\bar{\bar{\sigma}}_i$ of either type of particles is obtained as

$$\bar{\bar{\sigma}}_i = \sqrt{\frac{\sum_{c=1}^{N_c} \left(\sigma_i^{(c)} - \bar{\sigma}\right)^2}{N_c - 1}} \quad i = 1,2 \tag{7.14}$$

The mean concentration and its deviation, $\bar{\sigma}_2$ and $\bar{\bar{\sigma}}_2$, for the large-size particles, based on particles count in cells of size factor α = 5, are plotted against simulation time in Figure 12. From the number of small and large particles given in Table 2, the gross concentration of the large-size particles is $\bar{\sigma}_2$= 198/(198+1320) = 0.13. Thus, in an oscillating sectorial container, as the binary agglomerate becomes more and more homogeneous with time, the concentrations of the large and small size particles should approach the values of 0.13 and 0.87, respectively.

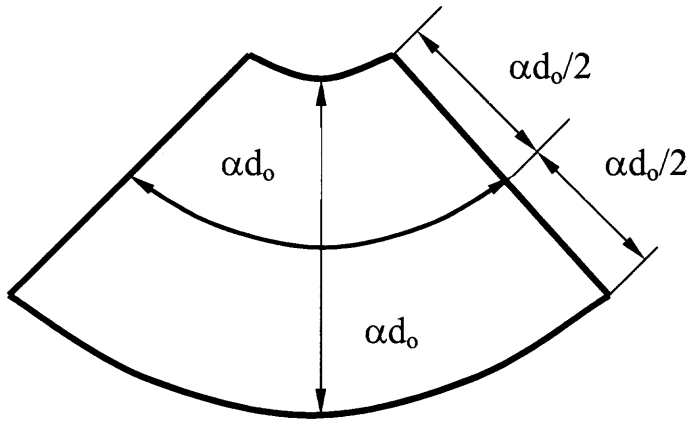

Figure 7.11 A cell used for determining concentration of two types of particles of binary bed during oscillations.

The mean concentration for various frequencies is in agreement with the granular flow patterns of Figure 7.9 discussed earlier. Constant values of mean concentration and standard deviation for f = 1.7 Hz indicate the state in which there is no movement of particles from one layer to another. It may further be seen that in a container oscillating at f = 3 Hz, the mean concentration $\overline{\sigma}_2$ of large particles approaches to $\sigma_2 = 0.13$ and the standard deviation $\overline{\overline{\sigma}}_2$ becomes smaller with increasing simulation time.

Khakhar et al. (1997) studied granular mixing problems in rotating cylinders experimentally and using continuum model and plotted the intensity of segregation against the number of revolutions, where the intensity of segregation is the same as mean concentration used in the present work. It was observed that the intensity of segregation has exponential decay in the initial stages and becomes constant at long times. Figure

7.12 shows basically the same characteristics of the binary bed in an oscillating sectorial container. Following Khakhar et al. (1997), an equation of the form

$$\overline{\sigma}_2 = \overline{\sigma}_{2,o} e^{-\lambda t / f} \tag{7.15}$$

is used for least squaring on the data of Figure 7.12. In the above equation, λ of units' cycles per sec is the mixing rate constant [Khakhar et al. (1997)]. The simulated results (reproduced from Figure 7.12) and fitted curves for three oscillation frequencies are shown in Figure 7.13. As may be seen from Figure 7.13, least squaring fitting is done for the first cycles as well as the twenty cycles. The constant λ from the 5-cycles fitting gives a measure of the initial rate of mixing, and the one from 20-cycles fitting of long time rate of mixing.

It may be noted that in Figure 7.15 one of the frequencies is the critical frequency (1.7 Hz), and very small value of mixing rate constant for this frequency is expected. In fact for an exact value of the critical frequency, the long time mixing rate constant ought to be zero. As the critical frequency is determined by trials, its value of 1.7 Hz cannot be expected to be an exact value. Of the two other frequencies in Figure 7.15, the initial mixing rate constant for 3 Hz frequency is higher that for 1 Hz frequency. This indicates that mixing of the two types of particles is more intense for 3 Hz than that for the 1Hz frequency; this is actually observed in graphic visualizations as well. The long time mixing rate constants for both the frequencies are nearly the same, however. The time taken for a well-mixed binary mixture depends on the initial rate of mixing; this is easily

seen from Figure 7.12 in which the $\overline{\sigma_2}$ seems to be reaching the 0.13 value more quickly for 3 Hz frequency than other frequencies.

As may be expected, both initial and long time mixing rate constants depend on frequency of oscillations. This dependence is shown in Figure 7.16. Small values of λ for f = 1.5, 2 Hz are noticeable. For mixing, the frequency of oscillations needs to be away from the critical frequency. The available range of frequency for mixing below the critical frequency is limited, and mixing can be time consuming. Mixing at a frequency above the critical frequency is more time efficient, and theoretically, the frequency range is unlimited.

Two additional sets of results on the locus of the center of mass and the unit fluctuating energy of the binary particulate bed in the oscillating container, shown in Figures 7.13 and 7.14, respectively, are in order. As for the case of unary particulate bed, the results in Figures 7.13 and 7.14 are in agreement with the foregoing description of the binary granular flow inside the oscillating container. For the case of critical frequency oscillations, the stabilized locus of the center of mass is a circular arc, Figure 7.13(b). For f = 1 Hz, as shown in Figure 7.13(a), the stabilized locus (indicated by the overlapping loci of the 19th and 20th cycles) is slightly above the locus of the first two cycles due to the upward dispersion of large particles into the small particles bed; see Figure 7.9(a).

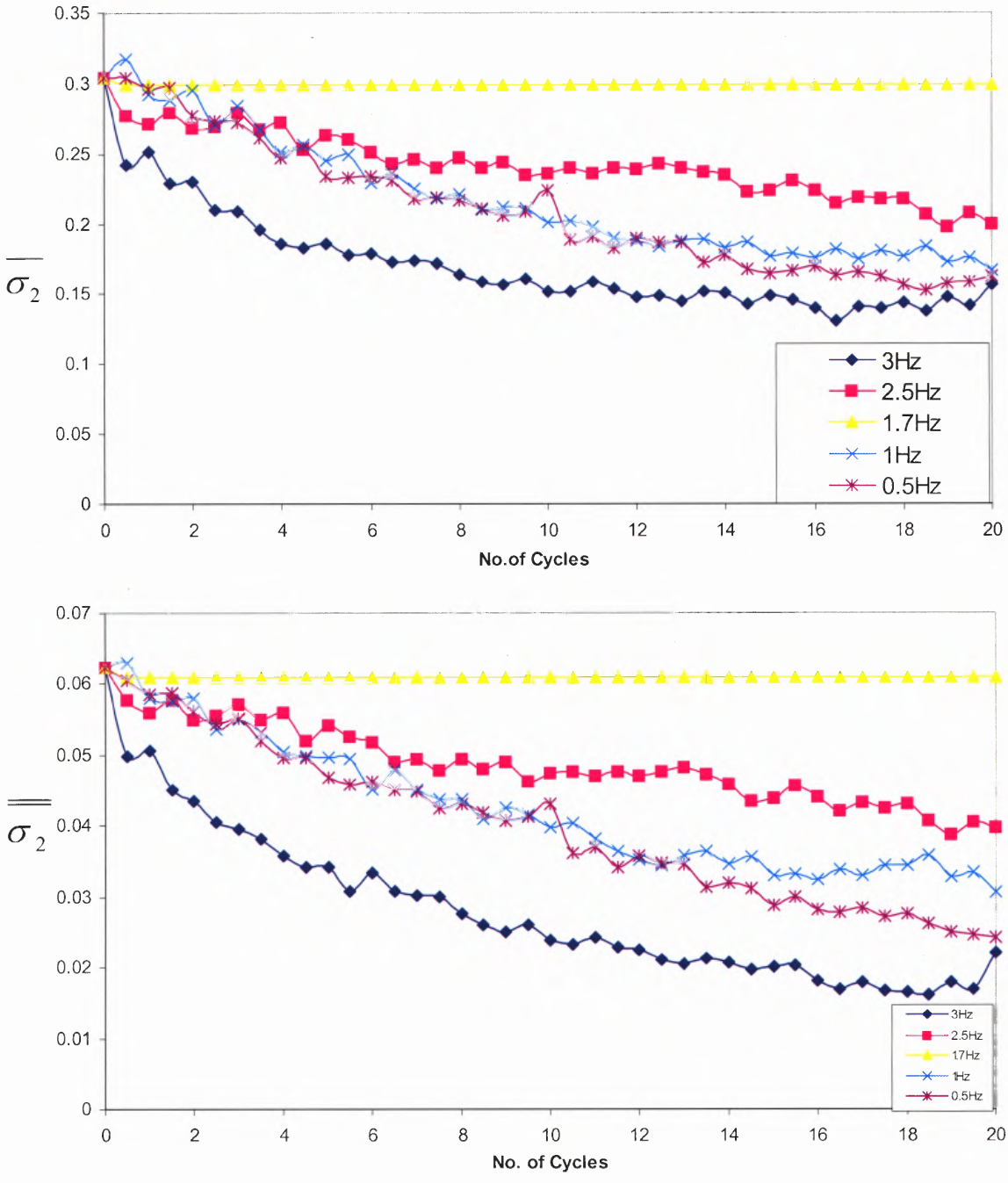

Figure 7.12 Variation of concentration and standard deviation of large particles with simulation time for various frequencies of oscillation.

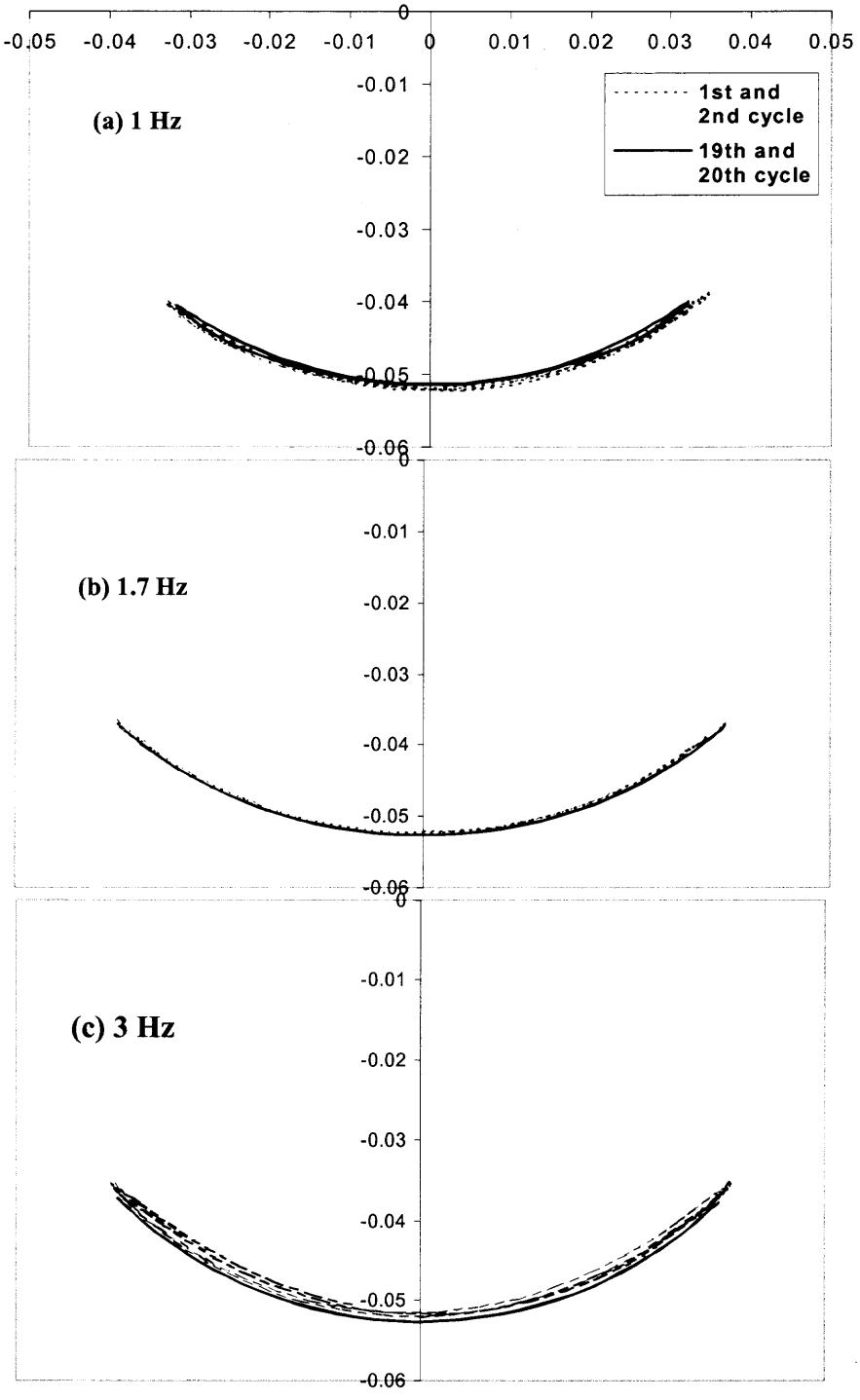

Figure 7.13 Loci of the mass center of oscillating binary particulate bed at frequencies below, equal, and above the critical frequency during first and last two oscillation cycles of 20-cycle simulations.

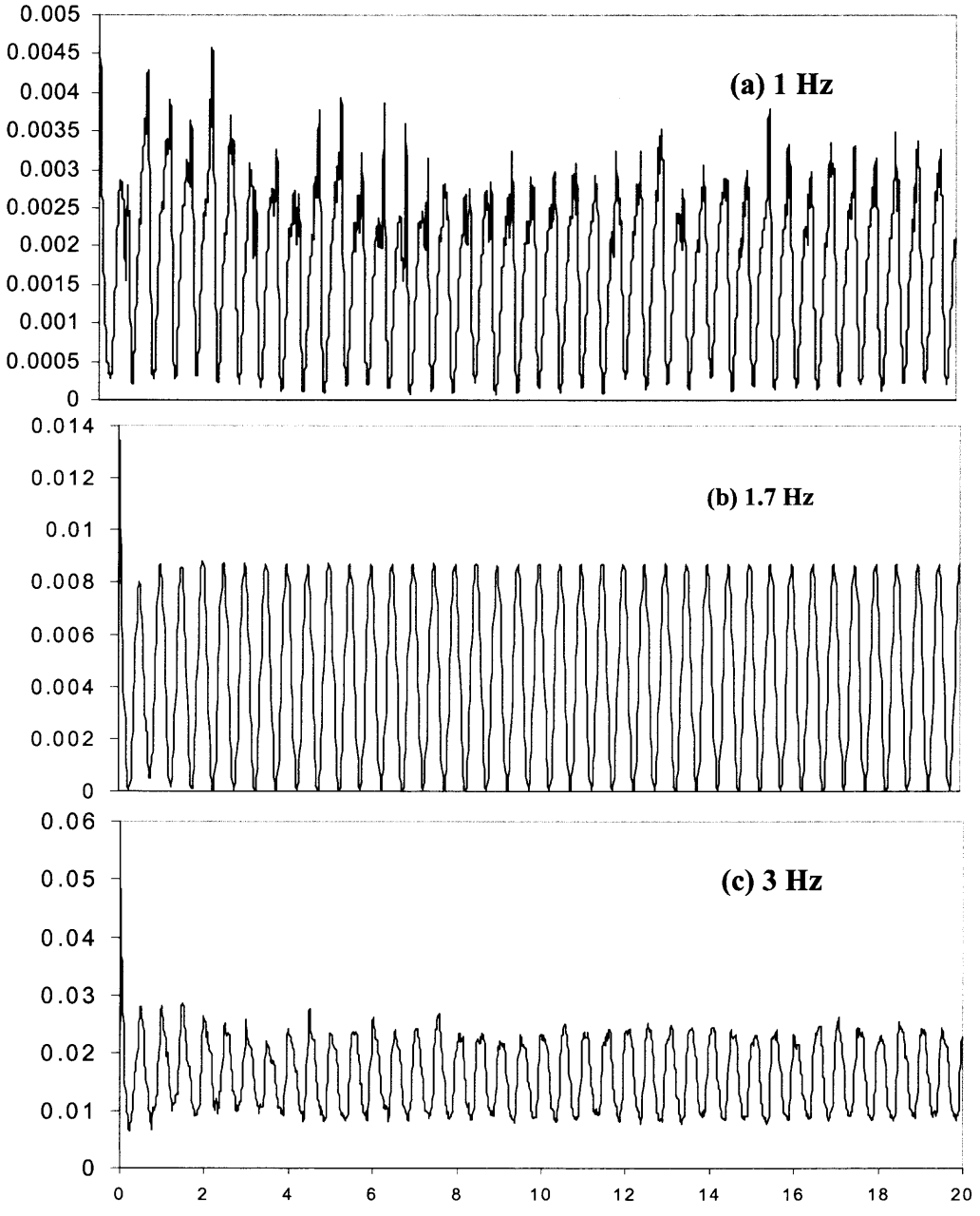

Figure 7.14 Variation of unit fluctuation energy of binary particulate bed with simulation time at frequencies below, equal, and above the critical.

Likewise, for f = 3 Hz, as shown in Figure 7.13(c), the stabilized locus (of 19th and 20th cycles) is below the locus of the first two cycles due to mixing of the particles.

7.3.3 Critical Frequency of Oscillations

The results presented in the foregoing sections for both unary and binary beds are each for only one type of setting with respect to the model parameters, number of particles, the size of sectorial container, and initial conditions. It is therefore natural to look for the effect of various system parameters on flow and mixing characteristics of granular beds in oscillating sectorial containers. Here some observations on the effect of some of the system parameters on the critical frequency are presented.

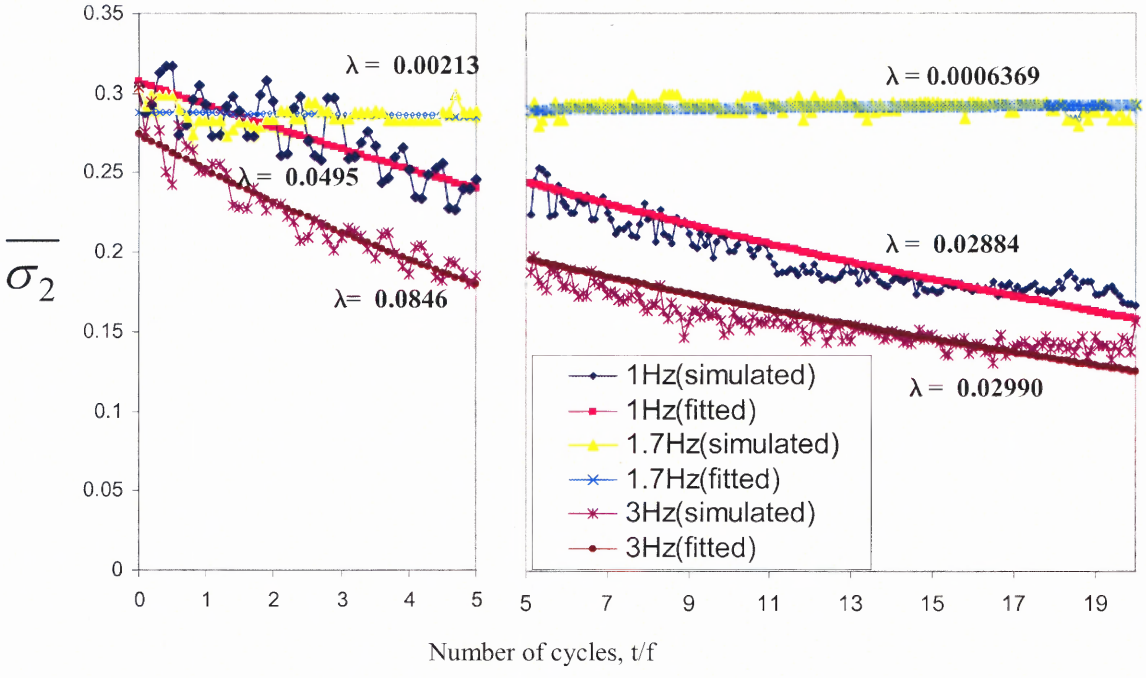

Figure 7.15 Least-square initial and long time fitting of Equation (7.15) on simulated particle concentration versus oscillation cycles data.

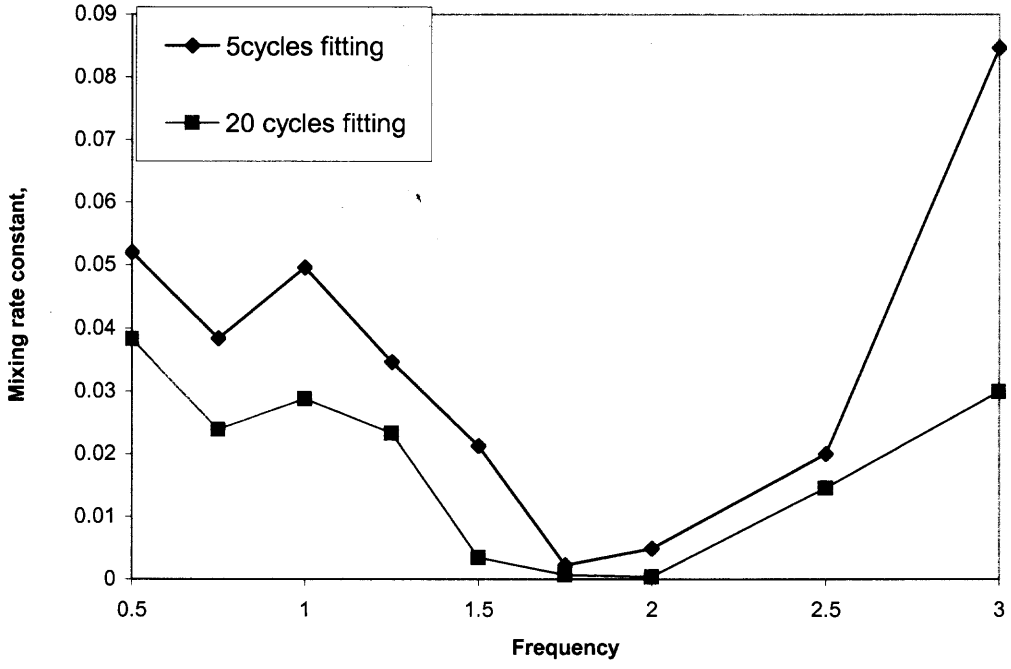

Figure 7.16 Variation of initial and long time mixing rate constants with oscillation frequency.

First, as mentioned earlier, in a container oscillating at critical frequency, the particulate bed after a few initial oscillations acquires a symmetric heap and then becomes stagnant. In that situation, the particles cease to move and, consequently, there is no interaction between the particles. It can therefore be expected that the critical frequency would be independent of the parameters of the interaction model. This was verified by determining the critical frequency for a range of values of two parameters of the interaction model, viz., the coefficients of friction and restitution. Leaving aside the interaction model parameters, the shape of symmetrically heaped bed in a container oscillating at critical frequency depends apparently on the other system parameter, such as, the size and number of particles and parameters. The effects of these parameters on the critical frequency can be guessed by simple reasoning. As an example, for a given size of container and the size of particle(s), the centroid of the particulate bed moves closer to

center of oscillations (i.e., the radius of curvature of sectorial container) with increase in the depth of the bed. Recalling that critical frequency represents balance of gravitational and centripetal actions, it is apparent that the critical frequency of oscillation should increase with increase in the number of particles.

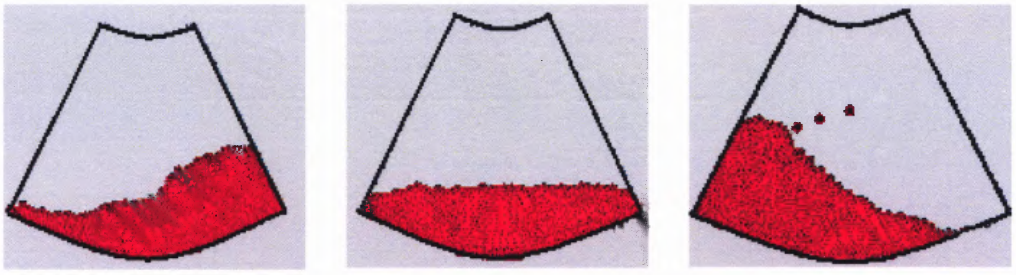

(a) 1.5Hz (b) 2.35Hz (c) 4Hz

Total number of particles: 924

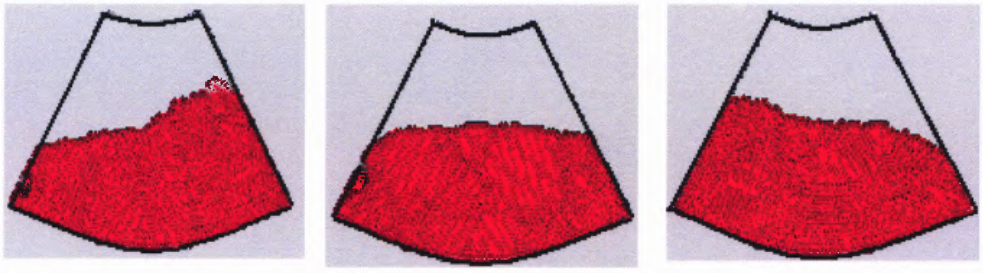

(a) 1.5Hz (b) 2.65Hz (c) 4Hz

Total number of particles: 1868

Figure 7.17 Snapshots at the end of 20 oscillation cycles of two types of unary particulate beds having different number of particles; the snapshot (b) is at critical frequency, and the snapshots (a) and (c) are at frequencies below and above the critical frequency.

Simulations were carried out to determine the critical frequencies for different number of particles for the same size of container and of particles as in Table 7.1 for unary and binary beds. Table 7.2 gives the critical frequencies for three sets of number of particles for both unary and binary beds. Note that the frequency for the number of particles used in Tables 7.1 is included in Table 7.2. The snapshots for the new sets of number of particle used in Table are shown in Figures 7.17 and 7.18 for unary and binary beds, respectively. Needless to say, the results in Table verify that the critical frequency increases with the increase in the number of particles.

Table 7.2 Effect on Number of Particles on Critical Frequency of Containers

(a) Unary Bed		(b) Binary Bed	
Number of Particles	Critical Frequency (Hz)	Number of Particles	Critical Frequency (Hz)
924	2.35	957	1.6
1399	2.60	1518	1.7
1868	2.65	1983	1.75

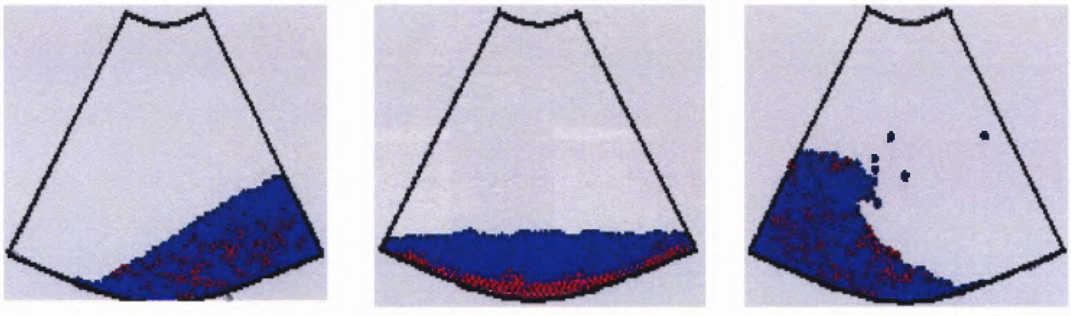

(a) 1Hz (b) 1.6Hz (c) 3Hz

Total number of particles: 957
Big particles: 101
Small particles: 856

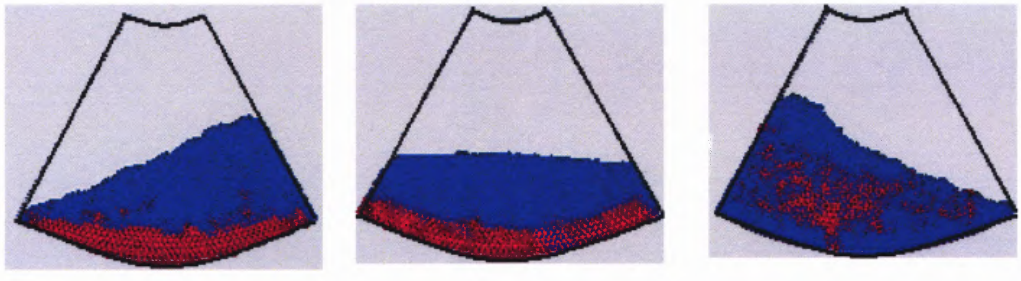

(a) 1Hz (b) 1.75Hz (c) 3Hz

Total number of particles: 1983
Big particles: 245
Small particles: 1738

Figure 7.18 Snapshots at the end of 20 oscillation cycles of two types of particulate beds having different number of particles; the snapshot (b) is at critical frequency, and the snapshots (a) and (c) are at frequencies below and above the critical frequency.

7.4 Conclusions

In this study, two-dimensional discrete element simulations were carried out to investigate the flow characteristics of unary and binary particulate beds in oscillating sectorial containers.

The simulated unary granular bed consisted of uniform size spherical particles. The binary granular bed also consisted of uniform, but of two different diameters, spherical particles. For the simulation of binary particulate bed, particulate sets of two different sizes were laid initially as separate layers. In the results presented in this chapter, it has been attempted to investigate the granular patterns via-a-vis the oscillation frequencies of the container. However, the other simulation parameters (container geometry, number and size of particles, contact model parameters, etc.) were fixed for the two types of granular beds.

The main conclusions of the present work are as follows,

1. The prominent feature of flow patterns of both unary and binary systems was heaping of the granular beds.
2. It is found that there is a critical frequency of oscillation for which the granular bed forms a symmetrical heap in which the granular bed becomes almost stagnant with little movement of the particles. The symmetric shape of granular heap is maintained throughout in a complete one cycle of oscillation.
3. Heaping becomes asymmetric with the granular bed leaning toward one of the two radial walls at oscillation frequencies on either side of the critical frequency. The granular bed heaps alternately to the two radial walls of container every half cycle of an oscillation. Further, heaping patterns are found to be opposite to each other at frequencies of oscillation below and above the critical frequency.
4. In a container oscillating at critical frequency, the two particulate layers remain separate in the symmetrically heaped bed.

5. At frequencies below the critical frequency, there is a noticeable but small amount of transfer of particles from one layer to another in asymmetrically heaped binary particulate bed. However, when the container is oscillated at frequencies greater than the critical frequency, motion of particles from one layer to another becomes intense, which eventually results into a homogeneous mixture of the two different size particulates.

CHAPTER 8

CONCLUSION AND RECOMMENDATIONS

8.1 Closing Remarks

A numerical and experimental study of dry particle coating is carried out in this research work. The main objective of this numerical study was to understand the nature of particulate flow inside the dry particle-coating device, called the hybridization system. Numerical simulations were carried out to understand the nature and type of particulate collisions and the forces, as well as the factors affecting the effective operation of the hybridization system.

Dry particle coating device, the hybridization system was simulated using different theories and techniques. In order to simulate the mixing chamber of the device, Discrete Element Method (DEM) was employed to study the system at the device level and the host particle level. The diagnostic analysis was performed. Various kinematic quantities such as rotational energies, pressure distribution were calculated and the effect of different operating conditions such as loading of the particles, and rotational speeds was studied. The results illustrated the generic behavior of the system for heavier and lighter particles. The system of heavier particles was seen to quickly settle down and the motion of particles was not seen after about 0.5 seconds of simulation. The system of lighter particles was seen to be stabilized after 0.2 seconds. However, from the particle collision analysis, the inter-particle interactions were seen to reduce gradually with the simulation time. Inter-particle collisions were seen to be higher than the particle-boundary collisions by at least an order of magnitude. The increase in the number of

collisions was seen to be linear. About 18% increase in the number of collisions was computed when the loading of particles was doubled. The tangential and normal forces were calculated. Normal forces were seen to be independent of the operating factors such as rotational speeds and the loading of particles. Tangential forces were seen to be increasing with the loading of particles as well as with the rotational speed. The normal forces were seen to be in the range of 10^{-3} N and the tangential forces in the range of 10^{-4} N.

The settling of particles inside the mixing chamber indicated that the effect of airflow induced due to the high-speed rotational blades within the system must be considered in the simulation study. Consequently, the mixing chamber as well as the re-circulating pipe were analyzed using computational fluid dynamics techniques. The velocity contours inside the mixing chamber of the hybridization system showed that the velocities were higher near outer wall (near the blades) due to the centrifugal action. Also, the velocities of air were seen to be in the range of 30-50 m/s at rotor speeds of 5000 rpm. The vortices were seen to be forming at the exit of the re-circulating pipe. The velocities of airflow inside the re-circulating pipe were seen to be nearly uniform and approximately equal to 15-20 m/s at 5000 rpm. The velocities of airflow were higher as the rotational speed was increased. Three different regions/zones of velocities were observed. Highest velocities were seen to be at the outer wall of the mixing chamber, lower velocities were at the center of the chamber and the velocities in the middle range were at the midst of the chamber (between the gap of blades and the inner cylinder). The velocities of airflow field were compared with experimentally measured velocities using a pitot tube, and were found to be in good agreement. The velocity flow field was also

characterized using another CFD code and quantitatively, the results were seen to be comparable with the velocities obtained using Fluent, a commercial fluid-modeling program. Also, the airflow was seen to be fairly uniform throughout the mixing chamber. CFD results indicated that the hybridzer device can be scaled by keeping the blade tip velocity constant in different sized systems. In other words, the rotation speeds required for the larger hybridizer device are smaller than those for a smaller hybridizer device.

Coupling of DEM and fluid velocities to understand the effect of the air velocities on the particles was carried out. The instantaneous air velocities at every node formed between the sectors were considered. The particles at a time instant close to the node were assigned the air velocity at that node in order to incorporate the effect of air drag. The inter-particle collisions and the particle-boundary collisions were calculated. The number of collisions seemed to be reduced than the earlier case of absence of air drag. The rise in the inter-particle collisions was seen to be exponential, however, the particle-boundary collisions were seen to be rising linearly with the simulation time. The normal forces were seen to be in the order of 10^{-2} N and the tangential forces in the order of 10^{-3} N. The tangential and normal forces were seen to be increased as compared to the case of no air drag. Coating quality and coating time was also estimated based upon the number of collisions obtained in this simulation. The number distribution of the particles indicated that the particles were mostly residing in the region surrounded by blades, thus clearly demonstrating the effect of air drag on the particles. DEM modeling of re-circulating pipe was also initiated. The number of collisions and the forces were estimated for a pipe flow assuming an equivalent length of pipe to take the effect of bends. The forces were seen to be very high of the order of 10^{-1} N even for a small

number of particles (100). Also, the collisions were of the order of 10^8. The results of DEM of pipe flow indicated that the particle interactions are very high which may contribute to the coating of particles inside the whole system.

Another numerical study on the granular flow mixing was done for an oscillating sectorial container. Unary as well as binary system of particles were simulated for several range of frequencies and a critical frequency was found for both the systems where the particulate bed was found to be segregated and stationary. Above and below this critical frequency, the particulate bed was seen to be heaping on the opposite sides of the container. For the unary system, this critical frequency was seen to be 2.6 Hz, whereas for the binary system of particles with the particle ratio of 1:2, this frequency was seen to be 1.7 Hz. For the lower loading of particles, the critical frequency was seen to be decreasing and for the higher loading of particles, the critical frequency was seen to be rising. The mixing degree was also calculated for the case of binary system of particles. The mixing rate constant was evaluated and was seen to be equal to 0.09 for the 3Hz case. This mixing rate constant when compared in the literature for the case of rotating cylinders was found to be on a lower side. Effect of different operating frequencies and loading conditions clearly demonstrated the ideal way of running the oscillating sectorial container from the mixing of particles point of view.

The last part of the dissertation was to study the application of dry particle coating. Three different coating devices were used to coat ground magnesium powder by using carnuba wax and hydrophobic fumed silica. The SEM images indicated the coating of wax on the surface of magnesium particle. The water immersion test indicated the uncoated sample settling down inside the water, on the other hand, the coated sample was

seen to be floating on the surface of water. The XRD tests revealed the reduction in the hydroxide formation with the coated products. The humidity tests showed that the weight increase in the coated samples after being exposed to the moisture and humidity filled chamber, was about 3 % and less than the uncoated ground magnesium, which was about 6 %. It was concluded that the dry coating of wax would extend the shelf life of ground magnesium powder.

8.2 Recommendations

The numerical and experimental studies of dry particle coating devices and its application were carried out in this research work. The field of dry particle coating is still relatively new and tremendous amount of applications and improvements in the field of dry particle coating are feasible.

In the hybridization system, a strong two-way coupling can be done in order to understand the effect of the airflow field on the particles and vice versa. The DEM and Fluid airflow model can be solved simultaneously to get even more accurate computations/behavior of the hybridization system. A high-speed digital camera can be used to capture the motion of particles inside the mixing chamber, which would assist in the verification of the simulations carried out. Moreover, the numerical study can be extended to include the modeling of host and guest particles together. Due to the computational limitations and the complex nature of the problem/geometry, this may require development of novel approaches along with the use of parallel computing.

In the area of granular flows mixing in sectorial containers, the study can be extended to the simulation of the rotation of the half semi-circular container or other

particular shapes to see the effect on segregation and mixing of particles. These results can be then compared with the mixing in rotating cylinders.

APPENDIX A

VELCOITY CONOURS FOR SINGLE PHASE MODEL

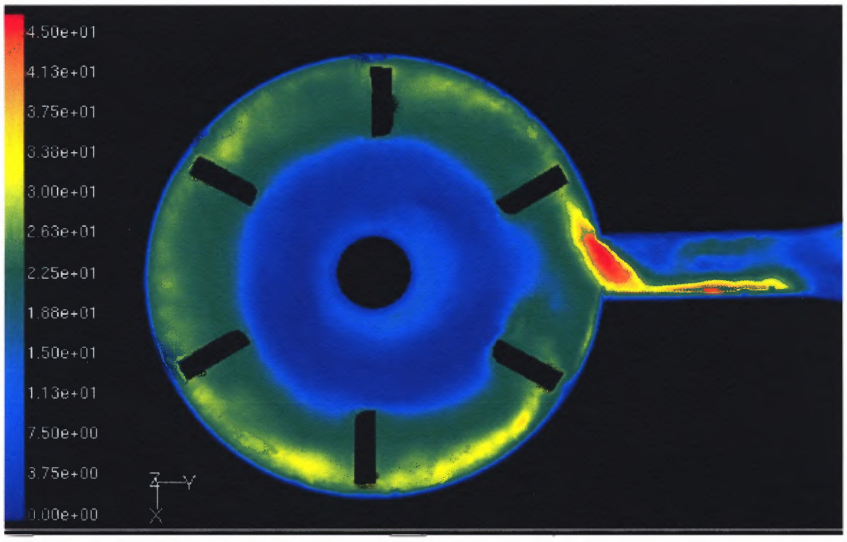

Figure A1 Flow field inside the mixing chamber at 5000 rpm using Fluent.

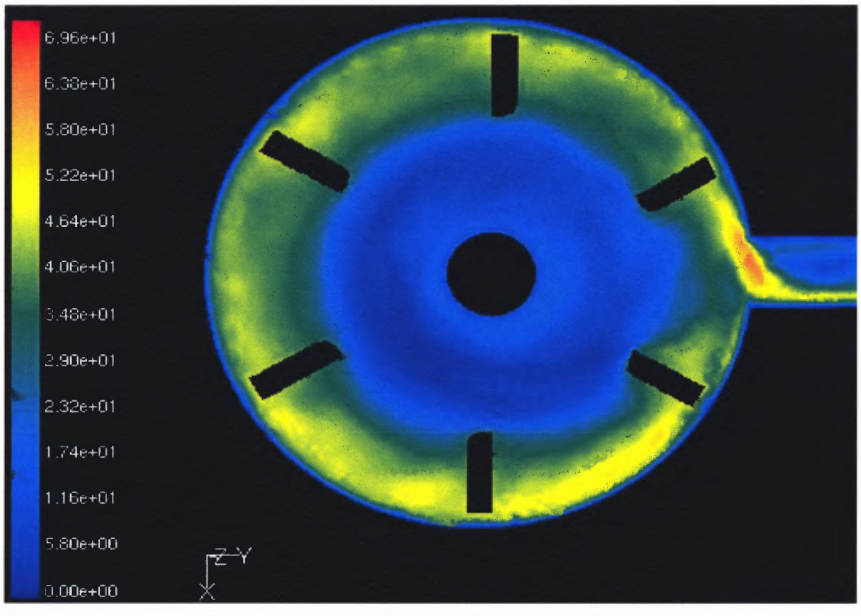

Figure A2 Flow field inside the mixing chamber at 8000 rpm using Fluent.

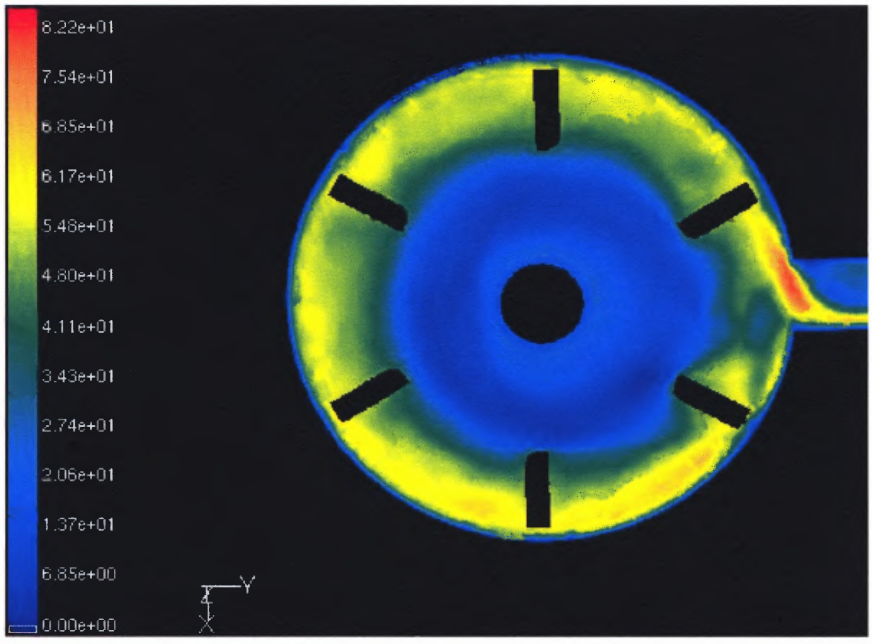

Figure A3 Flow field inside the mixing chamber at 10000 rpm using Fluent.

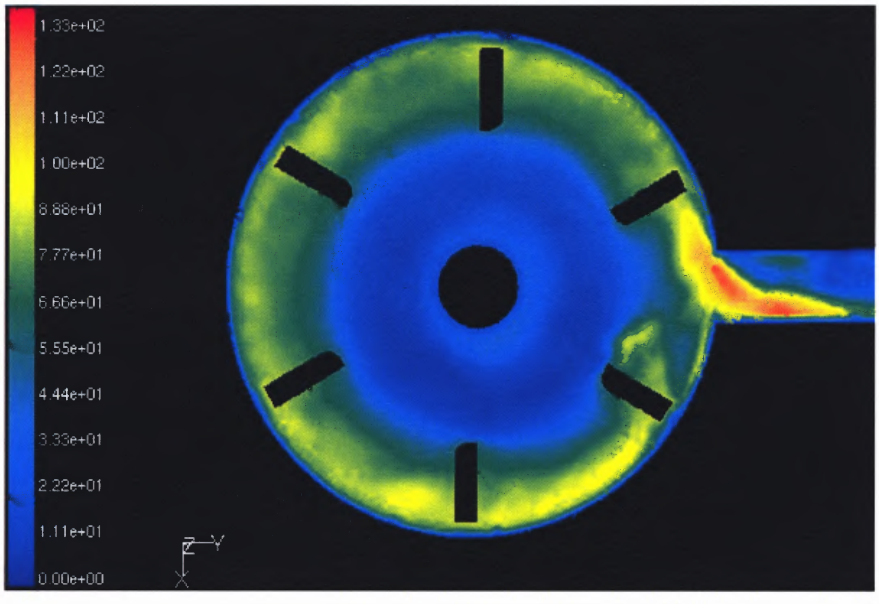

Figure A4 Flow field inside the mixing chamber at 15000 rpm using Fluent.

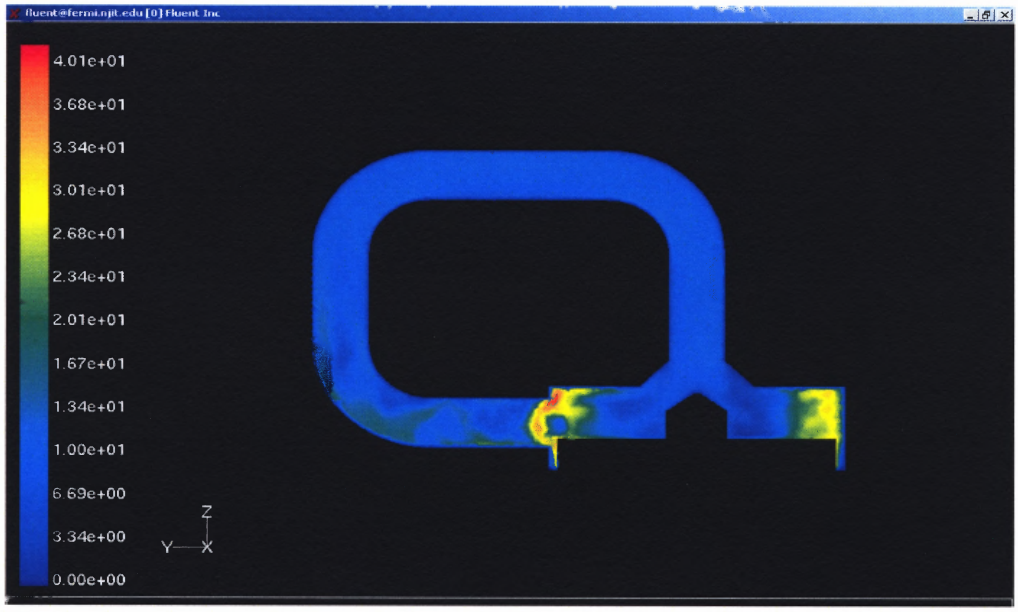

Figure A5 Flow field inside the re-circulating tube at 15000 rpm using Fluent.

APPENDIX B

VELOCITY CONTOURS OF MULTI-PHASE MODEL

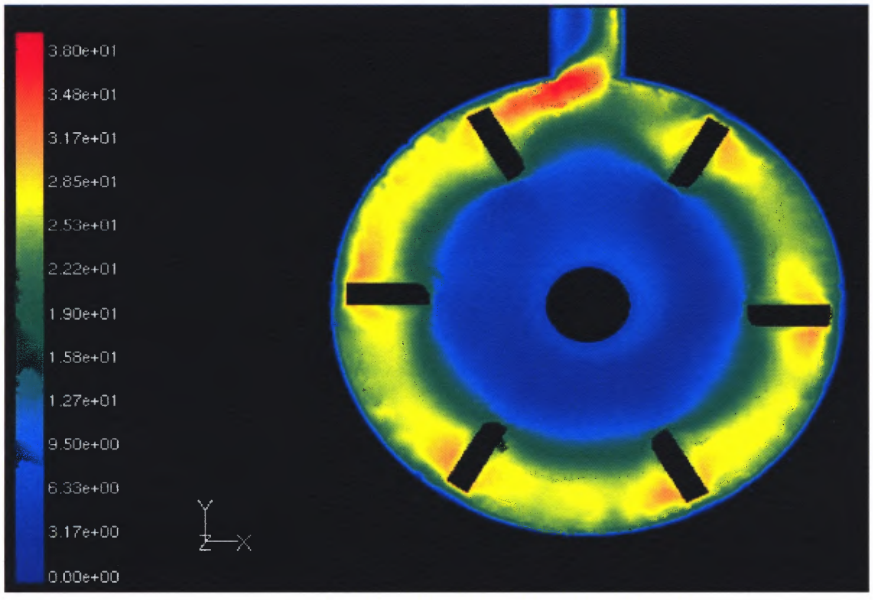

Figure B1 Velocity contours of airflow field at 5000 rpm.

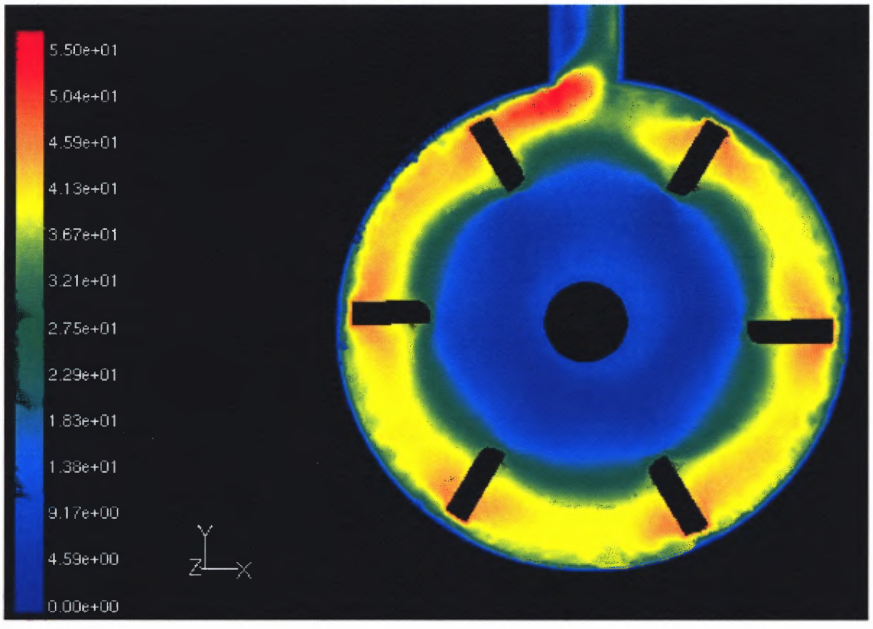

Figure B2 Velocity contours of airflow field at 8000 rpm.

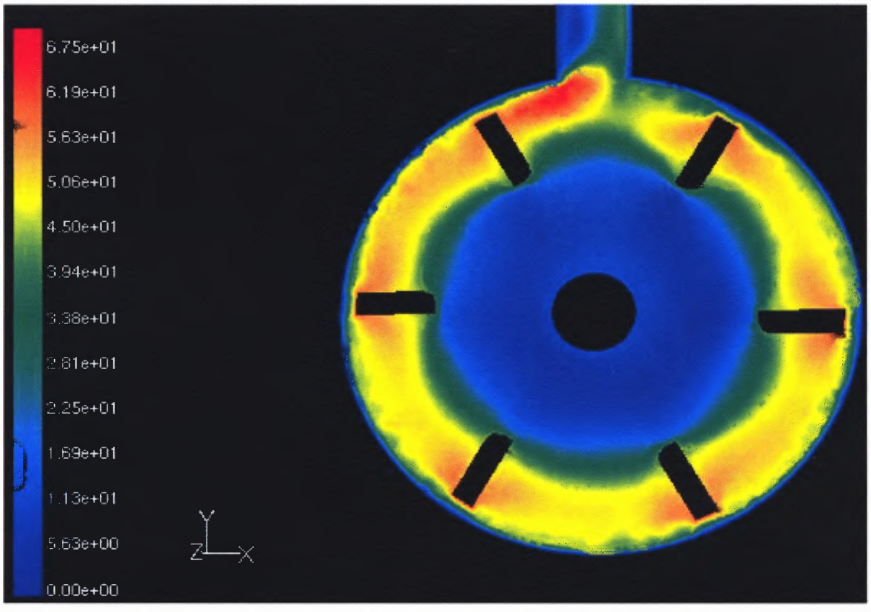

Figure B3 Velocity contours of airflow field at 10000 rpm.

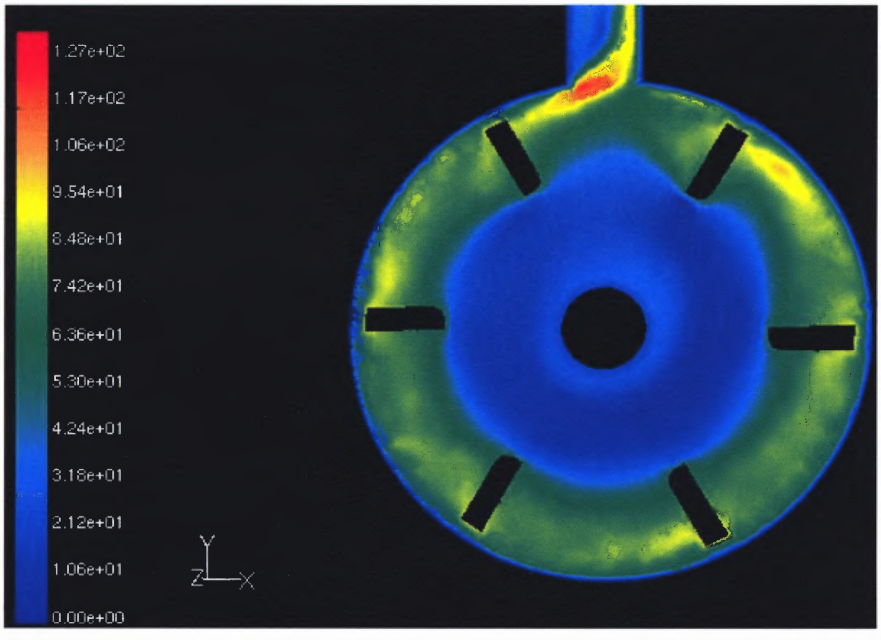

Figure B4 Velocity contours of airflow field at 15000 rpm.

APPENDIX C

SPRING STIFFNESS AND DASHPOT CONSTANT

In this appendix, the calculation of spring stiffness and dashpot constant is shown.

1. Spring stiffness k_n and k_s:

$$k_n = m^*_{ij}\left(\frac{v_n,\max}{\delta_n,\max}\right)^2\left(\exp\frac{\tan^{-1}(\alpha_{ij})-\alpha_{ij}}{\alpha_{ij}}\right)^2$$

where $v_n,\max$ is some assumed maximum relative velocity of normal impact, and $\delta_n,\max$ is the maximum allowable overlap between the particles.

Also,

$$m^*_{ij} = \frac{m_i m_j}{m_i + m_j}; \qquad \alpha_{ij} = \frac{\pi}{\ln \varepsilon_{ij}}$$

where ε_{ij} is the coefficient of restitution between the particles.

For the tangential stiffness, Cundall and Strack [1] recommend that

$$\frac{2}{3} \le \frac{k_s}{k_n} \le 1$$

2. Dashpot constant η_n:

$$\eta_n = 2\sqrt{\frac{k_n m^*_{ij}}{1+\alpha^2_{ij}}}$$

REFERENCES

Alonso, M., 1991. A Fundamental Study on the Coating of Powders, *Doctoral Thesis*,

Alonso, M., Satoh, M., and Miyanami, K., 1989a. *Powder Technology*, Vol. 59, 45.

— 1989. *Journal of the Society of Powder Technology*, Japan, Vol. 26 (9), 666.

— 1989b. *Powder Technology*, Vol. 59, 65.

— 1989c. *KONA*, Vol. 7, 97.

— 1989c. *Powder Technology*, Vol. 59, 217.

— 1990. *Powder Technology*, Vol. 62, 35.

A: Physicochemical and Engineering Aspects, 82, 117-128.

Anderson, T. B., and Jackson, R., A fluid mechanical description of fluidized beds, 1967, *I&EC Fundam.*, 6, 527-539.

Bannister, P., and Harnby, N., *Powder Technology*, Vol. 36 (1983) 275.

Blazer, G., Simonin, Q., Boelle, A., and Lavievelle, J., 1996, A unifying modeling approach for the numerical prediction of dilute and dense gas-solid two-phase flow, *Proceedings of 5th International conference on Circulating fluidized Beds*, May, Bejing, China.

Bryan, L., Rungvejhavuttivitaya, Y., and Stewart, P.J., 1979. *Powder Technology*, Vol. 22, 147.

Campbell, C. S. and C. E. Brennen, Computer simulation of granular shear flows, *J. Fluid Mech.* **151**, 167-188 (1985).

Chaudhuri, B., Singh, P., Pfeffer, R., and Dave, R. N., *World Congress on Particle Technology*, Brighton, U.K., July 7-9, 1998.

Chen, Y.S., A Computer Code for Three-Dimensional Incompressible Flow Using Non-orthogonal Body-Fitted Coordinate Systems, NASA-CR-178818.

Cundall, P.A. and Strack, O. D. L., Discrete numerical model for granular assemblies, *Geotechnique* **29**, 47-65 (1979).

Ding, J., and Gidspaw, D., 1990, A bubbling fluidization model using kinetic theory of granular flow, *A.I.Ch.E. J.*, 36, 523-538.

Dreizin, E., Shoshin Y., and Mudryy R., "High Energy Density Powders Of The Al-Mg Mechanical Alloys", 50th JANNAF Joint Propulsion Meeting, Salt Lake City, UT, July 11-13, 2001.

Enstad, G. G., *Inst. Chem, Engrs. Symp. Series*, Vol. 65, S2/H (1981).

Fitz-Gerald J., Pennycook, S., Gao. H., and Singh, R. K., 1999a. *Nanostructured Materials*, Vol.12, 1167-1171.

Fitz-Gerald, J., Singh R. K., and Gao, H., 1999b. *Journal of Material Research*, Vol. 14, No. 8, 3281-3291.

Fitz-Gerald, J., Singh, R. K., Trottier, T., and Holloway, P. H., 1998. *Applied Physics Letter*, Vol. 72, 15.

Hendrickson, W., and Abbott, J., 1997. "Process for Making Particle-Coated Solid Substrates", *U. S. Patent Laid-Open.*

Hersey, J., *Powder Technology*, Vol. 11 (1975) 41.

Hersey, J., Thiel W. J., and Yeung C. C., 1979. *Powder Technology*, Vol. 24, 251.

Honda, F., Honda H., and Koishi, M., 1992. *Journal of Chromatography*, 609, 49-59.

Honda, H., Kimura, M., Honda, F., Matsuno, T., Koishi, M., 1994. *Colloids and Surfaces A: Physicochemical and Engineering Aspects*, 82, 117-128.

Honda, H., Kimura, M., Matsuno, T., and Koishi, M., 1991. *CHIMICA OGGI: International Journal Chemistry and Biotechnology,* Vol. 9, 21.

Honda, H., Matsuno, T., and Koishi, K., 1988. *Journal of the Society of Powder Technology*, Japan, Vol. 25 (9), 597.

— 1989. *Journal of the Society of Powder Technology*, Japan, Vol. 26 (9), 666.

Honda, H., Ono, K., Ishizaka, T., Matsuno, T., Katano, K., and Koishi, M., 1987. *Journal of the Society of Powder Technology*, Japan, Vol. 24 (9), 593.

Horio, M., Mikami, T., and Kamiya, H., 1998, Numerical simulation of cohesive powder in a fluidized bed, *Chemical Engineering Science*, Vol. 53(10), 1927-1940. *International Journal Chemistry and Biotechnology,* Vol. 9, 21.

Ishizaka, T., Honda, H., Kikuchi,Y., Katano, T., and Koishi, M., 1988. *Chemical Pharmaceutical Bulletin*, Vol. 36, 2562-2569.

James, G.A., Experimental and Numerical Study of Flow Characteristics and Segregation in Flow Enhancements Systems, Ph.D. Thesis, New Jersey Institute of Technology, Newark, NJ, 2002.

James, G.A., Malik, M., and Dave, R.N., Experimentally-observed and numerically-simulated characteristics of granular flows in vibrated wedge-shaped containers, presented at: *AIChE Annual Meeting, Fourth International Particle Technology Forum*, Los Angeles, CA, November 12-17, 2000; see CD-ROM proceedings.

Kafui, K. D. and C. Thornton, Computer simulated impact of agglomerates, in *Powder & Grains'93*, Thornton (ed.), 401-406, Balkema, Rotterdam (1993).

Kalyon, D., and Yazici, R., "Hydroxide Formation in Atomized and Ground Magnesium Powders", A report made for ARDEC (Picatinny Arsenal), 1996.

Kaneyasu, A., Yamamoto, S., and Watanabe, T., (Ube Chemical Industry Co. Ltd., Yamaguchi (Japan)), Taikabutsu (Refractories), **47(9)** (1995) 444-449.

Khakhar, D. V., McCarthy, J. J., Shinbrot, T., Ottino, J. M., Transverse flow and mixing of granular materials in a rotating cylinder, *Phys. Fluids*, 9 (1997) 31-43.

Ladd, A., Molecular dynamics, *Lectures to be given at the Nato Advanced Summer Institute in Bath*, England, September 4--17, (1988).

Lai F. S., and Hersey, J. A., 1981. *Chem. Eng. Sci.*, Vol. 36, 1133.

Lai, F. S., Hersey, J. A., and Staniforth, J. N., 1981. *Powder Technology*, Vol. 28.

Launder, B.E., and Spalding, D.B., 1972, Mathematical models of turbulence, Academic press.

Lian, G., C. Thornton and M. J. Adams, A microscopic simulation of oblique collisions of 'wet' agglomerates, in *Powder & Grains'97*, Behringe & Jenkins (eds.), 159-162, Balkema, Rotterdam (1997).

Lian, G., C. Thornton and M. J. Adams, Discrete particle simulation of agglomerate impact coalescence, *Chemical Engineering Science* **53**, 19, 3381-3391 (1998).

Maliska, C.R., and Raithby, G.D., 1984, A method of Computing Three Dimensional Flows Using Non-Orthogonal Boundary Fitted Coordinates, *International Journal for Numerical Methods in Fluids*, Vol. 4, 519-537.

Masaru, O., Hironori, M., Tetsuya, U., and Kunio, S., *Advanced Powder Technol.* **7(4)** (1996) 291.

Mitsui mining and smelting organization, Jap. Pat. Abs., Gp G 21, **90(9)** (1990) Patent No. JP 02/014258.

Miyanami K., Satoh M., and Yoshida T., *Proceedings of first International Particle Technology Forum*, AIChE, Part III, **17**, Denver, USA, August (1994).

Mujumdar, A., Malik, M., Pfeffer, R., and Dave, R.N., Numerically-simulated characteristics of granular flows in oscillating and rotating, sectorial and cylindrical passages, presented at: *AIChE Annual Meeting, Fourth International Particle Technology Forum*, Los Angeles, CA, November 12-17, 2000; see CD-ROM proceedings.

Naito M., Yoshikava M., Tanaka T., and Kondo A., Kona, **11** (1983) 229.

Naito, M., Kondo, A., and Yokoyama, T., *ISIJ International*, 33, 915, 1993.

Ning, Z., R. Boerefijn, M. Ghadiri and C. Thornton, Effects of particle size and bond strength on impact breakage of weak agglomerates, in *Powder & Grains'97*, Behringe & Jenkins (eds.), 127-130, Balkema, Rotterdam (1997).

Patankar, S.V., 1980, Numerical Heat Transfer and Fluid Flow, McGraw-Hill Book Company.

Pfeffer, R., Dave, R. N., Wei, D., and Ramlakhan, M., *Powder Technol.* **117** (2001) 40.

Pritchett, J. W., Blake, T. R., and Garg, S. K., 1978, A numerical model of gas fluidized bed, *AIChE Symp. Ser.* No. 176, 74, 134-148.

Ramlakhan, M., Wu, C. Y., Watano, S., Dave, R. N., and Pfeffer, R., *World Congress on Particle Technology*, Brighton, UK, July 7-9, 1998.

Ramlakhan, M., Wu, C.Y., Watano, S., Dave, R.N., and Pfeffer, R., Powder Technology, Vol. 112 (1-2) (2000) 137-148.

Ramlakhan, M., Wu, C.Y., Watano, S., Dave, R.N., and Pfeffer, R., 2000, *Powder Tecnology*, Vol. 112 (1-2), 137-148.

Rietema, K., 1973, The effect of interparticle forces on the expansion of a homogeneoud gas-fluidized bed, *Chem. Engng. Sci.*, 28, 1493-1497.

Schmitz, Arno, Dr.Lerchenain, Germany, (1992) Patent No. 00288964/EP B1.

Shoshin Y., Mudryy R., and Dreizin E., "Preparation and Characterization of Energetic Al-Mg Mechanical Alloy Powders" The Second Joint Meeting of the US Sections of the Combustion Institute, Oakland, California, March 25-28, 2001.

Singh, R. K., Ata, A., and Fitz-Gerald, J., 1997. *Surface Modification Technologies.*

Singh, R. K., Ata, A., Fitzgerald J., and Rabinovich, Ya. I., *KONA*, **15** (1997) 121-131.

Staniforth J. N., and Rees, J. E., 1981. *Powder Technology*, Vol. 30, 255.

Syamlal, M., and O'Brien, T.J., 1996, MFIX documentation, theory guide, Technical note, DOE/METC –94/1004.

Takafumi, I., Yuji, K., and Kenji, O., Sixth International Symposium on Agglomeration, Nov 15-17 (1993), Nagoya, Japan.

Tanno, K., Current status of the Mechanofusion process for producing composite particles, *KONA* 8, 74 (1990).

Thiel, W. J., and Stephenson, P. L., *Powder Technology*, Vol. 31 (1982) 45.

Thornton, C. and K. K. Yin, Impact of elastic spheres with and without adhesion, *Powder Technology* **65**, 153-166 (1991).

Thornton, C. and Z. Ning, A theoretical model for the stick/bounce behavior of adhesive, elastic-plastic spheres, *Powder Technology* **99**, 154-162 (1998).

Thornton, C., K. K. Yin and M. J. Adams, Numerical simulation of the impact fracture and fragmentation of agglomerates, *J. Phys. D: Appl. Phys.* **29**, 424-435 (1996).

Tsuiji, Y., Activities in discrete particle simulation in Japan, *Powder Technol.* 113 (2000) 278-286.

Tsuiji, Y., Kawaguchi, T., Tanaka, T., 1993, Discrete particle simulation two-dimensional fluidized bed, *Powder Technology*, Vol. 77, 79-87.

Vanka, S.P., Chen, B.C.-J., and sha, W.T., A Semi-Implicit Calculation Procedure for Flows Described in Boundary Fitted Coordinate Systems, 1980, *Numerical Heat Transfer*, Vol. 3, 1-19.

Walton, O. and Braun, R., *J. Rheology* **30,** 5, 949 (1986).

Walton, O. R., *Mechanics of Materials* **16**, 239-247 (1993).

Walton, O. R., R. L. Brann, R. G. Mallon and D. M. Cervelli, Particle-dynamics calculation of gravity flow of inelastic, frictional spheres, in *Micromechanics of Granular Materials*, M. Satake and J. T. Jenkins, eds., Elsevier Sci. Pub. (1988).

Wassgren, C.R., Vibration of Granular Materials, Ph.D. Thesis, California Institute of Technology, Pasadena, CA, 1997.

Wassgren, C.R., Brennen, C.E., and Hunt, M.L., Vertical vibration of a deep bed of granular material in a container, *J. Appl. Mech.* 63 (1996) 712-719.

Watano, S., Imada, Y., Miyanami, K., Wu, C.Y., Dave, R.N., and Pfeffer, R., *J. of Chem. Eng.*, Japan **33(6)** (2000) 848-854.

Watano, S., Pfeffer, R., Davé, R. N. and Dunphy, W., "Dry Particle Coating by a Newly developed Roatating Fluidized Bed Coater," *Advanced Technologies for Particle Processing: 1998 AIChE Conference*, Vol. I, pp. 598-565, November 1998.

Yeung C. C., and Hersey, J., 1979. *Powder Technology*, Vol. 22, 127.

Yip C. W., and Hersey J., *Powder technology*, Vol. 16 (1977) 149.

Yip C. W., and Hersey J., *Powder technology*, Vol. 16 (1977) 189.

Yokoyama, T., K. Urayama, The Angmill Mechanofusion system and its applications, *KONA* **5**, 59 (1987).

Yokoyama, T., Uehara, K., and Naito, M., Kona, **5** (1987) 559.

Yuu, S., Umekage, T., and Johno, Y., 2000, Numerical simulation of air and particle motionsin bubbling fluidized bed of smaller particles, *Powder Technology*, Vol. 110, 158-168.